A MULTISCALE INVESTIGATION OF GAP JUNCTIONS IN MYOCYTE-FIBROBLAST INTERACTIONS

A Dissertation

Presented to the Faculty of the Weill Cornell Graduate School

of Medical Sciences

in Partial Fulfillment of the Requirements for the Degree of

Doctor of Philosophy

by

Tashalee Rushell Brown

August 2016

A MULTISCALE INVESTIGATION OF GAP JUNCTIONS IN MYOCYTE-FIBROBLAST INTERACTIONS

Tashalee Rushell Brown, Ph.D.

Cornell University 2016

The adult heart is composed of a dense network of cardiomyocytes surrounded by non-myocyte cells, the most abundant of which are cardiac fibroblasts. Several cardiac diseases, such as myocardial infarction or pressure overload, are associated with an increased density of fibroblasts, i.e., cardiac fibrosis. Fibroblasts are known to play a significant role in the development of electric and mechanical dysfunction of the heart, however the exact mechanisms are only partially understood. One widely studied hypothesis suggests that fibroblasts produce excess extracellular matrix, resulting in collagenous septa. These collagenous septa slow propagation, cause zig-zag conduction paths, and decouple cardiomyocytes resulting in a substrate for cardiac arrhythmia. Another emerging hypothesis suggests that fibroblasts promote arrhythmogenesis through direct electrical interactions with cardiomyocytes via gap junctional channels. In the heart, three major connexin (Cx) isoforms, Cx40, Cx43 and Cx45 form gap junction channels in cell-type-specific combinations. Because each Cx is characterized by unique gating properties (i.e., time- and voltage-dependent gating), the hypothesis that the electrophysiological contributions of fibroblasts may vary with the specific composition of the myocyte-fibroblast gap junction channel was explored in this study. First, the role of gap junction channel gating in myocyte-fibroblast interactions was investigated by using a unique strategy of coupling fibroblasts electrophysiology models with *in vitro* single cell ventricular cardiomyocytes via mathematical models of gap junction channel gating using the dynamic-clamp technique. These investigations revealed that gap

junction gating reduces the peak of the junctional current compared to a constant value conductance representation of gap junctions. Second, the gap junction models were incorporated into a detailed two-dimensional computational model of cardiac fibrosis. These simulations revealed that gap junction channel gating did not significantly alter impulse propagation and conduction velocity during cardiac fibrosis. Finally, a novel experimental approach using dye transfer techniques in cardiac tissue slices was developed and used to investigate myocyte-fibroblast interactions in a multicellular environment. These studies presents a framework for a multiscale approach to investigate complex myocyte-fibroblast interactions that have the potential to lead to a clearer understanding of the emerging mechanism by which cardiac fibroblasts promote cardiac arrhythmogenesis.

BIOGRAPHICAL SKETCH

Tashalee Rushell Brown was awarded a bachelor's of science in Biomedical Engineering from Johns Hopkins University in Baltimore, M.D. in May 2009. After spending two years conducting research at the National Institute of Aging as a Postbaccalaureate Intramural Research Trainee and at Weill Cornell Medical College as a Research Technician, she enrolled in the Weill Cornell/Rockefeller/Sloan-Kettering Tri-Institutional M.D.- Ph.D. Program in New York, NY in July 2009. Upon completion of her first two years of medical school, she began her thesis work in Dr. David Christini's laboratory in September 2011.

Dedicated to my mother Joyce May Brown who passed before this journey began but has been with me every step of the way.

ACKNOWLEDGEMENTS

This work was supported by grants from the National Institutes of Health (T32GM07739 to the Weill Cornell / Rockefeller / Sloan- Kettering Tri-Institutional MD/PhD Program; R01EB016407 to DJC; F31HL124939 to TRB) and by the UNCF/Merck Graduate Science Research Dissertation Fellowship to TRB.

TABLE OF CONTENTS

1 Introduction* **1**
1.1 Overview . . . 1
1.2 Basic cardiac electrophysiology . . . 1
1.3 Cardiac fibroblasts . . . 5
1.3.1 Myocyte-fibroblast interactions . . . 9
1.4 Biophysical properties of cardiac gap junctions . . . 10
1.4.1 Voltage-dependent gating of connexin channels . . . 13
1.4.2 Detecting junctional communication . . . 16
1.5 Computational modeling of the heart . . . 19
1.5.1 Mathematical models of gap junctions . . . 19
1.6 Mathematical models of cardiac fibroblasts . . . 21
1.7 Simulations of fibroblast-myocyte coupling . . . 23
1.8 Dynamic-clamp technique . . . 33
1.9 Project overview . . . 34

2 Illuminating myocyte-fibroblast homotypic and heterotypic gap junction dynamics using the dynamic-clamp technique† **43**
2.1 Abstract . . . 43
2.2 Introduction . . . 44
2.3 Methods . . . 46
2.4 Results . . . 51
2.5 Discussion . . . 61
2.6 Conclusions . . . 62
2.7 Limitations . . . 63

3 Investigating the influence of gap junction channel gating on impulse propagation and conduction velocity during cardiac fibrosis‡ **68**
3.1 Abstract . . . 68
3.2 Introduction . . . 69
3.3 Methods . . . 71
3.4 Results . . . 73
3.5 Discussion . . . 80
3.6 Conclusions . . . 82

4 A new approach to investigating myocyte-fibroblast interactions in cardiac tissue slices **85**
4.1 Abstract . . . 85
4.2 Introduction . . . 86
4.3 Materials and Methods . . . 88
4.4 Results . . . 94
4.5 Discussion . . . 101
4.6 Conclusions . . . 102

5 Conclusions and future directions **105**
5.1 Summary of research 105
5.2 Future directions 106
5.2.1 Cardiac tissue slice from transgenic mouse models 106
5.2.2 Internal pipette perfusion 107
5.2.3 Detailed electrophysiological modeling of cardiac tissue slices . 108
5.3 Concluding thoughts 108

A Appendix **112**
A.1 Equations for the gap junction model 112
A.2 Parameters of gap junction model 112

LIST OF TABLES

2.1 Orientation of gap junction channel models 56

4.1 Fluorescent Tracers 92

A.1 Connexin model parameters 113

LIST OF FIGURES

1.1 Electrical activity in the mammalian heart 2
1.2 Currents underlying the action potential waveform 4
1.3 Electron microscopy images of the adult guinea pig heart 6
1.4 Patterns of cardiac fibrosis 8
1.5 Gap junction channel configurations 12
1.6 Dependence of gap junctional conductance on transjunctional voltage . 14
1.7 Assays for detecting gap junction coupling 17
1.8 Dynamic-clamp technique 34
1.9 Multiscale study of gap junctions in myocyte-fibroblast interactions . . 35

2.1 Schematic of dynamic-clamp technique 48
2.2 Mathematical modeling of homotypic Cx43, Cx45, and heterotypic Cx43/Cx45 gap junction using the Vogel model 53
2.3 Dynamic-clamp recordings using *in vitro* guinea pig ventricular cardiomyocytes 55
2.4 Simulations of dynamic-clamp recordings using a cell-specific model. . 58
2.5 Plots of underlying current response during myocyte-fibroblast coupling using a cell-specific model 60

3.1 Myofibroblast insertion model architecture 74
3.2 Effects of myocyte-fibroblast Cx phenotype on conduction velocity – myofibroblast insertion model architecture 76
3.3 Two layer myofibroblast attachment model architecture of cardiac fibrosis 78
3.4 Effects of myocyte-fibroblast Cx phenotype on conduction velocity – myofibroblast attachment model architecture 80

4.1 Dual tracer technique 87
4.2 Overview of protocol steps 89
4.3 Cardiac tissue slice morphology 95
4.4 Field potential recordings from cardiac tissue slices 96
4.5 Cardiomyocyte microinjection under visual control 98
4.6 Non-myocyte microinjection under visual control 99
4.7 Investigating myocyte-to-myocyte coupling 100
4.8 Investigating non-myocyte to myocyte coupling 101

LIST OF ABBREVIATIONS

APD	Action potential duration
CV	Conduction velocity
Cx	Connexin
DC	Dynamic-clamp
DDR2	Discoid domain receptor 2
EAD	Early after depolarization
ECG	Electrocardiogram
FSP1	Fibroblast Specific Protein 1
G_j	Gap junctional conductance
I_j	Junctional current
MEA	Multi-Electrode Array
PBS	Phosphate Buffered Saline
PFA	Paraformaldehyde
RT	Room temperature
V_j	Transjunctional Voltage
V_{myo}	Myocyte membrane voltage
V_{fib}	Fibroblast membrane voltage

LIST OF SYMBOLS

α rate constant of gap junction opening

β rate constant of gap junction closure

γ_{open} main open state or a gap junction channel

γ_{res} sub-conductance or residual state of a gap junction channel

CHAPTER 1

INTRODUCTION*

1.1 Overview

The aim of this thesis is to use a hybrid computational modeling and experimental electrophysiology approach to investigate the role of gap junctional channels on interactions between cardiomyocytes and cardiac fibroblasts on the single cell and multicellular level. This introductory chapter will first present a basic introduction to cardiac electrophysiology. Next, the biology of cardiac fibroblasts relevant to cardiac arrhythmogenesis is discussed. Then, the biophysics of cardiac gap junction channels and the current techniques used to assay junctional communication are described. Next, the major findings of the existing computational studies investigating the implications of myocyte-fibroblast interactions in the heart are reviewed. Finally, the dynamic clamp technique and the approaches used in this thesis are introduced.

1.2 Basic cardiac electrophysiology

The coordinated pumping of blood through the heart results from a series of dynamic interactions that occur on the whole organ to the subcellular level. At the whole organ level, cardiac action potentials propagate through the heart via conduction pathways initiated in the sinoatrial node, which spreads through the atria, the atrioventricular node, and then through the specialized His-Purkinje conduction system into both ventricles (Figure 1.1).

*Section 1.5 has been published in full in [1]

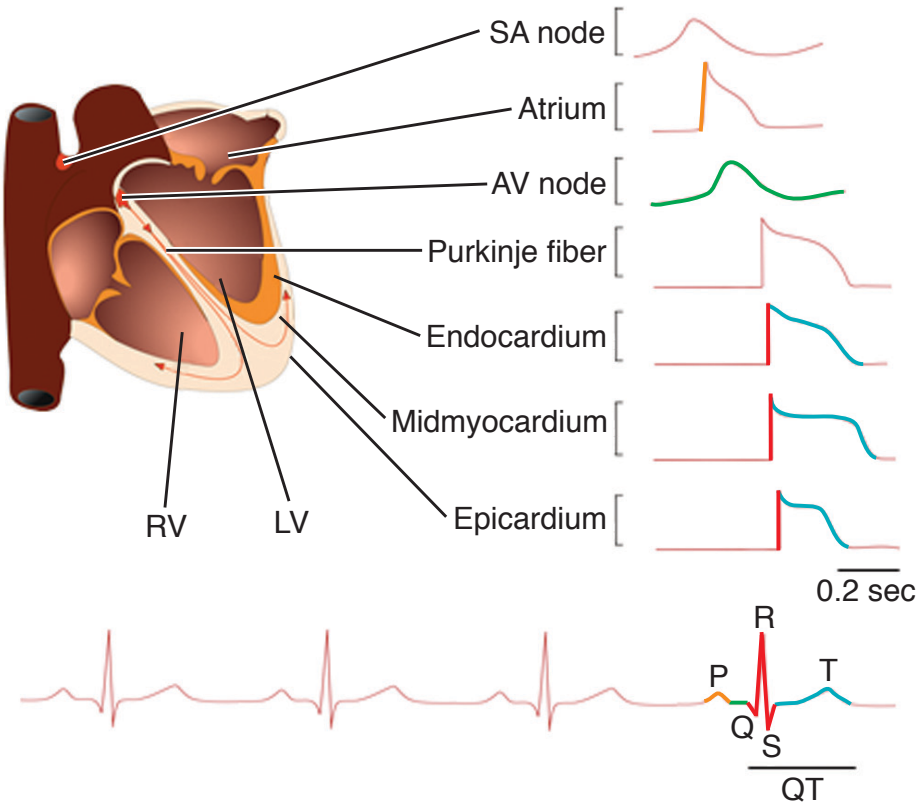

Figure 1.1 | *Electrical activity in the mammalian heart*
Schematic diagram of the mammalian heart with different anatomical regions labeled and representative action potential waveforms from those regions demonstrate that action potential morphology and duration is heterogenous throughout the heart. The action potential waveform in the sinoatrial node and atrioventricular node have a slow upstroke velocity compared to the atrium and ventricle. Epicardial cells have a prominent phase 1 notch and a shortened action potential duration compared to the midmyocardial region. The different components of the surface electrocardiogram (ECG) reflect different events in the cardiac cycle. The P wave reflects the time course for the spread of atrial depolarization (*orange*). Conduction through atrioventricular node occurs during the isoelectric portion of the PR interval (*green*). The QRS is the time for ventricular depolarization (*red*), and the QT interval represents ventricular depolarization (*blue*). RV - right ventricle, LV - left ventricle, SA node - sinoatrial node, AV node - atrioventricular node. Reproduced with permission from Elsevier [2].

At the tissue level, propagation of an acton potential results from local current flow through intercellular gap junction channels from a depolarized cell to a less depolarized neighboring cell. The rate of propagation, or conduction velocity, is determined by several factors including: the excitability of the cardiomyocytes, which is determined by the Na^+ and Ca^{2+} currents, the axial resistance to current flow, which arises from the cytoplasmic resistance of the cardiomyocyte and the gap junction channel conductance, the capacitance of the cell membrane, and the geometrical relationship or network properties of cardiomyocytes [3]. These determinants of conduction velocity can further be grouped into two categories called source and sink factors. Source factors involve excitability of cell membranes such as excitable inward currents. Sink factors include the passive electrical properties of the cells and tissue structure such as cell geometry and connectivity.

At the cellular level, the action potential dynamics and morphology are generated from the summation of the ionic currents generated by thousands of ion channels distributed in the cardiomyocyte cell membrane (Figure 1.2). The action potential waveform has five phases (0–4). Phase 0, is the action potential upstroke or rapid depolarization phase mediated by I_{Na}. Phase 1, is the notch or rapid repolarization phase mediated by I_{to}, (guinea pig cardiomyocytes lack I_{to}). Phase 2, is the plateau phase, which marks calcium entry into the cell. Phase 3, is the rapid repolarization phase, which is mediated by I_{Ks} and I_{Kr} and returns the membrane potential to its resting state. Phase 4, is the resting state, which is approximately –90 mV in normal cardiomyocytes. The action potential morphology and duration is heterogenous throughout the heart and exhibits region-specific variation. As illustrated in Figure 1.1, the action potential waveform in the sinoatrial node and atrioventricular node have a slow upstroke velocity compared to the atrium and ventricle. Epicardial cells have a more prominent Phase 1 notch and a shortened action potential duration compared to the midmyocardial region [5].

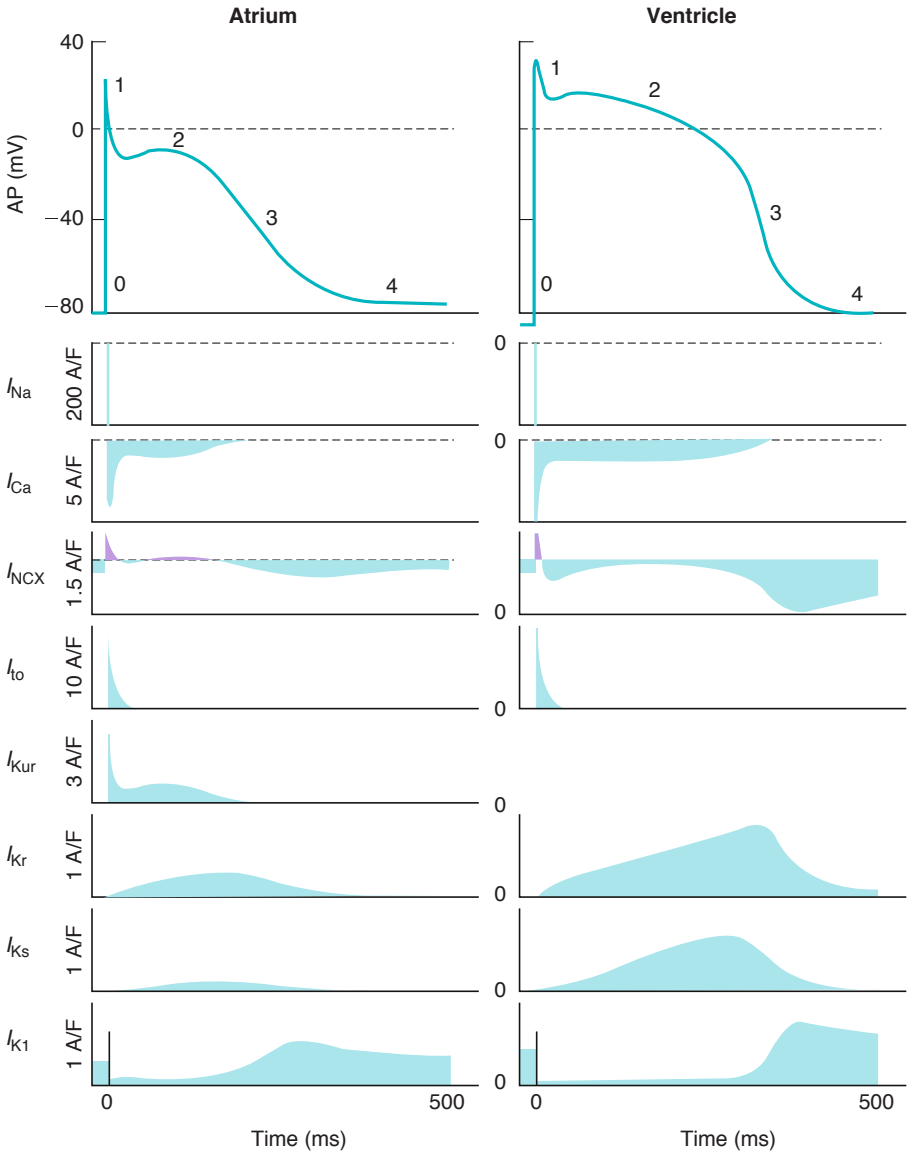

Figure 1.2 | *Currents underlying the action potential waveform*
Schematic of the action potential waveform and the underlying ionic currents (*Left*) Atrial cardiomyocyte action potential (*Right*) Ventricular cardiomyocyte action potential. (*Top panels*) shows the five phases of the action potential (see text). (*Bottom panels*), show how the underlying ionic currents sum to produce the action potential. Inward currents (currents below the line) depolarize the membrane; outward currents (currents above the line) contribute to repolarization. A/F, ampere/farad; I_{Na}, Na^+ current; I_{Ca}, Ca^{2+} current; I_{NCX}, Na^+/Ca^{2+} exchanger current; I_{to}, transient outward K^+ current; I_{Kur}, ultrarapid delayed rectifier K^+ current; I_{Kr}, rapid delayed rectifier K^+ current; I_{Ks}, slow delayed rectifier K^+ current; I_{K1}, inward rectifier K^+ current [4].

At the subcellular level, ion channels and gap junctional channels go through a gating process involving conformational changes of their protein subunits. This results in the opening and closing of the channel in response to voltage changes across the cell membrane and ultimately modulates the flow of ions across the cell membrane.

Elucidating the mechanisms of cardiac arrhythmia requires a thorough understanding of how subcellular changes affect properties at the cellular, tissue, and the whole heart level. This is because new mechanisms of arrhythmia may emerge from the nonlinear interactions between the properties at the different levels of interaction [6].

1.3 Cardiac fibroblasts

The majority of studies of normal and diseased heart have focused primarily on the structural and functional changes of cardiomyocytes. However, the adult heart is composed of a diverse population of non-myocyte cells including: fibroblasts, endothelial cells, pericytes (perivascular cells that wrap around blood capillaries), immune cells, telocytes (a newly described type of interstitial cell [7]) and vascular smooth muscle cells in close proximity to cardiac myocytes. The most prominent non-myocyte cell, cardiac fibroblasts, can account for approximately 30% of cells in the mouse heart to as much as 70% of cells in the rat heart [8, 9], but only a small fraction of the total volume of the heart. This network of cardiac fibroblasts and other non-myocyte cells may play an important role in cardiac physiology and pathophysiology.

Cardiac fibroblasts are often classified based on their morphology. They are flat, spindle-shaped cells with multiple processes (Figure 1.3). Fibroblasts lack a basement membrane, have an extensive Golgi apparatus and a large endoplasmic reticulum to support the production and deposition of extracellular matrix.

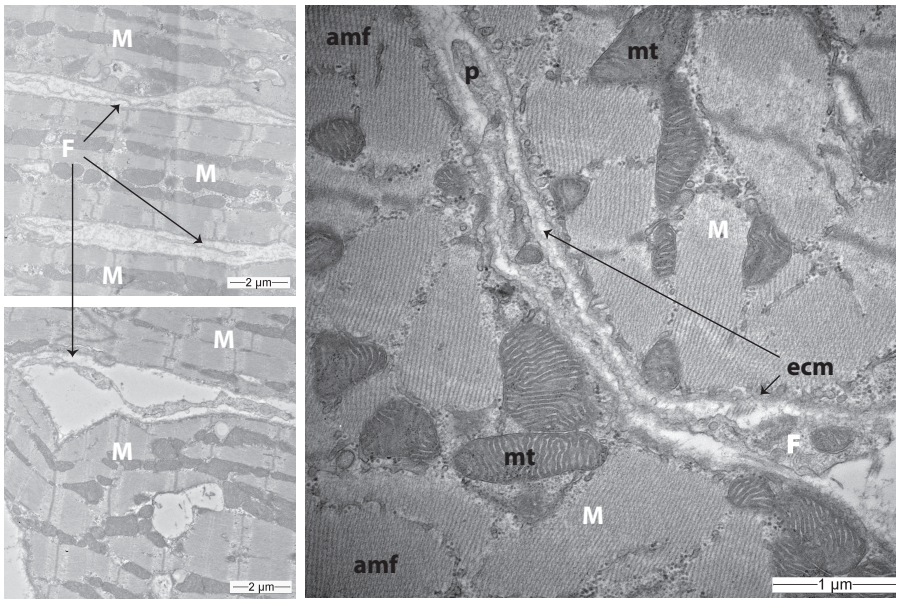

Figure 1.3 | *Electron microscopy images of the adult guinea pig heart.*
Pictured is an electron micrograph of the left ventricle of the adult guinea pig heart. Cardiac fibroblasts (F) are flat spindle shaped cells with long processes (p). They form an intermingled network of cells surrounding cardiac myocytes (M). In higher magnification, the sub-cellular structure of the tissue can be seen including the mitochondrion (mt) and cross sections actin-myosin filaments (amf) of the cardiomyocyte. The fibroblast is shown proximal to a bundle of extracellular matrix (ecm). F, fibroblasts; M, cardiac myocytes; mt, mitochondrion; ecm, extracellular matrix; p, fibroblast process; amf, actin-myosin filament.

Fibroblasts are a phenotypically heterogeneous population. In the normal heart, fibroblasts are thought to be predominantly derived from the epicardium, the epithelial layer covering the outer surface of the heart. Recent studies have shown that during development fibroblasts produced by endothelial-to-mesenchymal transition of the endocardium invade the myocardium and result in a population of endothelially-derived fibroblasts found mostly in the interventricular septum [10]. Moreover, a subset of fibroblasts are derived from the neural crest and are found in the right atrium. However, whether fibroblasts located in fibrotic lesions are derived from resident fibroblasts or transdifferentiated fibroblasts remains unknown. Recent studies have suggested that in the adult heart, fibroblasts with endothelial and epicardial markers responded similarly in proliferative

response to a pressure overload model suggesting that fibroblast phenotype may depend more on local environment than on their developmental origin [11].

Cardiac fibroblast and myofibroblast markers

A major challenge of studying cardiac fibroblasts is the shortage of robust and specific markers. Immunolabeling of the intermediate filament vimentin, is often used to identify fibroblasts and while it is not expressed by cardiomyocytes, it is expressed by numerous other non-myocyte cells in the heart. CD90 (Thy1) is another commonly used marker of cardiac fibroblasts [12], which is also expressed in immunes cells. Fibroblast Specific Protein 1 (FSP1) or S100 calcium binding protein A4 (S100A4) has been extensively used as a fibroblast marker. However, it has been shown to be more frequently associated with immune cells [13]. Goldsmith *et al.* [14] discovered the discoidin domain receptor 2 (DDR2) was specific to cardiac fibroblasts, but labels only a subset of fibroblasts. Recently, collagen1a1-GFP has emerged as more reliable cardiac fibroblasts marker expressed both during development and pathological conditions [10].

Cardiac fibrosis and myofibroblasts

A variety of cardiac diseases such as heart failure, pressure overload, and myocardial infarction results in the differentiation of cardiac fibroblasts into an activated phenotype termed myofibroblasts in responses to mechanical, oxidative stress, and/or pro-inflammatory stimuli. Although the resulting phenotypic changes of myofibroblasts are not well defined, myofibroblasts often express α-smooth muscle actin and display enhanced activity such as contractility, proliferation, motility, and collagen synthesis [15]. Moreover, in pressure overload, a subset of interstitial myofibroblasts upregulate Wilms Tumor 1 and a subset of perivascular fibroblasts express FSP1 [10]. Myofibroblast ac-

tivity is an important step in the reparative process of the heart after cardiac injury. However, when unregulated it can result in destructive patterns of tissue remodeling called cardiac fibrosis (Figure 1.4).

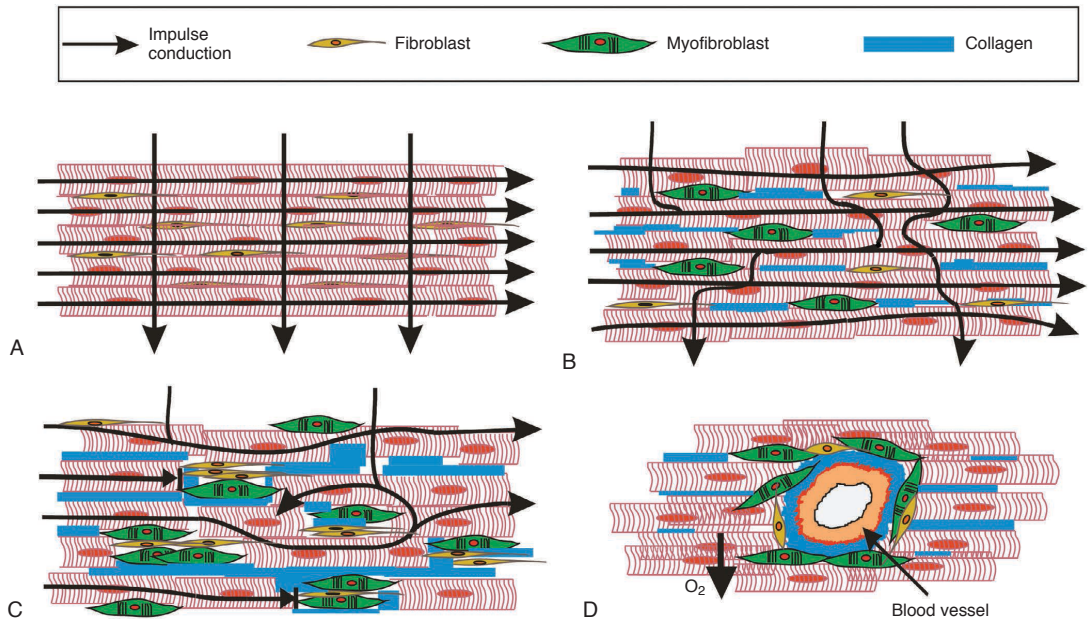

Figure 1.4 | *Illustration of the patterns of cardiac fibrosis*
(*A*) Impulse conduction in the normal heart. (*B*) Interstitial fibrosis in which lateral deposition of collagen and myofibroblasts mainly impedes transverse but not longitudinal impulse conduction. (*C*) Patchy fibrosis where replacement of dead cardiomyocytes with fibrous tissue obstructs both longitudinal and transverse impulse conduction. (*D*) Perivascular fibrosis in which fibrous tissue around blood vessels impairs O_2 supply and conduction in surrounding myocardium. Reproduced with permission from Elsevier [2].

These patterns of fibrosis include: interstitial fibrosis which results in the lateral separation of cardiomyocytes by collagen bundles and myofibroblasts, perivascular fibrosis which results in collagen deposition surrounding blood vessel, and patchy fibrosis which results in long bundles of collagen and myofibroblasts replacing dead cardiomyocytes. One widely studied mechanism by which myofibroblasts promote arrhythmogenesis during cardiac fibrosis suggests that myofibroblasts produce excess extracellular matrix resulting in collagenous septa. These collagenous septa slow propagation, cause zig-zag conduction paths and decouple cardiomyocytes, resulting in a substrate for ar-

rhythmogenic activity [16]. However, there are several emerging mechanisms by which fibroblasts are speculated to interact with cardiomyocytes.

1.3.1 Myocyte-fibroblast interactions

Fibroblasts may interact with cardiomyocytes though chemical (e.g. growth factors, cytokines, that can act through paracine mechanisms), mechanical (e.g. changes in contractility, pressure, and stretch) and electrical signaling (e.g. gating of ion channels and gap junction channels) [17]. One emerging, and somewhat controversial, hypothesis suggests that fibroblasts promote arrhythmogenesis through direct electrical interactions with cardiomyocytes via gap junction channels. Several *in vitro* experiments using normal and diseased heart models have demonstrated that fibroblasts make direct electrical interactions with cardiomyocytes via gap junction channels [18–21]. Using a dye transfer assay, Baudino *et al.* [21] showed in a three-dimensional cell culture model of neonatal rat cardiomyocytes and fibroblasts that cell-cell interactions exist between fibroblasts and cardiomyocytes. Furthermore, Vasquez *et al.* [20] used a gap fluorescence recovery after photobleaching technique to show that intercellular coupling was enhanced between cardiomyocyte monolayers co-cultured with cardiac fibroblasts derived from infarcted rat hearts compared to cardiac fibroblasts derived from normal hearts.

A major challenge in the field has been to translate such cell culture discoveries into native cardiac tissue and the whole heart. Camelliti *et al.* used immunolabeling and a scrape-loading dye transfer method to demonstrate that fibroblasts and cardiomyocytes are functionally coupled in the rabbit sinoatrial node [22]. However, Baum *et al.*, using a similar method, found no fibroblast-myocyte coupling in a canine model of myocardial infarction [23]. To date, it is unsettled whether fibroblast-myocyte coupling exists *in vivo* and whether such discrepancies are due to regional differences (sinoatrial

node vs. ventricle), species related differences (rabbit vs. canine), or disease related modifications in myocyte-fibroblast coupling (see [24, 25] for two recent reviews on this topic). This controversy regarding the role of myocyte-fibroblast coupling *in vivo*, has prompted the development of novel optogenetic strategies to investigate myocyte-fibroblast interactions *in vivo* [25, 26].

1.4 Biophysical properties of cardiac gap junctions

One of the key determinants of cardiac conduction is the axial resistance, which includes the gap junction channel resistance or its inverse conductance. Parameters that determine the conductance of gap junction channels include its static properties such as channel number and single-channel conductance and its dynamic properties such as its kinetics, voltage-dependent gating, and chemical gating [27]. Gap junction channels are highly permeable to ions and their single-channel conductances vary widely (25 pS for Cx45 to 350 pS for Cx37) [28].

Gap junction channel structure

A single gap junctional channel is composed of two hemichannels (connexons) docked head-to-head spanning two bilayer membranes. Each hemichannel is composed of six protein subunits, termed connexins (Cx) and are arranged in a hexagonal pattern around a central pore. This pore allows for direct communication between two neighboring cells. Homomeric hemichannels are composed of a single connexin isoform; heteromeric channels are composed of more than one connexin isoform. In general, gap junction channels are described as homotypic if both hemichannels are composed of the same connexin isoform, or heterotypic if the connexins of the two hemichannels differ

(see Figure 1.5).

Connexin expression in the normal heart

It is well known that cardiomyocytes couple to each other via gap junction channels. Cardiomyocyte gap junctions are organized at the intercalated disks which join neighboring cardiomyocytes in a step-like structure with gap junction channels located at the longitudinal segments of the steps [29]. In the heart, three major Cx isoforms: Cx40, Cx43 and Cx45 form gap junction channels in cell-type-specific combinations. For example, the sinoatrial node and the atrioventricular node express predominantly Cx45. Atrial cells express approximately equal amounts of both Cx43 and Cx40, while ventricular cells predominantly express Cx43 with small amounts of Cx45. Since each gap junction channel exhibits unique static and dynamic properties, it has been postulated that connexin type and distribution may play a functional role in cardiac conduction. For example, the SA and atrioventricular node is thought to require a population of weakly coupled cells. Connexin expression in the SA and atrioventricular node consists of low levels of the highly voltage sensitive and low conductance Cx45 gap junction channels [30].

Connexin expression in cardiac fibroblasts

Ventricular cardiac fibroblasts express Cx43 and Cx45, but express relatively higher levels of Cx45 compared to cardiomyocytes [31, 32], suggesting that a myocyte-fibroblast gap junction channel in the ventricle may be predominantly heterotypic Cx43/Cx45 in composition [33], but may also form homotypic Cx43 and Cx45 channels. However, there may be some species or regional differences in fibroblast gap junction expression. In the rabbit sinoatrial node, fibroblasts express Cx40 around neighboring fibrob-

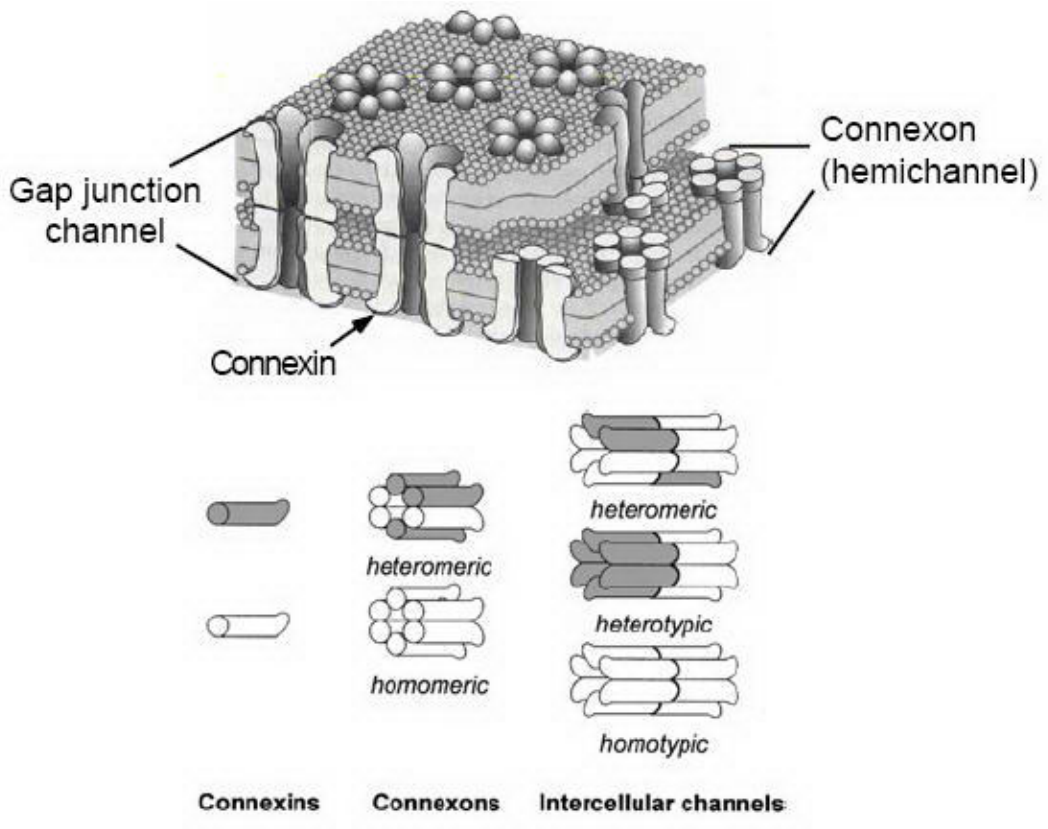

Figure 1.5 | *Gap junction channel configurations*
(top) A single gap junction channel is composed of two hemichannels (or *connexons*) docked head-to-head spanning two bilayer membranes. (bottom) Each hemichannel is composed of six protein subunits, termed *connexins* and are arranged in a hexagonal pattern around a central pore. Connexons (or hemichannels) composed of a single connexin isotype are termed *homomeric*, where as connexons formed from more than one connexin isotype are termed *heteromeric*. When gap junction channels are formed from two identical connexons, they are termed *homotypic* gap junction channels, while gap junction channels formed from different connexons are termed *heterotypic* channels. Source: https://wiki.brown.edu/confluence/display/BN0193S04/gap+junctions

lasts [22]. Gap junctions from the adult mouse heart express Cx40 and Cx43, but no Cx45 was detected [19]. In general, gap junctional plaques between cardiac fibroblasts have been difficult to detect using electron microscopy which suggests that fibroblast gap junctions may be more punctate than that of cardiomyocytes [31].

Connexin expression in the diseased heart

Impairment of cell-to-cell coupling results from alteration in expression and distribution of connexins. It has been suggested that cardiomyocyte connexins might be altered in the failing heart. The most widely documented change is down-regulation of Cx43 in the ventricles of patients with end-stage heart failure [34]. Increased expression of Cx45 in heart failure [35] and increased Cx40 in ischemic heart disease has also been documented [34]. This would result in a generalized increase in the Cx45:Cx43 ratio and in ischemic heart disease localized increase in Cx40:Cx43 ratio. Moreover, changes in fibroblast gap junction protein expression may occur within myocardial infarcts, two fibroblasts phenotypes expressing Cx43 and another expressing Cx45 have been found in a ventricular infarction model of the sheep heart [32]. Furthermore, fibroblasts isolated from an infarcted mouse heart exhibit upregulated Cx43 protein expression [36].

1.4.1 Voltage-dependent gating of connexin channels

An important feature of gap junction channels is that they are regulated by transjunctional voltage (V_j), which is the potential difference between the two coupled cells. The conductance (G_j) of most homotypic gap junction channels is maximal at $V_j = 0$, and decreases symmetrically for both positive and negative V_j values. However, heterotypic gap junction channels have a maximal conductance that is usually shifted away from $V_j = 0$, and the conductance decreases asymmetrically with increasingly positive and

negative V_j. The basic time- and voltage-dependent properties of ventricular cardiac connexins are shown in (Figure 1.6).

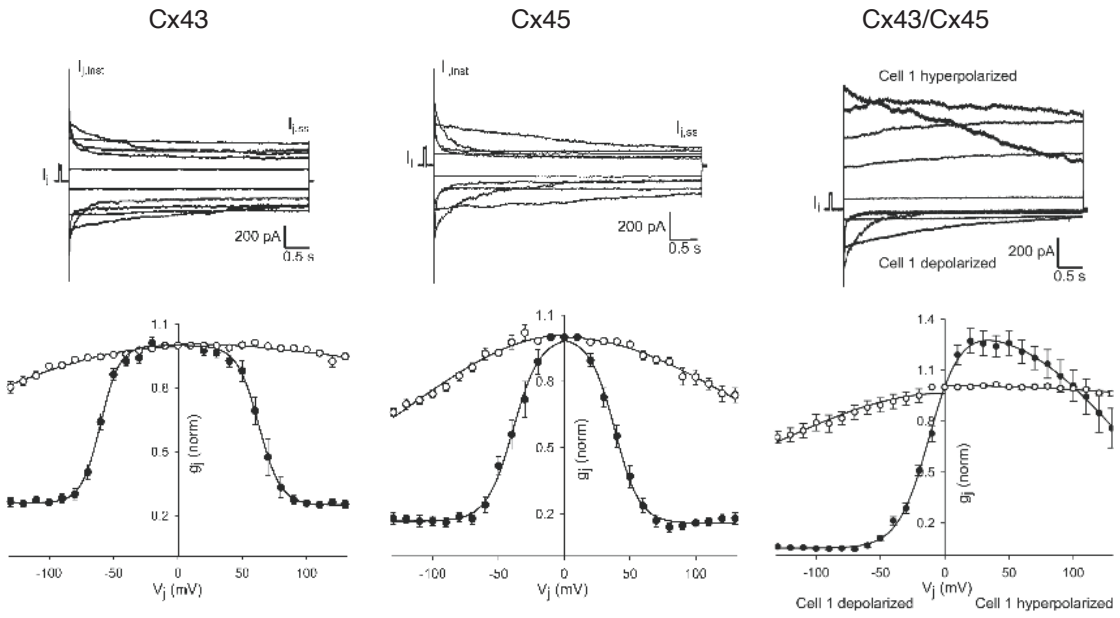

Figure 1.6 | *Dependence of the gap junction conductance on transjunctional potential for homotypic Cx43, homotypic Cx45, and heterotypic Cx43/Cx45 channels.*
Top: Junctional current, I_j, recorded in response to V_j = ±10, ±40, ±70, ±100, and ±130 mV voltage steps applied to cell 1. Instantaneous ($I_{j,inst}$) and steady state ($I_{j,ss}$) was measured from cell 2. Depolarization of cell 1 results in a negative V_j and a downward deflection of I_j. Bottom: Normalized $G_{j,inst}$ (i.e., $G_{j,inst}$ was normalized with respect to G_j associated with a small test pulse prior to each V_j pulse) and $G_{j,ss}$ ($G_{j,ss}$ was normalized with respect to $G_{j,inst}$) for A) Cx43, B) Cx45, and C) Cx43/Cx45. Adapted from [37].

Analysis of junctional current (I_j) records shows that there is a time-dependent inactivation during V_j pulses, and the time constants for voltage-dependent inactivation are also voltage dependent. I_j is relatively constant at small V_j steps, it inactivates slowly at intermediate V_j steps, and inactivates rapidly at large V_j steps. Single gap junctional channels have two prominent states a main state, $\gamma_{j,main}$, and a residual state, $\gamma_{j,residual}$. The presence of this residual state explains the incomplete decay at I_j at large V_j steps. Analysis of I_j records in terms of normalized G_j conductance (i.e., $G_j = I_j/V_j$) is often compared. In the bottom panel of (Figure 1.6) comparing between panels for homotypic

Cx43 and homotypic Cx45, shows that the V_j sensitivity of Cx45 is greater than that of Cx43.

Heterotypic Cx43/Cx45 channels inactivate with high V_j sensitivity when the Cx43 expressing cell is depolarized, but with low V_j sensitivity when cell Cx43 is hyperpolarized (see Cx43/Cx45 panel in Figure 1.6). Thus, heterotypic gap junctions are sensitive to the polarity of V_j and exhibit rectifying behavior. Looking at the normalized G_j-V_j plot, $G_{j,inst}$ decreases moderately with negative V_j and only slightly with positive V_j representing the behavior of $\gamma_{j,main}$. However, $G_{j,ss}$ decreases significantly with negative V_j and increases transiently with positive V_j and thus reflects the opening of previously closed gap junction channels [37].

Chemical gating of connexin channels

Chemical gating of gap junction channels occurs via a slow or "loop" gate which closes channels completely and is distinct from the fast voltage sensitive gate, which only closes channels partially. This gate is thought to mediate Ca^{2+} and H^+ chemical gating of gap junctions [38]. For example, intracellular acidification (i.e., decreases in pH) typically result in a decrease in junctional conductance and permeability to large tracers. This can be an important mechanism of influencing cell-to-cell communication. For example, intracellular acidification of cardiac myocytes could occur as a result of coronary artery occlusion resulting in anaerobic metabolism and therefore the closure of gap junction channels. This process can be cardioprotective, since the closure of gap junctions would create a barrier to isolate the unaffected neighboring cells from the intercellular diffusion of ions, metabolites, and signaling molecules from the injured tissue. However, this phenomenon could also be pro-arrhythmic to the heart, since the electrical barriers created by the closure of gap junctions can become an obstacle to im-

pulse propagation and become a substrate for cardiac arrhythmias [39]. Moreover, the different connexin phenotypes have different sensitivities to pH. Cx45 and Cx40 have the highest and lowest pH sensitivity respectively, with Cx43 being intermediate [40]. Phosphorylation has also been shown to play a role in gap junction gating by modulating the open or closed states of gap junction channels as well as altering the kinetics of transitions between states [41, 42].

1.4.2 Connexin permeability and detection of junctional communication

Gap junction channels are also permeable to endogenous molecules and molecular tracers up to ~1000 Daltons. Molecular tracers are often used to detect the existence of functional gap junction coupling such as the Alexa Flour series of fluorescent tracers and Lucifer Yellow [43, 44]. Permeability to endogenous molecules such as glucose, cAMP, and ADP, is less well explored. Investigating permeability of endogenous molecules is more technically difficulty due to compounds having direct and downstream effects on junctional channels. For example, intercellular calcium signaling is particularly challenging because of the many pathways involved, Ca^{2+} entry can occur via paracrine signaling by extracellular release of ATP resulting in activation of purinergic receptors on a neighboring cell which induces Ca^{2+} entry, or can occur via intercellular diffusion of inositol triphosphate (IP^3), or directly via Ca^{2+} entry through gap junction channels [39].

Several methods have been developed to investigate junctional communication, but most are more suitable to studying cell-to-cell coupling in cell culture, only a few are applicable to tissue level investigations (Figure 1.7). The most commonly used method is the microinjection technique which involves the microinjection of a membrane-impermeable but gap junction permeable fluorescent dye by an electrical or pressure

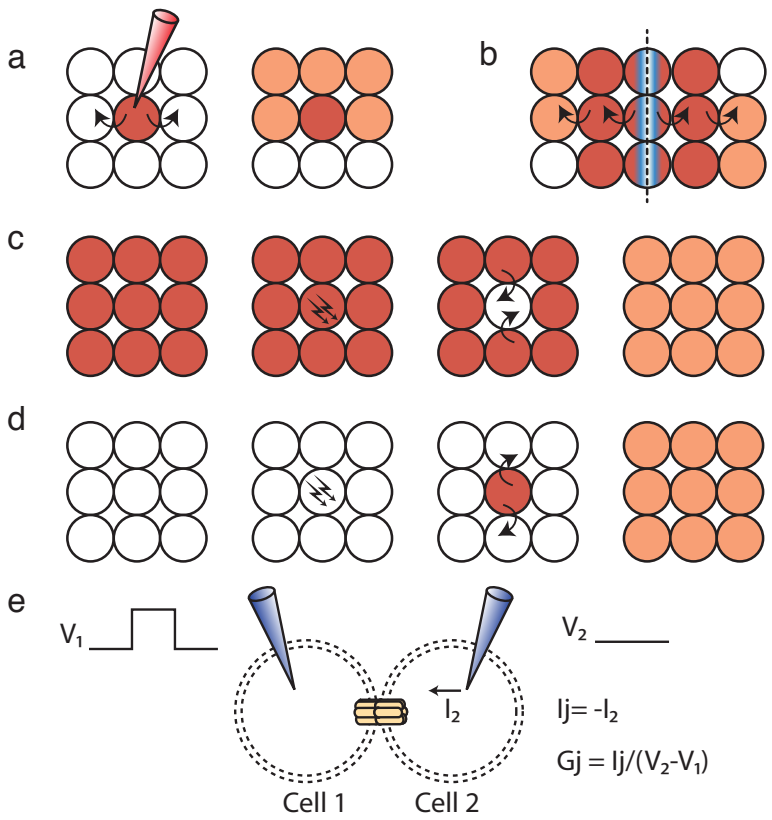

Figure 1.7 | *Commonly used assays for detecting functional gap junction coupling.* A subset of the commonly used assays for detecting functional gap junction coupling may be suitable for investigations *in situ* and *ex vivo*. (*A*) Microinjection - a gap junction permeable dye (red) is injected into center donor cell, the neighboring cells are coupled and show dye has transfer (*B*) Scrape Loading - a gap junction permeable dye (red) and gap junction impermeable dye (blue) are loaded by injury scraping along a line of cells, the gap junction permeable tracer diffuses to neighboring cells indicating coupling. (*C*) Gap-FRAP - cells are loaded uniformly with fluorescent tracer (red), the center cell is photobleached using high power laser. After photobleaching diffusion of dye from surrounding cells back to photobleached cell indicates coupling. (*D*) LAMP - a specialized dye is loaded into cells and photoactivated into a gap junction permeable tracer. If coupled the dye will diffuse to neighboring cells. (*E*) Dual whole-cell patch clamp - a pair of cells are simultaneously patch-clamped. A voltage gradient is established by stepping the voltage of one of the patch-clamped cells and the current is measured in the holding cell and the junctional conductance is then calculated.

pulse into a target cell via a micropipette. If neighboring cells are coupled the fluorescent dye will diffuse to the neighboring cells. Despite being a technically challenging technique, microinjection allows for the screening of functional gap junction permeability in

a specific cell. Thus, this strategy was used in (Chapter 4) to develop a novel method of investigating myocyte-fibroblast interactions in cardiac tissue slices. The scrape loading technique is an alternative to microinjection. Cells are cut or scraped in the presence of a membrane-impermeable and gap junction permeable tracer which is incorporated into the initially scraped cells. The dye will diffuse into neighboring cells if they are functionally coupled by gap junctions. However, this method is limited in its ability to obtain quantitative data and it is not conducive to screening of individual cell types.

The Gap-FRAP (fluorescent recovery after photobleaching) method involves a fluorescent tracer being uniformly introduced into cells. A target area is then photobleached creating a gradient for diffusion. If the photobleached cell is coupled with non-photobleached cells an influx of dye via gap junctions will result. However, this method requires a high intensity laser for photobleaching and it is difficult to avoid photochemical and thermal damage of the sample. The LAMP (local activation of molecular fluorescent probe) method is a recently developed method which uses a newly developed photo-activatable fluorophore, NPE-HCCC2/AM, that can be loaded into cells, and then activated into a fluorescent and gap junction permeable dye using a low dose of ultraviolet light. If neighboring cells are coupled the dye will diffuse to neighboring cells. Finally, the dual whole-cell patch clamp method is the most sensitive method of detecting electrical conductance between neighboring cells. It is important to note that permeability measures and electrical conductance are not equivalent. A voltage gradient is established by stepping the voltage of one of the patch-clamped cells, while holding the other cell constant. The current measured in the holding cell in response to the voltage step (V_j) is the junctional current, (I_j). The junctional conductance (G_j) can be calculated from $G_j = I_j/V_j$. However, this method is technically challenging and requires specialized equipment [45].

1.5 Computational modeling of the heart

1.5.1 Mathematical models of gap junctions

Gap junction channels are a diverse population of channels that vary in conductance and gating properties and the extent of their electrical and metabolic transfer depends on the dynamic properties as discussed above in Section 1.4.1. The general time- and voltage-dependent behaviors of gap junction channels have been incorporated into several computational models discussed below.

Transjunctional-voltage-dependent models

Four-state models Recent models have described transjunctional voltage (V_j)-gating of gap junction channels using a four-state model. This representation describes each hemichannel as having one voltage gate, and thus two gates in series control the gating of the gap junction channel. Each voltage gate can exist in an open or closed residual state. This results in four possible states: 1) OO, in which both gates are open, 2) CO, in which the left gate is close and the right gate is open, 3) OC, in which the left gate is open and the right gate is closed, and 4) CC, in which both gates are closed. This four-state scheme for V_j-gating was used to develop a general mathematical model by Vogel *et al.* [46] , a steady-state model by Chen-Izu *et al* [47] , and a stochastic model by Paulaskas *et al.* [48].

The Vogel *et al.* [46] mathematical model is based on single channel data and consists of two hemichannel models connected in series with each hemichannel containing a voltage gate; each hemichannel transitions between two non-zero states, a high (H) and low (L) conductance state gated by the transjunctional voltage, V_j, across each

hemichannel. The gates function independently, leading to four conformation states of the combined channel, HH, HL, LH, and LL.

The Chen-Izu *et al.* [47] mathematical model focused on the steady state behavior of V_j-gating. They developed a modified Boltzmann equation that allowed for the simultaneous fitting of positive and negative polarities of V_j. The Chen-Izu model assumes that an intact gap junction channel has one open channel conductance and one residual conductance, as opposed to the Vogel model which has four possible conductances. Two models were developed, a contingent gating model in which the gating of one channel depends on the state of the opposed channel, and an independent gating model which assumes that the two voltage gates in the model do not interact other than through the distribution of V_j.

A four-state stochastic model of contingent gating of gap junction channels containing two fast gates and V_j sensitive gating was developed by Paulaskas *et al.* [48]. The model assumes that each channel has an open state and a residual state, and that both states rectify. Gates can have the same or different gating polarities. Each hemichannel gate can be in the open or closed states which correspond to the open state and the residual state of the hemichannel, respectively. The single-cannel conductances of the open and residual state rectify, and thus depend on V_j. The model defines for a given time whether individual channels stay in the same state or change their state. This model has also been extended into a stochastic 16-state model of voltage gating of gap junction channels by incorporating the slow gating mechanism [49].

Data-based model Lin *et al.* [50] developed a model to describe the unique features of V_j gating between cardiomyocyte cells. This gating is thought to occur when conduction velocity is very slow ($\leq$10 cm/s) and the intercellular conduction delay is large

enough to produce V_j gradients equal to the magnitude of a ventricular action potential. The major component of the model is the two inactivation components and two recovery components based directly from data obtained by applying a ventricular action potential to paired neonatal murine ventricular myocytes in dual whole cell voltage clamp experiments. Inactivation is induced when V_j increases above a certain threshold value and is removed when V_j is in the resting state. They incorporated a behavior described as facilitation which occurs only in ventricular cardiomyocyte cell pairs. Facilitation is observed as an increase in G_j above the initial peak values during the final repolarization phase of the action potential.

1.6 Mathematical models of cardiac fibroblasts

A major advancement in our understanding of fibroblast-myocyte interactions was the discovery that cardiac fibroblasts express time- and voltage-dependent and inward rectifying K^+ currents [51, 52]. Computational models incorporating the electrophysiological properties of these conductances are described as "active" models. Prior to this discover, cardiac fibroblasts were modeled as purely "passive" electrical loads.

Ventricular fibroblast model

Passive model In the passive fibroblast model, the membrane capacitance is connected in parallel to an ohmic resistance. Therefore, the membrane potential can be represented by the ordinary differential equation: $C_f \frac{dV_f}{dt} = -G_f (V_f - E_f)$, where C_f is the fibroblast membrane capacitance, V_f is the membrane potential of the fibroblast, E_f is the fibroblast resting membrane potential, and G_f is the fibroblast membrane conductance [53]. This model does not accurately represent all of the electrophysiological properties of

cardiac fibroblasts. However, due to the ability to independently modify E_f and G_f this model has been extensively used to systematically investigate these basic fibroblast electrophysiological parameters in multi-scale computational models of fibroblast-myocyte interactions (see Section 1.7).

Active model Active fibroblast models have been developed by Sachse *et al.* [54], Jacquemet *et al.* [55], and MacCannell *et al.* [56], with the MacCannell model being the most widely used. The MacCannell *et al.* model includes four membrane currents: an inwardly-rectifying K^+ current, a time- and voltage-dependent delayed-rectifier K^+ current, an electrogenic Na^+/K^+-ATPase, and a time-independent background Na^+ conductance. The magnitude and kinetics of the inwardly rectifying and delayed-rectifier K^+ currents are based on experimental measurements [51, 52] from fibroblasts isolated from the adult rat ventricle. The Na^+/K^+-ATPase and the background Na^+ current were introduced to enable K^+ and Na^+ ion homeostasis. The resting membrane potential of the uncoupled fibroblast is set to –49.6 mV and the membrane capacitance is 6.3 pF.

The Sachse model is based on the same experimental data as the MacCannell model and therefore also includes an inwardly rectifying current I_{Kir} and a time- and voltage-dependent outward current I_{Shkr} (i.e., the K_v family) but with different mathematical formulations. They also incorporated a nonspecific background current I_b to maintain the resting membrane potential of –58 mV and they modeled a smaller membrane capacitance of 4.5 pF. The Jacquemet model is a simplified active model developed by fitting a three-dimensional polynomial to the recorded current-voltage relationship of the cardiac fibroblast and incorporating a delayed current activation. The resting membrane potential was set to –58 mV.

Atrial fibroblast model

Recent experimental studies implicate potentially important differences between cardiac fibroblasts derived from ventricular versus atrial tissue [57–59]. This has led to a subset of models representing the atrial fibroblast phenotype. Chatelier *et al.* have shown that the differentiation of human atrial fibroblasts into myofibroblasts is associated with *de novo* expression of voltage gated Na^+ currents [58, 59]. Koivumaki *et al.* [59] integrated these electrophysiological findings into a mathematical model of human atrial myofibroblasts [60]. However, the introduction of Na^+ currents into the model did not result in significant changes in the fibroblast electrophysiology nor any action potential-like responses on stimulation. This may be due to the inactivation of the Na^+ current by the relatively depolarized resting membrane potential of the cardiac fibroblast.

There are still significant gaps in our understanding of fibroblast electrophysiological properties due to the limited availability of electrophysiological data and the difficulty of accurately recording from such small cells [61]. In an attempt to overcome such limitations, computational studies have explored the contribution of a wide range of fibroblast properties by varying parameters such as: membrane capacitance, C_f, membrane conductance, G_f, resting membrane potential, E_f, gap junctional conductance, G_j, and fibroblast-myocyte ratio and quantifying their effects on fibroblast-myocyte coupling.

1.7 Simulations of fibroblast-myocyte coupling

Cardiac fibroblasts have been described as a “leaky capacitor”: charging during the diastolic and upstroke phase of the action potentialaction potential and then leaking current during the systolic phase when the voltage-dependent currents of the cardiac fibroblast

are activated by depolarization [62]. This in turn can cause modifications in the cardiomyocyte action potential morphology when/if coupled to a fibroblast. Three hypothetical types of fibroblast-myocyte coupling configurations in the intact heart have been proposed [63]. First, "zero-sided" coupling in which fibroblasts do not interact directly with cardiomyocytes but instead create obstacles similar to collagenous septa leading to discontinuous conduction. Second, "single-sided" coupling in which fibroblasts are connected to groups of myocytes and can act as current sources or sinks. Third, "double-sided coupling" in which fibroblast-fibroblast connections interlink myocytes resulting in new conduction pathways or conduction bridges between uncoupled myocytes. In this section, we review the existing computational models of fibroblast-myocyte coupling in the form of cell pairs/clusters (i.e., a single cardiomyocyte coupled to one or more cardiac fibroblasts), one-dimensional (1D) cables, two-dimensional (2D) sheets, and three-dimensional (3D) models and discuss their contribution to our understanding of the mechanism of fibroblast-myocyte interactions.

Interactions with ventricular myocyte Models

Effects on action potential morphology

MacCannell *et al.* used computational models of cell pairs using the Tusscher-Noble-Noble-Panfilov (TNNP) model of the human ventricular cardiomyocyte [64] and their active model of an adult ventricular fibroblast (Section 1.6) to show that fibroblast-myocyte coupling modifies the cardiomyocyte action potential morphology. fibroblast-myocyte coupling resulted in a hyperpolarized action potential plateau, shortened action potential duration, depolarizations of the resting membrane potential, and corresponding action potential waveform-dependent changes in the ionic currents of the cardiomyocyte. They found that the magnitude of these changes in action potential were depen-

dent on the membrane properties of the cardiac fibroblasts, the gap junction conductance, and the number of fibroblasts. The dependency of these action potential changes on fibroblast membrane properties were further explored by Xie *et al.* [65] who described such changes as a function of the two components of the fibroblast-myocyte gap junctional current: 1) an early transient outward (I_{to})-like component, and 2) a late background current component. They performed simulations using a modified version of the Luo and Rudy (LR1) model [66] and the passive fibroblast model (Section 1.6) and systematically modified the fibroblast membrane conductance, G_f, and resting membrane potential, E_f, and observed its effects on the two components of the gap junctional current and on action potential morphology during fibroblast-myocyte coupling. They found that when G_f is small, the early component of the the gap junctional current behaves similar to I_{to} (i.e., it is activated rapidly during the early phase 1 of the action potential and can influence action potential amplitude and action potential duration) and results in prolongation of the action potential duration. When G_f is large, the late component of the gap junctional current plays a more prominent role in modifying the action potential duration. The parameter E_f affects the crossing voltage in which the fibroblast voltage is more depolarized than the cardiomyocyte membrane potential. Therefore, when G_f is large and E_f is more depolarized, the late component of the gap junctional current is mainly an inward current for the cardiomyocyte resulting in the prolongation of its action potential duration. However, when G_f is large and E_f is more hyperpolarized (i.e., –80 mV) the late component is mainly an outward current and thus shortens action potential duration.

As will be discussed in the next section, fibroblast-myocyte coupling can also have significant affects on cardiac impulse propagations and cardiomyocyte excitability as demonstrated by *in vitro* experiments and simulations using 1D cables, and 2D tissue sheets.

Effects on conduction velocity and excitability

Conduction velocity and fibroblast density Experimental investigations *in vitro* have demonstrated that myofibroblasts can directly modify conduction velocity by direct electrical interactions with cardiomyocytes. For example, Miragoli *et al.* [67] measured conduction velocity and upstroke velocity (dV/dt_{max}) from optical mapping recordings of stimulated strands of cultured neonatal rat cardiomyocytes coated with myofibroblasts. Interestingly, they found a biphasic dependence of conduction velocity and dV/dt_{max} on myofibroblast density. Using microelectrode recordings, they demonstrated that these fibroblast-mediated changes were associated with cardiomyocytes strands becoming depolarized from –78 mV to –50 mV.

To help explain these findings, Xie *et al.* [62] developed various 2D tissue sheet models based on native cardiac tissue structure in order to investigate the effects of fibroblast-myocyte ratio on conduction velocity. In their cell-attached model, in which a layer of cardiac fibroblasts were modeled on top of a monolayer of cardiomyocytes, they observed a similar biphasic relationship between conduction velocity and fibroblast-myocyte ratio as seen in *in vitro* experiments. They suggested that conduction velocity first increased by the fibroblast bringing the cardiomyocyte membrane potential closer to the threshold for I_{Na} but then decreased as the increasing fibroblast density resulted in a shift in the cardiomyocyte membrane potential and I_{Na} inactivation. However, using their random fibroblast insertion model, which represents the coculture of cardiomyocytes interspersed with cardiac fibroblasts, they found a monotonic decrease in conduction velocity with increasing fibroblast-myocyte ratio. They also found that the membrane potential of the fibroblast, E_f, also has an effect on conduction velocity: when E_f was set to a more hyperpolarized value of –80 mV the fibroblast had no effect on the cardiomyocyte resting membrane potential and there was a more linear relationship be-

tween conduction velocity and the fibroblast-myocyte ratio.

However, these results were opposite of the experimental findings of Miragoli *et al.*, who found a biphasic relationship with endogenous/interspersed fibroblast-myocyte co-cultures, but a monotonic relationship when cardiac fibroblasts were plated on top of a cardiomyocyte monolayer. One suggested explanation of this discrepancy is that in experimental conditions where cardiac fibroblasts were plated on top of a cardiomyocyte monolayer, the latter may have still had significant endogenous/interspersed fibroblast content which might be high enough to obscure the increasing conduction velocity phase. Other yet to be explored mechanisms may also exist.

It has been shown that cardiac tissue microstructure consists of laminar clefts or cleavage planes with fibroblasts often localized in the cleft spaces. Surprisingly, their 2D model of fibroblasts inserted into laminar clefts between cardiomyocytes resulted in a monotonic increase in conduction velocity with increasing fibroblast density [62]. This behavior is thought to be due to cardiac fibroblasts forming bridge-like pathways or due to the downstream depolarization of a cardiomyocyte by a depolarized cardiac fibroblast within the cleft.

Conduction velocity and gap junctional conductance Zlochiver *et al* [68] used a combination of *in vitro* optical mapping experiments and computational modeling studies to investigate the effects of fibroblast-myocyte gap junctional conductance on conduction velocity. Gap junctional conductance was modified experimentally using gene expression level modification of connexin 43 (Cx43) channels, in which, Cx43 RNA interference resulted in a 90% reduction in myofibroblast Cx43 expression, and Cx43 over expression resulted in 99% overexpression of Cx43. Their 2D computational model, designed to mimic the cell cultures experiments, used a ventricular cardiomyocyte model

and the cardiac fibroblast model that included the outward rectifying current-voltage relationship (Sec. Section 1.6). In both simulations and experiments, there was a biphasic relationship between conduction velocity and gap junctional conductance, with an initial decrease in conduction velocity followed by an increase as gap junctional conductance increased. One hypothesis for the biphasic nature of this relationship is that insufficient charge is being transmitted to downstream cardiomyocytes during low levels of coupling, resulting in alternative conduction pathways and conduction slowing. However, above a certain threshold of gap junction conductance there is enough charge transmitted through the myofibroblasts to excite downstream cardiomyocytes and thus increase conduction velocity.

Spontaneous activity Miragoli *et al.* [69] used strands of cultured neonatal rat ventricular cardiomyocytes coated with myofibroblasts to demonstrate that fibroblast-myocyte coupling can result in depolarization-induced ectopic activity. The percentage of preparations with spontaneous activity increased with increasing myofibroblast density. Such activity was not observed in control cardiomyocyte strands without direct myofibroblast contact. They demonstrated that changes in membrane polarization can affect the rate of occurrence of spontaneous activity by using current clamp injections of constant current pulses in individual cardiac myocytes in the range of membrane depolarizations seen in fibroblast coated cardiomyocyte cultures.

Greisas *et al.* [70] used a 2D monolayer tissue model, including human ventricular cardiomyocytes represented by the TNNP model [64] and the MacCannell cardiac fibroblast model, and added support to the hypothesis that spontaneous activity occurs as a result of fibroblast-mediated depolarization of the cardiomyocyte resting membrane potential. In their monolayer tissue model, cardiac fibroblasts were embedded between ventricular cardiomyocytes in a single layer. In this configuration, spontaneous excita-

tions were observed frequently. For example, spontaneous activity occurred with low fibroblast-myocyte ratios from 0.5 to 1.75 with gap junctional conductances of 0.02 nS to 0.08 nS. The spontaneous excitation occurred in clusters when the coupled fibroblast modified the membrane potential of the neighboring cardiomyocytes to their excitation threshold. At low coupling the fibroblast effect was not strong enough to depolarize the cardiomyocyte, while at very high coupling the large depolarization and inactivation of sodium channel activity prevented the cardiomyocytes from recovering from inactivation after the action potential was elicited. Similarly, automaticity was suppressed by very high fibroblast density due to the inability of the cardiomyocytes to recover from the large depolarization imposed by the coupled cardiac fibroblasts. Thus, the spontaneous activity only occurred at intermediate values of gap junctional conductance and when the fibroblast density was low.

Effects on vulnerability to reentry

Heart failure can arise from numerous cardiac pathologies and can result in various degrees of electrical and structural remodeling depending on the particular etiology. Ionic remodeling and fibrosis have been identified as key players in the mechanisms for arrhythmogenesis associated with heart failure. Gomez *et al.* modeled ionic and structural remodeling in heart failure using 1D cables and 2D computational models [71, 72]. They used the Grandi *et al.* [73] and the O'Hara *et al.* [74] human ventricular action potential model with heart failure ionic remodeling and the MacCannell fibroblast model for structural remodeling. When clusters of fibroblasts were inserted randomly into a cardiomyocyte strand action potential duration dispersion increased to 70 ms from 24 ms with 10% fibrosis. Such regional dispersion of repolarization can create a substrate for the development of reentry. Moreover, transmural dispersion of repolarization was also enhanced. Both action potential duration dispersion and transmural dispersion of

repolarization showed a biphasic relationship with fibroblast density, with both action potential duration dispersion and transmural dispersion of repolarization first increasing with 10% fibrosis, but then decreasing when fibroblast density was increased to 20%.

Furthermore, they investigated the role of fibrosis in reentry generation in several degrees of fibrosis [72]. They found that spontaneous activity occurred as a result of the depolarization of the cardiomyocyte membrane potential by the surrounding fibroblasts. In their heart failure remodeling simulations they found that low fibrosis (4%) could not induce reentrant activity, but at 14.5% there was a vulnerable window for reentry initiation of 20 ms. Thus, when enough fibrosis is present, the action potential duration and effective refractory period of some cardiomyocytes are shortened so that when a premature stimulus is applied, part of the ventricular tissue has recovered enough to become excited, generating wave break and spiral waves. However, at even higher fibrosis (40%) reentrant activity was not observed because the depolarizing wave front reached very low potentials, leading to only small electronic voltage changes. They also observed a slight decrease in the rotation frequency of the spiral wave with increased fibrosis. This decrease in spiral wave frequency was also observed in experimental studies by Zlochiver *et al.* [68] and is consistent with fibroblast-loading induced conduction slowing (Section 1.7).

Using a 3D computational model based on diffusion tensor magnetic resonance images of the rabbit heart, McDowell *et al.* [75] investigated the role of fibroblast-myocyte coupling in the mechanism of arrhythmia generation during myocardial infarction. The peri-infarct zone was modeled as having a fibroblast density ranging from 10–30%, while the scar was model as 80% or 0% fibroblast density. Using the Mahajan *et al.* [76] model of the rabbit ventricular action potential and the MacCannell fibroblast model, they showed that susceptibility to arrhythmia in the infarcted heart depends on myofi-

broblast density. At low densities myofibroblasts did not alter arrhythmia propensity, at intermediate densities myofibroblasts caused additional action potential duration shortening and increased arrhythmia propensity, at high densities myofibroblasts protected against arrhythmia by causing resting depolarization and blocking propagation. The underlying mechanism was shown to be fibroblast-myocyte coupling depolarizes the resting membrane potential of the cardiomyocyte, which causes a partial inactivation of I_{Na} and contributes to conduction failure.

Effects on early afterdepolarizations

Since it is difficult to modify gap junctional conductance systematically in an *in vitro* experiment, Nguyen *et al.* [77] used a hybrid computational modeling and dynamic-clamp approach (see Section 1.8) to investigate fibroblast-myocyte coupling between a real rabbit ventricular cardiomyocyte and a virtual cardiac fibroblast. They showed that fibroblast-myocyte coupling increased susceptibility to both oxidative stress-induced and hypokalemia-induced early afterdepolarizations [77]. They deduce that these effects where dependent on the early I_{to}-like component of the gap junctional current by performing experiments in which they selectively eliminated the early component and observed suppression of early afterdepolarizations. The I_{to}-like component results in lowering of the action potential plateau into the range that allows for reactivation of L-type calcium current. They also found that the increased early afterdepolarization susceptibility was especially enhanced when the resting membrane potential of the cardiac fibroblast, E_f, was more depolarized (–25 mV). It is worth noting that much smaller changes in fibroblast-myocyte coupling was needed to result in early afterdepolarization formation compared to effects on conduction velocity.

Interactions with atrial myocyte models

Atrial fibrosis is associated with pathological conditions such as persistent and permanent atrial fibrillation. Ashihara *et al.* [78] hypothesized that electronic interactions between atrial myocytes and fibroblasts may play a role in the genesis of complex fractionated atrial electrograms and proposed that targeting these fibroblast-associated complex fractionated atrial electrogram sites could terminate induced atrial fibrillation. Using a 2D sheet computational model of human atrial tissue with cardiomyocytes represented by the Courtemanche model [79] and the MacCannell fibroblast model, they showed that the incorporation of high-density fibroblasts (50% fibrotic area) resulted in more spiral wave meandering within or around the fibrotic areas and these meandering waves were sustained longer than controls without fibrotic areas. Moreover, computed bipolar electrogram recordings from the fibrotic areas showed complex fractionated atrial electrograms. Simulations of complex fractionated atrial electrogram-targeted ablation resulted in spiral wave reentry termination shortly after ablation. This suggests that the fibroblast-mediated decrease in action potential duration, conduction velocity, and myocardial excitability are required for complex fractionated atrial electrograms. In contrast, simulated collagen accumulation (i.e., low density (18.8%) or high density (37.5%) replacement of fibrotic area by non-excitable and non-conductive tissue) showed less frequent wave breakups and no complex fractionated atrial electrogram sites in the bipolar electrogram. However, the manifestation of such complex fractionated atrial electrograms could be related to the direction of the incident waveform relative to the underlying spatial organization of the fibrosis as demonstrated in a 2D computational model study by Campos *et al.* [80]. Catheter ablation targeting these collagen accumulation regions could not terminate spiral waves.

McDowell *et al.* [81] developed a 3D computational model of human left atrial tis-

sue with specific geometry from a patient with persistent atrial fibrillation including models with combinations of gap junction remodeling, collagen deposition, and myofibroblast proliferation with electronic or paracrine effects. They found that gap junction remodeling was the primary contributor to conduction block and inclusion of other fibrotic lesions did not suppress it. Furthermore, all simulations which incorporated both gap junction remodeling and myofibroblast coupling resulted in reentry after conduction block, thus indicating myofibroblasts are critical for reentry formation.

1.8 Dynamic-clamp technique

The dynamic-clamp technique allows for real-time feedback between computational models and *in vitro* patch-clamped cells (Figure 1.8). Traditional methods of accessing electrical properties of excitable cells used current clamp or voltage clamp methods. During current clamp, a current value is set by the amplifier and injected into the cardiomyocyte and the membrane potential is recorded. In voltage clamp, the membrane potential value is set by the amplifier and the current injected into the cardiomyocyte to maintain this set voltage is recorded. Dynamic clamp is an extension of the current clamp mode in which a current is set by the amplifier and injected into the cardiomyocyte in current clamp mode. However this current is a function of the membrane potential of the patch-clamped cardiomyocyte. This current can be used for example: to represent an additional ionic conductance (in the case of "model clamp") or a coupling current (in the case of "coupling clamp"). Thus, the dynamic clamp uses a feedback loop in, which the membrane potential is measured using a patch-clamp amplifier, the measured voltage is fed into a computer that calculates the current to be injected and then sends this information to the patch clamp amplifier to inject this current.

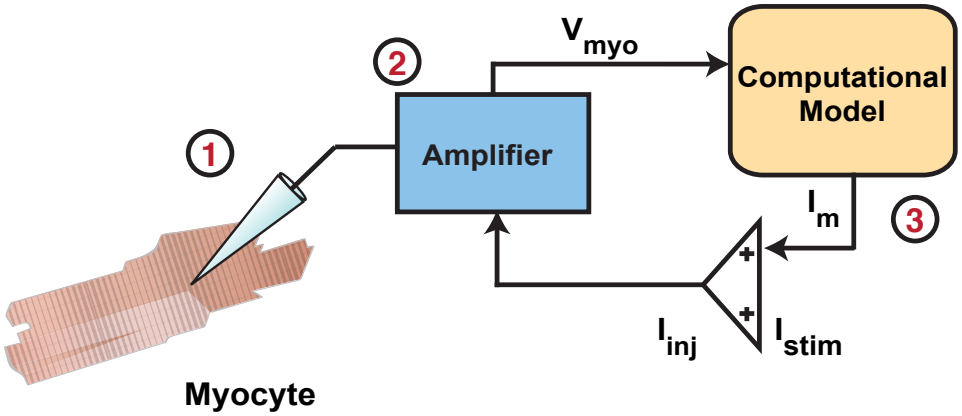

Figure 1.8 | *Dynamic-Clamp method is a hybrid computational modeling and patch clamp electrophysiology technique*
Computer calculations are perfomed using RTXI Dynamic-clamp framework, and *in vitro* recordings are performed using a patch-clamp amplifier. (*1*) Measure voltage V_{myo}. (*2*) Input V_{myo} to model. (*3*) Computational model is used to calculate I_{inj} current in real-time.

1.9 Multiscale study of gap junctions in myocyte-fibroblast interactions

This study investigates how the subcellular properties of voltage-dependent gap junction channels are linked to changes in myocyte-fibroblast interactions at the cellular level and tissue level (Figure 1.9). To do so, a mathematical model of the gap junction channels involved in myocyte-fibroblast interactions was developed. Then, an investigation into how changes in gap junction channel phenotypes between myocytes and fibroblasts affect myocyte action potential morphology using the dynamic-clamp technique was conducted (Chapter 2). Next, an investigation into whether changes in gap junctions at the subcellular level and cellular level combine at the tissue level and result in modifications in impulse propagation was conducted (Chapter 3). Finally, a novel strategy to experimentally investigate myocyte-fibroblast interactions in a multicellular

environment was developed (Chapter 4).

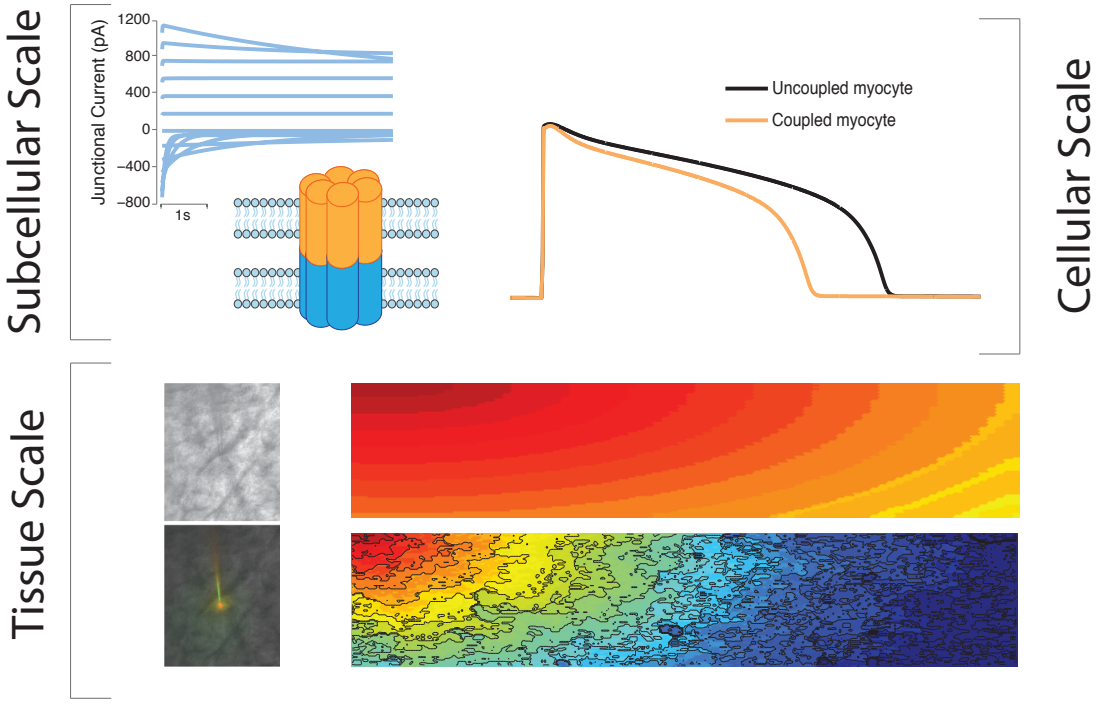

Figure 1.9 | *Multiscale study of gap junctions in myocyte-fibroblast interactions* This study, investigates how the *subcellular scale* changes in voltage dependent gating of gap junction channels are linked to changes in the myocyte-fibroblast coupling and result in changes in cardiomyocyte action potential morphology at the *cellular scale*. Furthermore, this study investigates how changes in myocyte-fibroblast gap junction channel phenotypes at the *tissue scale* alter fibroblast mediated changes in impulse propagation and conduction velocity using tissue simulations. Finally, a novel strategy to investigate the degree of interconnections between myocytes-fibroblast using cardiac tissue slices is developed.

BIBLIOGRAPHY

1. Brown, T., Krogh-Madsen, T. & Christini, D. J. Computational Approaches to Understanding the Role of Fibroblast-Myocyte Interactions in Cardiac Arrhythmogenesis. *BioMed Research International* (2015).

2. Zipes, D. P. & Jalife, J. *Cardiac Electrophysiology: From Cell to Bedside* (Elsevier Health Sciences, 2013).

3. King, J. H., Huang, C. L. H. & Fraser, J. A. Determinants of myocardial conduction velocity: implications for arrhythmogenesis. *Front Physiol* (2013).

4. Zipes, D. P. & Jalife, J. *Cardiac Electrophysiology: From Cell to Bedside* (Zipes, 2009).

5. Grant, A. O. Cardiac Ion Channels. *Circulation: Arrhythmia and Electrophysiology* (2009).

6. Qu, Z. & Weiss, J. N. Mechanisms of Ventricular Arrhythmias: From Molecular Fluctuations to Electrical Turbulence. *Annu. Rev. Physiol.* (2015).

7. Gherghiceanu, M. & Popescu, L. M. Cardiac telocytes — their junctions and functional implications. *Cell Tissue Res.* (2012).

8. Nag, A. C. Study of Non-Muscle Cells of the Adult Mammalian Heart - a Fine-Structural Analysis and Distribution. *Cytobios* (1980).

9. Banerjee, I, Fuseler, J. W., Price, R. L., Borg, T. K. & Baudino, T. A. Determination of cell types and numbers during cardiac development in the neonatal and adult rat and mouse. *AJP: Heart and Circulatory Physiology* (2007).

10. Moore-Morris, T., Cattaneo, P., Pucéat, M. & Evans, S. M. Origins of cardiac fibroblasts. *Journal of Molecular and Cellular Cardiology* (2016).

11. Ali, S. R. *et al.* Developmental heterogeneity of cardiac fibroblasts does not predict pathological proliferation and activation. *Circ. Res.* (2014).

12. Hudon-David, F., Bouzeghrane, F., Couture, P. & Thibault, G. Thy-1 expression by cardiac fibroblasts: Lack of association with myofibroblast contractile markers. *Journal of Molecular and Cellular Cardiology* (2007).

13. Kong, P., Christia, P., Saxena, A., Su, Y. & Frangogiannis, N. G. Lack of specificity of fibroblast-specific protein 1 in cardiac remodeling and fibrosis. *AJP: Heart and Circulatory Physiology* (2013).

14. Goldsmith, E. C. *et al.* Organization of fibroblasts in the heart. *Dev. Dyn.* (2004).

15. Vasquez, C., Benamer, N. & Morley, G. E. The cardiac fibroblast: functional and electrophysiological considerations in healthy and diseased hearts. *J. Cardiovasc. Pharmacol.* (2011).

16. De Jong, S., van Veen, T. A. B., van Rijen, H. V. M. & de Bakker, J. M. T. Fibrosis and cardiac arrhythmias. *J. Cardiovasc. Pharmacol.* (2011).

17. Howard, C. M. & Baudino, T. A. Journal of Molecular and Cellular Cardiology. *Journal of Molecular and Cellular Cardiology* (2013).

18. Chilton, L, Giles, W. R. & Smith, G. L. Evidence of intercellular coupling between co-cultured adult rabbit ventricular myocytes and myofibroblasts. *The Journal of Physiology* (2007).

19. Louault, C., Benamer, N., Faivre, J.-F., Potreau, D. & Bescond, J. Implication of connexins 40 and 43 in functional coupling between mouse cardiac fibroblasts in primary culture. *Biochimica et Biophysica Acta (BBA) - Biomembranes* (2008).

20. Vasquez, C *et al.* Enhanced Fibroblast-Myocyte Interactions in Response to Cardiac Injury. *Circ. Res.* (2010).

21. Baudino, T. A. *et al.* Cell Patterning: Interaction of Cardiac Myocytes and Fibroblasts in Three-Dimensional Culture. *MAM* (2008).

22. Camelliti, P., Green, C. R., LeGrice, I. & Kohl, P. Fibroblast network in rabbit sinoatrial node: structural and functional identification of homogeneous and heterogeneous cell coupling. *Circ. Res.* (2004).

23. Baum, J. R., Long, B, Cabo, C & Duffy, H. S. Myofibroblasts cause heterogeneous Cx43 reduction and are unlikely to be coupled to myocytes in the healing canine infarct. *AJP: Heart and Circulatory Physiology* (2012).

24. Duffy, H. S. Fibroblasts, myofibroblasts, and fibrosis: fact, fiction, and the future. *J. Cardiovasc. Pharmacol.* (2011).

25. Kohl, P. & Gourdie, R. G. Fibroblast-myocyte electrotonic coupling: does it occur in native cardiac tissue? *Journal of Molecular and Cellular Cardiology* (2014).

26. Quinn, T. A., Camelliti, P., Siedlecka, U & Poggioli, T. Cell-specific expression of voltage-sensitive protein confirms cardiac myocyte to non-myocyte electrotonic coupling in healed murine infarct border tissue. *Circulation* (2014).

27. Desplantez, T., Dupont, E., Severs, N. J. & Weingart, R. Gap Junction Channels and Cardiac Impulse Propagation. *J Membrane Biol* (2007).

28. Goldberg, G. S., Valiunas, V. & Brink, P. R. Selective permeability of gap junction channels. *Biochimica et Biophysica Acta (BBA) - Biomembranes* (2004).

29. Severs, N. J. The cardiac gap junction and intercalated disc. *Int. J. Cardiol.* (1990).

30. Giovannone, S, Remo, B. F. & Fishman, G. I. Channeling diversity: Gap junction expression in the heart. *HRTHM* (2012).

31. Zhang, Y. *et al.* Connexin43 Expression Levels Influence Intercellular Coupling and Cell Proliferation of Native Murine Cardiac Fibroblasts. *Cell Commun Adhes* (2008).

32. Camelliti, P., Devlin, G. P., Matthews, K. G., Kohl, P. & Green, C. R. Spatially and temporally distinct expression of fibroblast connexins after sheep ventricular infarction. *Cardiovasc. Res.* (2004).

33. Rook, M. B., Jongsma, H. J. & de Jonge, B. Single channel currents of homo- and heterologous gap junctions between cardiac fibroblasts and myocytes. *Pflugers Arch.* (1989).

34. Dupont, E. Altered Connexin Expression in Human Congestive Heart Failure. *Journal of Molecular and Cellular Cardiology* (2001).

35. Yamada, K. A., Rogers, J. G., Sundset, R., Steinberg, T. H. & Saffitz, J. E. Up-regulation of connexin45 in heart failure. *J. Cardiovasc. Electrophysiol.* (2003).

36. Zhang, Y., Kanter, E. M. & Yamada, K. A. Remodeling of cardiac fibroblasts following myocardial infarction results in increased gap junction intercellular communication. *Cardiovascular Pathology* (2010).

37. Desplantez, T., Halliday, D., Dupont, E. & Weingart, R. Cardiac connexins Cx43 and Cx45: formation of diverse gap junction channels with diverse electrical properties. *Pflugers Arch.* (2004).

38. Peracchia, C. Chemical gating of gap junction channels. *Biochimica et Biophysica Acta (BBA) - Biomembranes* (2004).

39. Harris, A. & Locke, D. *Connexins* (Humana Pr Inc, 2009).

40. Moreno, A. P. Biophysical properties of homomeric and heteromultimeric channels formed by cardiac connexins. *Cardiovasc. Res.* (2004).

41. Moreno, A. P., Fishman, G. I. & Spray, D. C. Phosphorylation shifts unitary conductance and modifies voltage dependent kinetics of human connexin43 gap junction channels. *BPJ* (1992).

42. Van Veen, T. A., van Rijen, H. V. & Jongsma, H. J. Electrical conductance of mouse connexin45 gap junction channels is modulated by phosphorylation. *Cardiovasc. Res.* (2000).

43. Weber, P. A., Chang, H.-C., Spaeth, K. E., Nitsche, J. M. & Nicholson, B. J. The Permeability of Gap Junction Channels to Probes of Different Size Is Dependent on Connexin Composition and Permeant-Pore Affinities. *Biophysical Journal* (2004).

44. Hanani, M. Lucifer yellow - an angel rather than the devil. *Journal of Cellular and Molecular Medicine* (2012).

45. Abbaci, M., Barberi-Heyob, M., Blondel, W., Guillemin, F. & Didelon, J. Advantages and limitations of commonly used methods to assay the molecular permeability of gap junctional intercellular communication. *Biotech.* (2008).

46. Vogel, R. & Weingart, R. Mathematical model of vertebrate gap junctions derived from electrical measurements on homotypic and heterotypic channels. *The Journal of Physiology* (1998).

47. Chen-Izu, Y, Moreno, A. P. & Spangler, R. A. Opposing gates model for voltage gating of gap junction channels. *Am. J. Physiol., Cell Physiol.* (2001).

48. Paulauskas, N., Pranevicius, M., Pranevicius, H. & Bukauskas, F. F. A Stochastic Four-State Model of Contingent Gating of Gap Junction Channels Containing Two "Fast" Gates Sensitive to Transjunctional Voltage. *Biophysical Journal* (2009).

49. Paulauskas, N., Pranevicius, H., Mockus, J. & Bukauskas, F. F. Stochastic 16-State Model of Voltage Gating of Gap-Junction Channels Enclosing Fast and Slow Gates. *Biophysical Journal* (2012).

50. Lin, X., Gemel, J., Beyer, E. C. & Veenstra, R. D. Dynamic model for ventricular junctional conductance during the cardiac action potential. *Am. J. Physiol. Heart Circ. Physiol.* (2005).

51. Shibukawa, Y., Chilton, E. L., MacCannell, K. A., Clark, R. B. & Giles, W. R. K+ Currents Activated by Depolarization in Cardiac Fibroblasts. *Biophysical Journal* (2005).

52. Chilton, L. K+ currents regulate the resting membrane potential, proliferation, and contractile responses in ventricular fibroblasts and myofibroblasts. *AJP: Heart and Circulatory Physiology* (2005).

53. Nayak, A. R., Shajahan, T. K., Panfilov, A. V. & Pandit, R. Spiral-Wave Dynamics in a Mathematical Model of Human Ventricular Tissue with Myocytes and Fibroblasts. *PLoS ONE* (2013).

54. Sachse, F. B., Moreno, A. P. & Abildskov, J. A. Electrophysiological Modeling of Fibroblasts and their Interaction with Myocytes. *Ann Biomed Eng* (2007).

55. Jacquemet, V. & Henriquez, C. S. Modelling cardiac fibroblasts: interactions with myocytes and their impact on impulse propagation. *Europace* (2007).

56. MacCannell, K. A. *et al.* A Mathematical Model of Electrotonic Interactions between Ventricular Myocytes and Fibroblasts. *Biophysical Journal* (2007).

57. Burstein, B, Libby, E, Calderone, A & Nattel, S. Differential Behaviors of Atrial Versus Ventricular Fibroblasts: A Potential Role for Platelet-Derived Growth Factor in Atrial-Ventricular Remodeling Differences. *Circulation* (2008).

58. Chatelier, A. *et al.* A distinct de novo expression of Nav1.5 sodium channels in human atrial fibroblasts differentiated into myofibroblasts. *The Journal of Physiology* (2012).

59. Koivumäki, J. T. *et al.* Na(+) current expression in human atrial myofibroblasts: identity and functional roles. *Front Physiol* (2014).

60. Maleckar, M. M., Greenstein, J. L., Giles, W. R. & Trayanova, N. A. Electrotonic Coupling between Human Atrial Myocytes and Fibroblasts Alters Myocyte Excitability and Repolarization. *Biophysical Journal* (2009).

61. Wilson, J. R., Clark, R. B., Banderali, U. & Giles, W. R. Measurement of the membrane potential in small cells using patch clamp methods. *channels* (2011).

62. Xie, Y. *et al.* Effects of fibroblast-myocyte coupling on cardiac conduction and vulnerability to reentry: A computational study. *Heart Rhythm* (2009).

63. Kohl, P. & Camelliti, P. Fibroblast–myocyte connections in the heart. *HRTHM* (2012).

64. Ten Tusscher, K. H. W. J. A model for human ventricular tissue. *AJP: Heart and Circulatory Physiology* (2003).

65. Xie, Y, Garfinkel, A, Weiss, J. N. & Qu, Z. Cardiac alternans induced by fibroblast-myocyte coupling: mechanistic insights from computational models. *AJP: Heart and Circulatory Physiology* (2009).

66. Luo, C. H. & Rudy, Y. A model of the ventricular cardiac action potential. Depolarization, repolarization, and their interaction. *Circ. Res.* (1991).

67. Miragoli, M., Gaudesius, G. & Rohr, S. Electrotonic modulation of cardiac impulse conduction by myofibroblasts. *Circ. Res.* (2006).

68. Zlochiver, S. *et al.* Electrotonic Myofibroblast-to-Myocyte Coupling Increases Propensity to Reentrant Arrhythmias in Two-Dimensional Cardiac Monolayers. *Biophysical Journal* (2008).

69. Miragoli, M., Salvarani, N. & Rohr, S. Myofibroblasts induce ectopic activity in cardiac tissue. *Circ. Res.* (2007).

70. Greisas, A. & Zlochiver, S. Modulation of spiral-wave dynamics and spontaneous activity in a fibroblast/myocyte heterocellular tissue–a computational study. *IEEE Trans Biomed Eng* (2012).

71. Gomez, J. F., Cardona, K., Romero, L., Ferrero, J. M. & Trenor, B. Electrophysiological and Structural Remodeling in Heart Failure Modulate Arrhythmogenesis. 1D Simulation Study. *PLoS ONE* (2014).

72. Gomez, J. F., Cardona, K., Martinez, L., Saiz, J. & Trenor, B. Electrophysiological and Structural Remodeling in Heart Failure Modulate Arrhythmogenesis. 2D Simulation Study. *PLoS ONE* (2014).

73. Grandi, E., Pasqualini, F. S. & Bers, D. M. A novel computational model of the human ventricular action potential and Ca transient. *Journal of Molecular and Cellular Cardiology* (2010).

74. O'Hara, T., Virág, L., Varró, A. & Rudy, Y. Simulation of the Undiseased Human Cardiac Ventricular Action Potential: Model Formulation and Experimental Validation. *PLoS Comput Biol* (2011).

75. McDowell, K. S., Arevalo, H. J., Maleckar, M. M. & Trayanova, N. A. Susceptibility to arrhythmia in the infarcted heart depends on myofibroblast density. *Biophysical Journal* (2011).

76. Mahajan, A. *et al.* A rabbit ventricular action potential model replicating cardiac dynamics at rapid heart rates. *Biophysical Journal* (2008).

77. Nguyen, T. P., Xie, Y, Garfinkel, A, Qu, Z & Weiss, J. N. Arrhythmogenic consequences of myofibroblast-myocyte coupling. *Cardiovasc. Res.* (2012).

78. Ashihara, T *et al.* The Role of Fibroblasts in Complex Fractionated Electrograms During Persistent/Permanent Atrial Fibrillation: Implications for Electrogram-Based Catheter Ablation. *Circ. Res.* (2012).

79. Courtemanche, M, Ramirez, R. J. & Nattel, S. Ionic mechanisms underlying human atrial action potential properties: insights from a mathematical model. *Am. J. Physiol.* (1998).

80. Campos, F. O. *et al.* Electroanatomical Characterization of Atrial Microfibrosis in a Histologically Detailed Computer Model. *IEEE Trans. Biomed. Eng.* (2013).

81. McDowell, K. S. *et al.* Mechanistic Inquiry into the Role of Tissue Remodeling in Fibrotic Lesionsin Human Atrial Fibrillation. *BPJ* (2013).

CHAPTER 2

ILLUMINATING MYOCYTE-FIBROBLAST HOMOTYPIC AND HETEROTYPIC GAP JUNCTION DYNAMICS USING THE DYNAMIC-CLAMP TECHNIQUE*

2.1 Abstract

Fibroblasts play a significant role in the development of electrical and mechanical dysfunction of the heart; however the underlying mechanisms are only partially understood. One widely studied mechanism suggests that fibroblasts produce excess extracellular matrix, resulting in collagenous septa that slow propagation, cause zig-zag conduction paths, and decouple cardiomyocytes, resulting in a substrate for cardiac arrhythmia. An emerging hypothesis suggests that fibroblasts promote arrhythmogenesis through direct electrical interactions with cardiomyocytes via gap junction (gap junction) channels. In the heart, three major connexin (Cx) isoforms, Cx40, Cx43 and Cx45 form gap junction channels in cell-type-specific combinations. Because each Cx is characterized by a unique time- and transjunctional voltage-dependent profile, this study investigated whether the electrophysiological contributions of fibroblasts would vary with the specific composition of the myocyte-fibroblast (myocyte-fibroblast) gap junction channel. Due to the challenges of systematically modifying Cxs *in vitro*, native cardiomyocytes were coupled with *in silico* fibroblast and gap junction channel electrophysiological models using the dynamic-clamp technique. The results demonstrated that there is a reduction in the early peak of the junctional current during the upstroke of the action potential due to gap junction channel gating. However, effects on the cardiomyocyte action potential morphology were similar regardless of the specific type of gap junction

*Reproduced from Brown TR, Krogh-Madsen T, and D.J. Christini. Illuminating myocyte-fibroblast homotypic and heterotypic gap junction dynamics using the dynamic-clamp technique. Biophysical Journal. in press.

channel (homotypic Cx43, Cx45, and heterotypic Cx43/Cx45 and Cx45/Cx43). Furthermore, a cell-specific model of our dynamic-clamp experiments was used to investigate changes in the underlying membrane currents during myocyte-fibroblast coupling. These findings shed more light on the complex electrophysiological interplay between cardiac fibroblasts and myocytes.

2.2 Introduction

The adult heart is composed of cardiomyocytes and a diverse population of non-myocyte cells including: fibroblasts, endothelial cells, pericytes, immune cells, and vascular smooth muscle cells. The most abundant non-myocyte cells, cardiac fibroblasts, form an intermingled network with cardiomyocytes and account for ~27% of cells in the mouse heart to as much as 70% of cells in the rat heart [1, 2]. Fibroblasts play a significant role in the development of electrical and mechanical dysfunction of the diseased heart. Cardiac diseases such as myocardial infarction, pressure/volume overload, and heart failure result in fibroblast accumulation and differentiation into the activated myofibroblast state. Myofibroblasts secrete and remodel extracellular matrix, causing the formation of collagenous septa which slow propagation, cause zig-zag conduction paths, and decouple cardiomyocytes, resulting in a substrate for cardiac arrhythmia [3].

Recent evidence suggests that fibroblasts may also promote arrhythmogenesis through direct electrical interactions with cardiomyocytes. Several studies have demonstrated that fibroblasts form gap junction (gap junction) channels with cardiomyocytes *in vitro* [4, 5] and *ex vivo* in the SA node [6]. However, contrary to previous studies, Baum et al., found no indication of functional myocyte-fibroblast (myocyte-fibroblast) coupling [7]. This controversy regarding the role of myocyte-fibroblast coupling *in vivo*, has prompted the development of novel optogenetic strategies to investigate myocyte-fibroblast interactions *in vivo* [8, 9]. Because of the limitations of existing experimental

models, combined computational modeling and *in vitro* experiments have proved valuable in illuminating the potential contributions of myocyte-fibroblast interactions in the heart. Modeling studies have suggested that fibroblasts may modify cardiac electrophysiology by reducing action potential (action potential) duration, modifying conduction velocity, and inducing spontaneous electrical activity when coupled to cardiomyocytes via gap junction channels [10–12]. A gap junction channel is composed of two hemichannels docked head-to-head spanning two bilayer membranes. Each hemichannel is composed of six protein subunits, termed connexins (Cx) arranged in a hexagonal pattern around a central pore [13]. In general, gap junction channels are described as homotypic if both hemichannels are composed of the same Cx isoform and heterotypic if the Cxs of the two hemichannels differ. In the heart, three major Cx isoforms: Cx40, Cx43 and Cx45 form gap junction channels in cell-type-specific combinations.

Since each gap junction channel exhibits unique static (single-channel conductance) and dynamic (voltage-sensitive gating) properties, it has been postulated that Cx type and distribution may play a functional role in cardiac conduction [14]. For example, the Cxs in the heart have differing single-channel conductance and regional and cell specific differences in Cx distribution. The single-channel conductance of Cx43 is ~90 pS and much larger than that of Cx45, which is only ~35 pS [15]. Cx43 is highly expressed in ventricular cardiomyocytes and are co-expressed with small amounts of Cx45 in the normal heart, while atrial cardiomyocytes express Cx40 in addition to equal amounts of Cx43 and slightly higher amounts of Cx45 than ventricular cardiomyocytes [16]. Moreover, changes in Cx expression are also observed during cardiac disease. For example, Cx43 is down-regulated and Cx45 is up-regulated during heart failure [17, 18]. Cardiac fibroblasts also express Cx43 and Cx45, but with relatively higher levels of Cx45 [19, 20], suggesting that a myocyte-fibroblast gap junction channel in the ventricle may be predominantly heterotypic Cx43/Cx45 [21], and may also form homotypic Cx43 and

Cx45 channels. Elucidating the functional effects of such homotypic and heterotypic gap junction channels on myocyte-fibroblast interactions is the focus of this study. Recent work by McSpadden *et al.* investigated the effect of Cx type on myocyte and non-myocyte coupling and showed that non-myocyte cells expressing Cx45 were more weakly coupled to cardiomyocytes and had more moderate effects on cardiomyocyte resting potential and conduction velocity compared to non-myocytes cells expressing Cx43 [22]. However, due to the limitation of the experimental setup, they were not able to distinguish between effects mediated by heterotypic Cx43/Cx45 and Cx45 gap junction channels. Interestingly, Desplantez *et al.* found that increasing Cx45:Cx43 ratio in cell pairs resulted in a reduction of electrical coupling and cell-to-cell dye transfer [23]. These studies highlight how Cx type and distribution can influence cell-to-cell interactions.

This chapter expands upon these studies and earlier modeling work [24] by utilizing the dynamic-clamp technique to explore the effects of homotypic and heterotypic gap junction channels on myocyte-fibroblast interactions in the context of a real cell. Dynamic clamp is a powerful tool used in cardiac electrophysiology, which allows for real-time feedback between computational models and *in vitro* patch-clamped cells [25]. This approach was used to couple an *in vitro* patch-clamped guinea pig ventricular cardiomyocyte to a cardiac fibroblast electrophysiological model using gap junction channel models representing distinct Cx types.

2.3 Methods

Guinea pig ventricular myocyte isolation

Left ventricular myocytes were enzymatically isolated from the adult guinea pig heart via perfusion on a Langendorff apparatus, as described previously [26]. All procedures

were performed in accordance with the Weill Cornell IACUC protocol 0701-571A. In brief, adult Hartley guinea pigs (n = 4) were anesthetized using intraperitoneal injection of 120 mg/kg of sodium pentobarbital. The heart was excised, cannulated and perfused first with Common Tyrode's buffer (in mM): 130 NaCl, 5.4 KCl, 3.5 $MgCl_2$, 5 HEPES, 10 Dextrose, 2 $CaCl_2$, pH 7.2 with NaOH, (osmolality 288 mmol/kg) to facilitate the removal of blood, followed by calcium-free Common Tyrode's buffer to stop contractions, and finally with Common Tyrode's buffer solution containing Collagenase Type II (Worthington, Lakewood, NJ), Protease Type XIV (Sigma-Aldrich Corp., St. Louis, MO), and 0.05 mM $CaCl_2$. The left ventricle was dissected, minced, and further digested in Common Tyrode's buffer containing Collagenase Type II. The final suspension of cells contained a population of single cardiomyocytes. Cells were stored in Dulbecco's Modified Eagle Medium with 5% fetal bovine serum or in Common Tyrode's buffer with 0.5% bovine serum albumin and 0.75 mM $CaCl_2$. Only rod shaped cells with striations were selected for electrophysiology studies.

Electrophysiological recordings

Whole-cell Amphotericin B (Sigma-Aldrich Corp., St. Louis, MO) perforated patch-clamp recordings were obtained at 35-37°C using a model 2400 patch-clamp amplifier (A-M systems, Sequim, WA, USA). Patch pipettes were pulled from 1.5-mm OD, 0.86-mm ID borosilicate glass capillary tubes (Sutter Instrument, Novato, CA) to a resistance of 1.6-2 MΩ and backfilled with pipette solution. Pipette solution contained (in mM): 113 KCl, 10 NaCl, 5.5 Dextrose, 0.5 $MgCl_2$, 11 KOH, 10 HEPES, 10 μM $CaCl_2$, pH 7.1 with KOH (osmolality 289 ± 0.6 mmol/kg). Extracellular solution contained (in mM): 137 NaCl, 5.4 KCl, 1 MgSO4, 10 HEPES, 10 Dextrose, 2 $CaCl_2$, pH 7.35 with NaOH (osmolality 304 ± 0.6 mmol/kg). Recordings were corrected for a liquid junction potential of −3 mV.

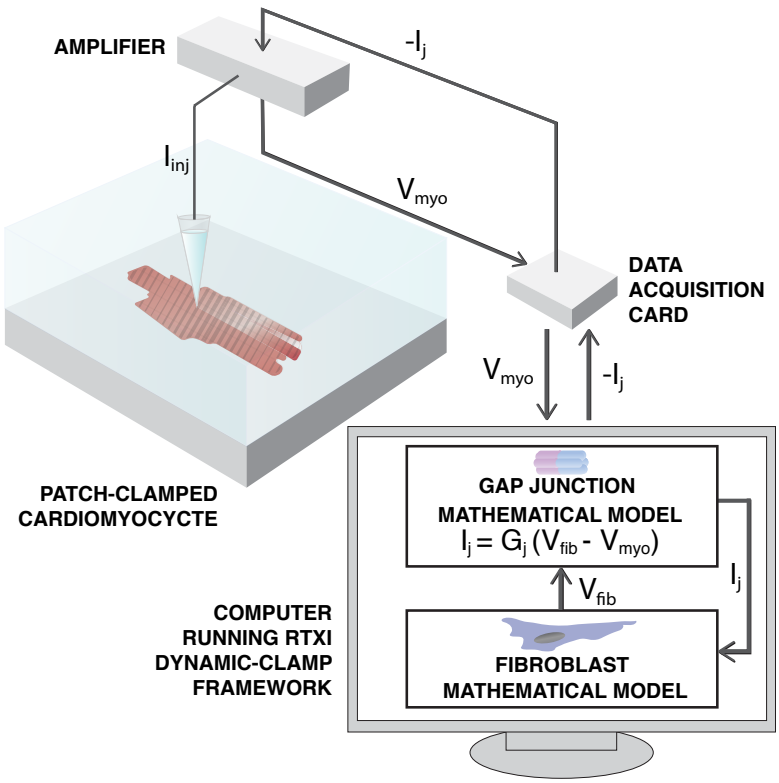

Figure 2.1 | *Schematic of dynamic-clamp technique*.
The dynamic-clamp technique allows for real-time feedback between computational models and *in vitro* patch-clamped cardiomyocytes. In this approach, an *in vitro* cardiomyocyte cell is patch-clamped and its membrane potential is measured and fed into the computer's data acquisition system, simultaneously a cardiac fibroblast model is simulated in real-time. Next, a junctional current, I_j, is calculated as a function of the gap junctional conductance, G_j, and the difference between the fibroblast model voltage, V_{fib}, and cardiomyocyte voltage, V_{myo}. Finally, the junction current is injected back into the fibroblast model and the *in vitro* cardiomyocyte via the patch-clamp amplifier. Resulting in a circuit as if the cardiomyocyte was directly coupled to the fibroblast model.

Dynamic-clamp experiments

Figure 2.1 shows a schematic of the dynamic-clamp feedback circuit. Guinea pig ventricular cardiomyocytes were patch-clamped and used the dynamic-clamp technique to couple them to the MacCannell fibroblast electrophysiological model [27] via gap junction channel models developed to represent the gating and kinetic properties of Cx43, Cx45, and Cx43/Cx45. Dynamic-clamp protocols were implemented using the Real-

Time eXperiment Interface (RTXI; www.rtxi.org) framework developed in the laboratory [28, 29]. Prior to the start of dynamic-clamp recordings, the patch-clamped cardiomyocyte was paced at 2 Hz in current-clamp mode using 1.5 times the threshold stimulus pulse for 1 ms duration until it reached a stable recording. The bridge balance was used to compensate for 70–100% of the voltage drop across the access resistance which ranged from 5.8–16.6 MΩ.

The capacitance of the fibroblast model was fixed at 6.3 pF as reported in the MacCannell model [27], while the capacitance of the *in vitro* guinea pig cardiomyocyte varied from cell-to-cell. In order to ensure that the relative size of the *in vitro* cell and the fibroblast electrophysiological model were similar across cells, the capacitance of the cardiomyocyte was determined using a real-time estimate measured in voltage-clamp mode. A scaling factor ($k = C_{\mathrm{m}}/153.4$) was then used to scale the junctional current injected into the cardiomyocyte such that the effective size of the cell is equivalent to the dynamic-clamp simulations described below. The dynamic-clamp protocol consists of 40 uncoupled beats with dynamic clamp off, followed by 40 coupled beats with dynamic clamp on (i.e., coupling to the fibroblast electrophysiological model via a gap junction channel model). This protocol was then repeated for each of the gap junction channel models.

Dynamic-Clamp simulations

In order to provide mechanistic insight into which parameters play a key role in modifying action potential morphology during myocyte-fibroblast coupling, simulations of the dynamic-clamp experiments were performed. The published Livshitz and Rudy guinea pig ventricular myocyte model (LRd2009) [30] differs significantly in action potential morphology and action potential duration compared to the control experimental data and therefore has a limited ability to predict results from the dynamic-clamp experiments. Thus, a cell-specific model was generated using a genetic algorithm optimization proce-

dure similar to that of Groenendaal *et al.* [31] to scale (i.e., 0.01–2.9 times the published values) maximal conductance parameters of the LRd2009 model to fit experimental data. The optimization was focused on the maximal conductance parameters based on the assumption that most cell-to-cell variability is due to different expression levels of ion channels, represented by maximal conductance parameters in the model, while model kinetics are more conserved across healthy cells. Current-clamp recordings were used, which consisted of a train of 40 action potentials during pacing at a cycle length of 500 ms as the target cell behavior. The sum-of-squared-errors (SSE) between the experimental data and the model voltage was used as the objective function used as a quantitative measure of the difference between the model behavior and the cell behavior during the optimization procedure:

$$\mathrm{SSE} = \sum_{\mathrm{i}=1}^{\mathrm{N}} (V_{\mathrm{data}} - V_{\mathrm{model}})^2, \tag{2.1}$$

where $\mathrm{V_{data}}$ is the experimentally recorded myocyte voltage, $\mathrm{V_{model}}$ is the model output voltage, and N is the total number of data points sampled. The end result of the optimization is a set of parameters for the calibrated cell-specific model.

To simulate the dynamic-clamp experiments the *in vitro* cardiomyocytes in Figure 2.1 is replaced with a calibrated cell-specific model and coupled it to the fibroblast electrophysiology model via a gap junction channel model (see Figure 2.2 *C*) as described previously [24]. Briefly, the membrane voltage of the myocyte ($\mathrm{V_{myo}}$) and the fibroblast ($\mathrm{V_{fib}}$) are derived from Eqn. Equation 2.2 and Equation 2.3, respectively. $\mathrm{C_{myo}}$ and $\mathrm{C_{fib}}$ are the membrane capacitance and $\mathrm{I_{myo}}$ and $\mathrm{I_{fib}}$ are the total ionic current flowing through the ion channels, pumps, and exchangers. $\mathrm{I_{stim}}$ is the stimulus current. N is the number of fibroblast models coupled to a single cardiomyocyte model.

$$\frac{\mathrm{d}V_{\mathrm{myo}}}{\mathrm{d}t} = -\frac{1}{C_{\mathrm{myo}}} \left[I_{\mathrm{myo}}(V_{\mathrm{myo}}, t) + I_{\mathrm{stim}} + \sum_{\mathrm{i}=1}^{\mathrm{N}} I_{\mathrm{j}} \right] \tag{2.2}$$

$$\frac{dV_{fib}}{dt} = -\frac{1}{C_{fib}}\left(I_{fib}(V_{fib}, t) + I_j\right) \tag{2.3}$$

$$I_j = G_j(V_{fib} - V_{myo}) \tag{2.4}$$

$$\begin{aligned} G_j = N_{chans}(&G_{HH} \cdot N_{HH} + G_{LH} \cdot N_{LH} \\ &G_{HL} \cdot N_{HL} + G_{LL} \cdot N_{LL}) \end{aligned} \tag{2.5}$$

The junctional current, I_j, is calculated using Eq. Equation 2.4, where the junctional conductance, G_j, is dependent on the gap junction model used ("static" or "dynamic"). In the static model, G_j is a constant conductance. In the dynamic model, G_j is based on the Vogel and Weingart model [32], where the conductance is dependent on the fraction of gap junction channels in a given state and their corresponding conductance and the number of gap junction channels, N_{chans}, as shown in Eq. Equation 2.5 and detailed in Figure 2.2.

2.4 Results

Development of homotypic and heterotypic gap junction channel models.

Mathematical models of homotypic Cx43, homotypic Cx45, and heterotypic Cx43/Cx45 gap junction channels were developed as these are the most relevant mediators of myocyte-fibroblast (myocyte-fibroblast) coupling in the ventricles. Figure 2.2 illustrates the basic gating properties of these gap junction channel models. In general, the gap junction channel conductance (G_j) is both time and transjunctional voltage (V_j) dependent. The top graphs in Figure 2.2 *B* show the junctional current recorded from cell pairs in response to V_j steps of ±10, ±40, ±70, ±100, and ±130 mV and demonstrates that the junctional current inactivates to a steady state value in response to an applied

V_j. The rate of inactivation is faster for large positive or negative V_j steps. The bottom graphs in Figure 2.2 *B* show the normalized (i.e., to V_j = 0 mV) instantaneous (open circles) and steady-state (closed circles) G_j vs. V_j relationship. The instantaneous G_j vs. V_j relationship is approximately linear for small V_j values but becomes non-linear with larger V_j values. Moreover, the V_j-dependence is symmetric for homotypic channels but asymmetric for heterotypic channels [33].

The four state mathematical model of vertebrate gap junction channels by Vogel and Weingart [32] was used as the basis model because it accounts for the voltage-sensitive gating and inactivation kinetics of gap junction channels. This model was also computationally efficient, which is important for the dynamic-clamp experiments, whose accuracy is dependent on low latency between voltage measures from the patch-clamped cardiomyocytes and calculations of current injections from the computational models. A schematic of the Vogel and Weingart model is shown in Figure 2.2 *A*. It consists of two hemichannel models connected in series with each hemichannel containing a voltage-sensitive gate that transitions between a high (H) and low (L) conductance state. The gates function independently, leading to four states of the gap junction channel model: HH, HL, LH, and LL. State HH represents the main open state, γ_{open}, while states HL and LH represent the sub-conductance or residual state, γ_{res}, of the channel [34]. Least-squares curve fitting and parameter tuning was used to fit the model to the experimental data from Desplantez *et al.* [33] (Figure 2.2 *B*), with initial parameter constraints based on previous electrophysiology and computational modeling studies [35–38].

Figure 2.2 *C* shows simulations of the developed Cx43, Cx45, and Cx43/Cx45 gap junction channel models. Their corresponding parameters are listed in Table A.1. The top graphs in Figure 2.2 *C* shows junctional current responses to V_j steps from −130 to 130 mV in 20-mV increments and the bottom graphs demonstrates the G_j vs. V_j of the gap junction channel models.

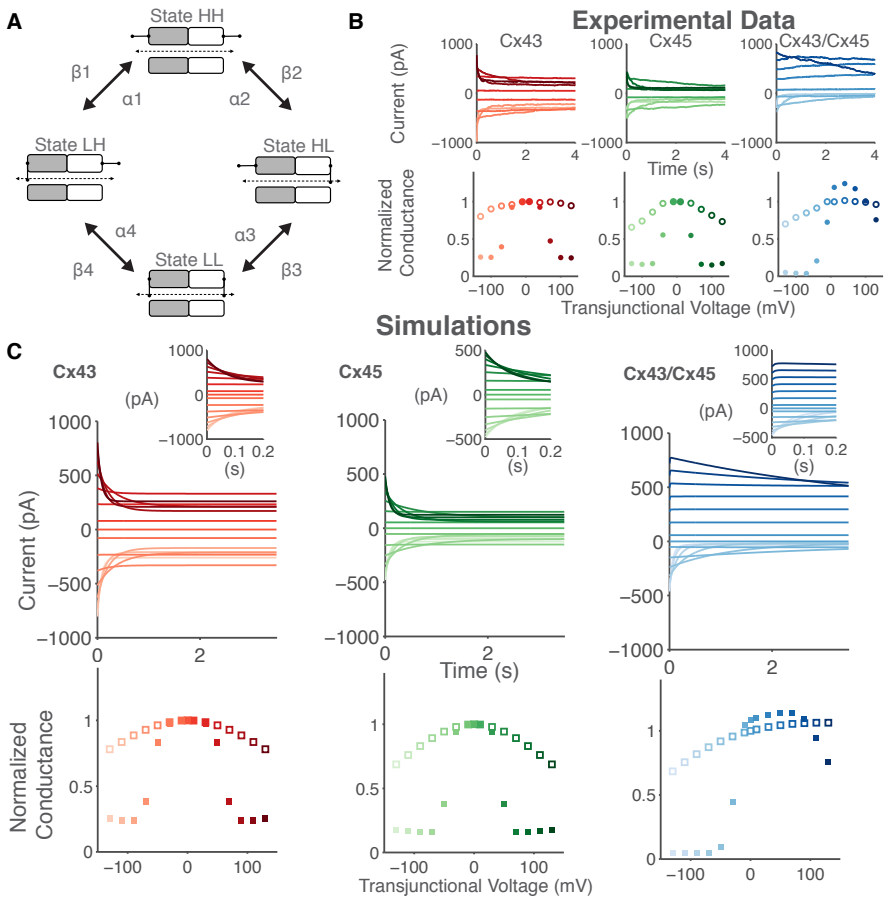

Figure 2.2 | *Mathematical modeling of homotypic Cx43, Cx45, and heterotypic Cx43/Cx45 gap junction using the Vogel model.*
(*A*) The schematic of the gap junction channel model consists of two hemichannel connected in series with each hemichannel containing a voltage sensitive gate, each hemichannel transitions between a high (H) and low (L) non-zero conductance state gated by the transjunctional voltage (V_j). The gates are functionally independent, leading to four conformational states: HH, HL, LH, LL. (*B*) Dual whole-cell patch clamp experimental recordings of transfected human HeLa cells pairs expressing rat Cx43 (*left-column*), mouse Cx45(*middle-column*), and their heterotypic Cx43/Cx45 combination (*right-column*) reproduced from Desplantez *et al.* [33] with permission. (*top*) Junctional current recorded at V_j = ±10, ±40, ±70, ±100, and ±130 mV. (*bottom*) Mean normalized instantaneous (○) and steady-state (●) conductance as a function of V_j. Shading of currents corresponds to shading of conductance, with darker shades representing increasingly positive V_j values. (*C*) Parameters of the Vogel and Weingart model were modified to reproduce key features of the experimental data in (*B*). (*top*) Simulations of the junctional current of 100 Cx43 channels (*left*), 250 Cx45 channels (*middle*), 100 Cx43/Cx45 channels (*middle*) at V_j steps from −130 to 130 mV in 20-mV increments. (*Insets*) Current responses to V_j for shorter time scales. (*bottom*) Normalized instantaneous (□) and steady-state (■) conductance as a function of V_j.

The Cx specific models in Figure 2.2 *C* reproduces key features of the experimental data. For example, Cx45 is more voltage sensitive than Cx43. This behavior is demonstrated by the steeper decline in the junctional current (compare Figure 2.2 *C*, *top-left* and *top-center*) and the smaller half-maximal inactivation of Cx45 of 46 mV compared to that of Cx43, which is 65 mV according to the G_j-V_j plot (compare Figure 2.2 *C*, *bottom-left* and *bottom-center*). The main open state γ_{open} can be calculated as the sum of conductors is series using the equation: $\gamma_{open} = \gamma_{H1} \cdot \gamma_{H2}/(\gamma_{H1} + \gamma_{H2})$, which results in a value of 79.3 pS for the Cx43 model, 35.8 pS for the Cx45 model, and 56.7 pS for the Cx43/Cx45 model, which are within the range of experimentally measured values of 60 – 118 pS, 26 – 32 pS [39], and 55 – 65 pS [36], respectively. The Cx43/Cx45 model also reproduces the asymmetric voltage sensitivity, with enhanced voltage sensitivity at negative V_j. It is important to note that the Cx43/Cx45 model behavior is not simply a summation of the Cx43 and Cx45 hemichannel models. This is in line with evidence that the docking of heterotypic gap junction channels results in conformational changes in the component Cx43 hemichannel and Cx45 hemichannel [36].

Myocyte-fibroblast coupling using dynamic clamp.

The dynamic-clamp technique was used to investigate whether the unique time- and V_j-dependent profiles of Cx43, Cx45, and Cx43/Cx45 gap junction channels modifies myocyte-fibroblast coupling. A schematic of the dynamic-clamp experimental setup is presented in Figure 2.1. To facilitate direct comparisons between the effects of the different Cx types on action potential morphology and action potential duration, multiple coupling protocols were performed on a single *in vitro* cardiomyocyte (see Materials and Methods). Since the gap junction channel models vary in both single-channel conductance and V_j-dependent gating, the effects of V_j-dependent gating was distinguished by normalizing the resting channel conductance (i.e., at V_j = 0 mV) of the Cx specific models to the magnitude of the static model conductance.

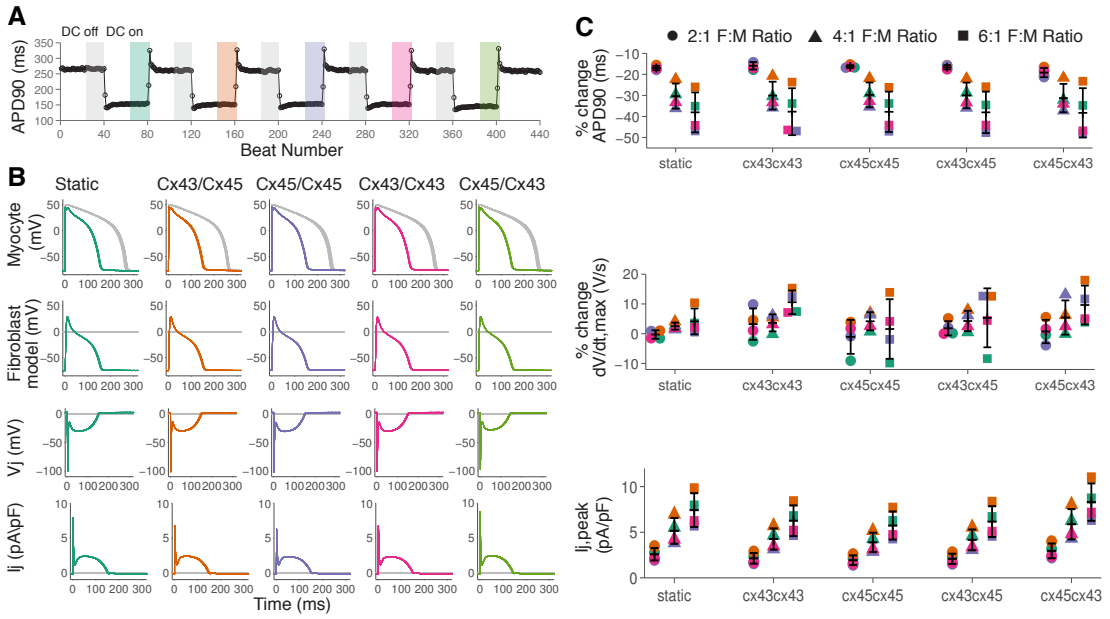

Figure 2.3 | *Dynamic-clamp recordings using in vitro ventricular cardiomyocytes.* (*A* and *B*) Example of dynamic-clamp (DC) recordings from a single cell coupled to 6 fibroblast models (high fibrosis) with 2 nS conductance, G_j. The protocol consists of 40 uncoupled beats with dynamic-clamp off, 40 coupled beats with dynamic-clamp on (i.e., coupling to the fibroblast model via 4 Cx models: Cx43, Cx45, Cx43/Cx45, Cx45/Cx43, and a constant conductance "static model". The G_j of the Cx model at V_j=0 mV was scaled to the static model conductance. (*A*) APD_{90} vs. beat number, shows a reduction in action potential duration when the cell is coupled to the fibroblast model (*color bars*). (*B*) Overlay of voltage traces of the last 20 beats in each 40 beat segment (*bars* in *A*), showing the effects of dynamic-clamp coupling on action potential (action potential) morphology. (*row 1*) Myocyte voltage, (*row 2*) fibroblast model voltage, (*row 3*) transjunctional voltage $V_j = (V_{fib} - V_{myo})$, (*row 4*) junctional current. Coupling via the scaled Cx models results in similar changes in action potential morphology compared to the static model. (*C*) Percent change in APD_{90}, dV/dt_{max}, and the maximum junctional current ($I_{j,peak}$) compared to the previous uncoupled segment (DC off) with ● 2:1, ▲ 4:1, and ■ 6:1 fibroblast to myocyte ratio. All 5 gap junction models showed similar trends: increased $I_{j,peak}$, no change dV/dt_{max}, and reduction in APD_{90} with increasing fibroblast to myocyte ratio. Error bars represent S.D.

Figure 2.3 shows results of coupling an *in vitro* guinea pig ventricular myocyte to the MacCannell fibroblast model via 4 different Cx specific gap junction channel models: Cx43, Cx45, Cx43/Cx45, Cx45/Cx43, and a static gap junction model, using the dynamic-clamp technique. The Cx45/Cx43 model is the reverse orientation of the Cx43/Cx45 gap junction channel model presented in Figure 2.2 *C* (see Table 2.1 for Cx

Table 2.1 | Orientation of gap junction channel models

Model	Myocyte Connexin	Fibroblast Connexin
Cx43	Cx43	Cx43
Cx45	Cx45	Cx45
Cx43/Cx45	Cx43	Cx45
Cx45/Cx43	Cx45	Cx43

orientation). Figure 2.3 *A* and *B* represents myocyte-fibroblast coupling during a high degree of fibrosis (fibroblast to myocyte ratio of 6:1). Figure 2.3 *A* shows the action potential duration vs. beat number during the course of the experiment. When the dynamic clamp was turned on, the fibroblast model was coupled to the *in vitro* cardiomyocyte via a gap junction channel model. This resulted in a reduction in the cardiomyocyte action potential duration. This is due to the fibroblast acting as a current sink during the action potential resulting in an early repolarization. The magnitude of the action potential duration reduction is not significantly dependent on the time- and V_j-dependent properties of the gap junction channel model. The degree of reduction was similar for Cx43, Cx45, and Cx43/Cx45. Reversing the orientation of the heterotypic Cx43/Cx45 model also had similar effects on the cardiomyocyte action potential duration during the myocyte-fibroblast coupling schemes tested. Figure 2.3 *B* is an overlay of the recorded *in vitro* cardiomyocyte voltage trace and the fibroblast model voltage trace in the regions of the protocol highlighted in Figure 2.3 *A*. The difference between the myocyte and fibroblast voltage trace (V_j) and the junctional current (I_j) is also presented. During the upstroke of the action potential there is a minimum in V_j to -100 mV, as the myocyte quickly depolarizes. At this V_j the gap junction channel model inactivates rapidly. However, throughout the remainder of the action potential the V_j remains in the range of ± 30 mV, where the gap junction channel model shows little inactivation (see Figure 2.2). The main effects of time- and V_j dependent gating of the G_j channel models can be seen in the changes in the junctional current, where coupling via Cx43, Cx45, and Cx43/Cx45 results in a reduction of the early peak of the junctional current compared to the static

model. Reversing the orientation of the Cx43/Cx45 model results in an increase in the peak of the junctional current, demonstrating the rectifying behavior of this heterotypic channel. The asymmetry of the G_j vs. V_j relationship (Figure 2.2 *C*) facilitates current flow from the Cx45 expressing cell to the Cx43 expressing cell but impedes flow in the opposite direction.

Dynamic-clamp experiments were performed on four additional ventricular cardiomyocytes from the guinea pig heart and determined the effects on APD_{90}, dV/dt_{max} and $I_{j,peak}$ (i.e., the early peak of the junctional current). In Figure 2.3 *C*, the fibroblast to myocyte ratio was varied to explore the effects of Cx type during three different degrees of cardiac fibrosis: low fibrosis (fibroblast to myocyte ratio of 2:1), medium fibrosis (fibroblast to myocyte ratio of 4:1), and high fibrosis (fibroblast to myocyte ratio of 6:1). The percent change is calculated relative to the immediately proceeding protocol step with dynamic clamp off. The percent change in action potential duration shows a trend of increasing action potential duration reduction with increasing levels of fibrosis, but little change in dV/dt_{max}. Similar trends were observed across all 5 gap junction channel models. $I_{j,peak}$ increases with higher degrees of fibrosis due to the larger current sink provided by the increased number of fibroblast models coupled to a single cardiomyocyte. While the differences in $I_{j,peak}$ between Cx types did not reach statistical significance, there is a trend of Cx45/Cx43 resulting in increased $I_{j,peak}$ compared to the static model, while the other Cx types resulted in a reduction in $I_{j,peak}$. These results indicate that the time- and V_j-dependent gating of gap junction channels only plays a role during the upstroke of the action potential, when V_j is the large, during myocyte-fibroblast coupling.

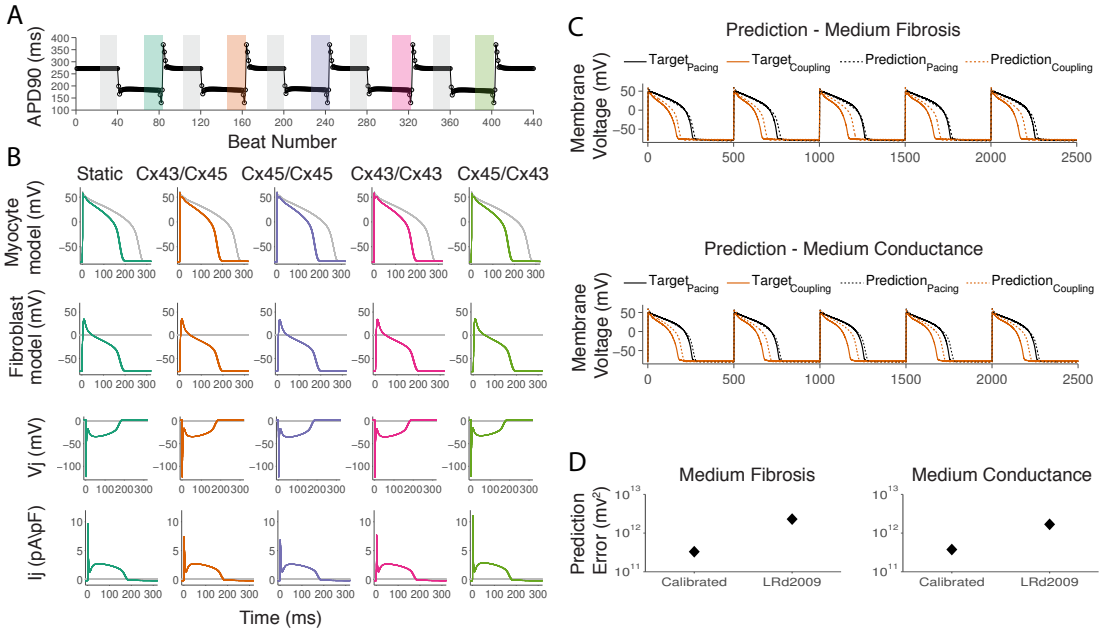

Figure 2.4 | *Simulations of dynamic-clamp recordings using a cell-specific model.* (*A* and *B*) Results of cell-specific model simulation using the same protocol as in Figure 2.3 *A* and *B*. (*A*) APD_{90} vs. beat number, shows a reduction in action potential duration when the cell-specific model is coupled to the fibroblast model (*color bars*). (*B*) Overlay of voltage traces of the last 20 beats in each 40 beat segment (*bars* in *A*), showing the effects of coupling on action potential morphology. (*row 1*) Myocyte model voltage, (*row 2*) fibroblast model voltage, (*row 3*) transjunctional voltage $V_j = (V_{fib} - V_{myo})$, (*row 4*) junctional current. (*C*) Prediction of the cell-specific model during coupling to 4 fibroblast models with 2 nS conductance (Medium fibrosis) (*top*) and 2 fibroblasts at 4 nS conductance (Medium Conductance) (*bottom*). Target pacing is the target experimental results during pacing of the *in vitro* guinea pig cardiomyocyte at a cycle length of 500 ms with dynamic clamp off. Target coupling is the target experimental results during dynamic-clamp coupling of the *in vitro* cell to the fibroblast models with the Cx43/Cx45 gap junction model. (*D*). The error was calculated as the sum-of-squared-error of the difference between the average of 20 beats during pacing minus the average of 20 beats during coupling during medium fibrosis and medium conductance.

Simulations of dynamic-clamp experiments using a cell-specific electrophysiological model.

To provide mechanistic insight into the underlying parameters that play a key role in myocyte-fibroblast coupling, simulations of the dynamic-clamp experiments using a cell-specific electrophysiological model was performed. To develop the cell-specific

model, a train of 40 action potentials was selected from the experimental data as the target cell behavior and used a genetic algorithm optimization technique to fit maximal conductance parameters to the experimental data using a strategy similar to Groenendaal *et al.* [31] (see Materials and Methods for details). Figure 2.4 *A* and *B* shows the results of using this strategy to develop an electrophysiological model for the cell in Figure 2.3 *B*. The simulation was generated by using the same protocol performed on the *in vitro* cardiomyocyte. The action potential duration of the calibrated model is a better match to the action potential duration of the experimental data compared to the published LRd2009 model whose action potential duration at a cycle length of 500 ms is ~130 ms [40] (Figure 2.4). In Figure 2.4 *B* an overlay of the uncoupled and the coupled voltage responses of the cell-specific model and fibroblast model mediated by gap junction channels of each Cx type is shown. The results are qualitatively similar to the results of the *in vitro* cell. To test for model improvement in predicting behavior during myocyte-fibroblast coupling, the predictions of the cell-specific model and the default LRd2009 model was compared to two new sets of experimental data. Figure 2.4 *D* shows that the calibrated model results in a reduced prediction error for both sets of data.

Previous studies have demonstrated that several ionic currents are modified during myocyte-fibroblast coupling [41]. In Figure 2.5, the changes in underlying currents in response to myocyte-fibroblast coupling is shown. The peak of the sodium current, I_{Na}, is only slightly reduced. The late phase of the L-type calcium current, I_{CaL}, is increased. The peak of the slow delayed rectifier current, I_{Ks}, was greatly reduced. Changes in I_{K1}, I_{NCX}, and I_{Kr} were also observed due to the change in the action potential waveform.

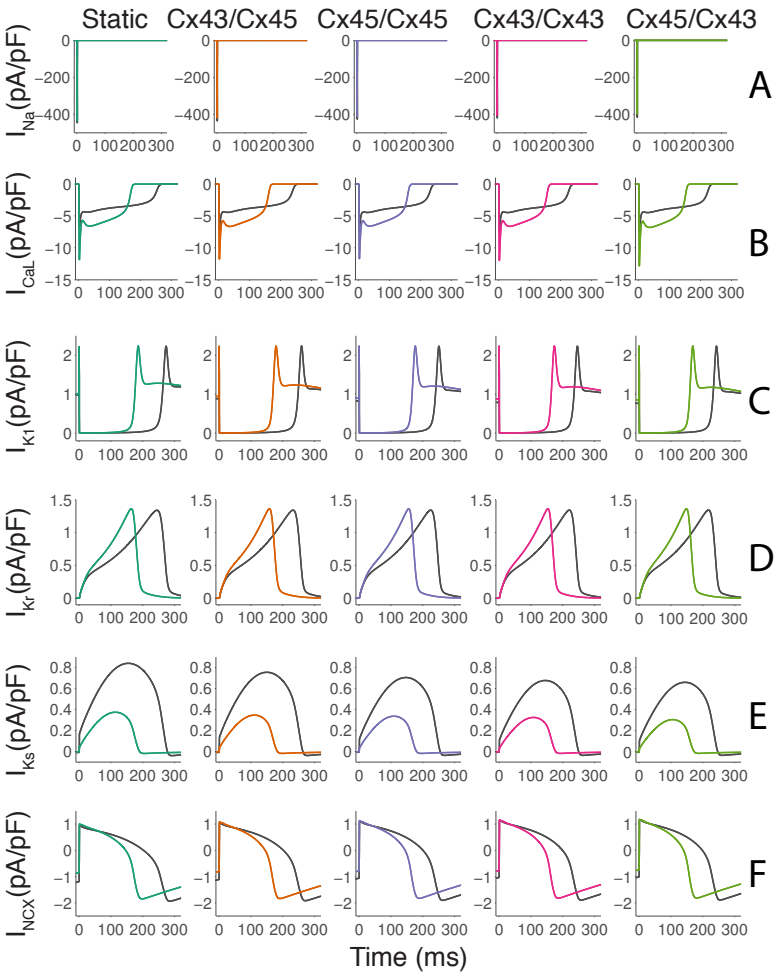

Figure 2.5 | *Plots of underlying current response during myocyte-fibroblast coupling using a cell-specific model.*
The cell-specific model from Figure 2.4 was coupled to 6 fibroblast models (high fibrosis) with 2 nS conductance and the underlying current responses were recorded. (*A*) The peak of the sodium current, I_{Na}, is slightly reduced. (*B*) The late phase of the L-type calcium current, I_{CaL}, is increased. (*C*) The inward rectifying potassium current I_{K1} was shortened along with the action potential waveform. (*D*) The rapid delayed rectifier potassium current, I_{Kr}, showed shortening along with the action potential waveform. (*E*) The peak of the slow delayed rectifier potassium current, I_{Ks}, is greatly reduced, and (*F*), the sodium calcium exchanger is also shortened due to changes in the action potential waveform.

2.5 Discussion

A combined computational modeling and dynamic-clamp experimental approach was used to investigate the role of homotypic and heterotypic gap junction channels in myocyte-fibroblast coupling. Mathematical models were developed for homotypic Cx43, homotypic Cx45, and heterotypic Cx43/Cx45 gap junction channels, the most likely mediators of myocyte-fibroblast coupling. Using the dynamic-clamp technique an *in vitro* guinea pig ventricular cardiomyocytes was coupled to fibroblast electrophysiological models via the developed Cx type specific models and compared their effects on the cardiomyocyte action potential morphology. Then a cell-specific model of the dynamic clamped cell was developed using a genetic-algorithm based optimization technique and used to analyze the underlying currents that were perturbed during myocyte-fibroblast coupling. The developed Cx type specific gap junction channel models reproduced the single-channel conductance properties and the time- and voltage-dependent gating of the Cx43, Cx45, and Cx43/Cx45 gap junction channels. Since previous studies have demonstrated that single channel conductance alone modifies myocyte-fibroblast coupling [27, 42], this study focused on investigating the contribution of the time- and voltage-dependent gating of gap junction channels on myocyte-fibroblast coupling. When the *in vitro* guinea pig ventricular myocyte was coupled to a fibroblast electrophysiological model using the static gap junction model, it resulted in a reduction in action potential duration as shown previously in a recent dynamic-clamp study [10]. Replacing the static gap junction model with one of the developed Cx specific gap junction models featuring time- and voltage-dependent gating resulted in similar changes in the action potential morphology. This suggests that gap junction channel gating does not play a significant role in myocyte-fibroblast coupling. This is likely due to the slow time constants of the inactivation kinetics of the gap junction

channel and due to the small transjunctional voltage between the myocyte and fibroblast during most of the action potential. These factors results in the gap junction channel operating predominantly on the instantaneous portion of the G_j vs. V_j curve (see Figure 2.2 *B* an *C*). The main differences between the static model and the Cx specific gap junction models was during the upstroke of the action potential, when the early peak of the junctional current was reduced in response to the large transjunctional voltage between the myocyte and fibroblast (seeFigure 2.3 *B* and *C*). Reduction in the early peak suggests a small reduction in the ability of the fibroblast to act as a current sink during the upstroke of the action potential. Using a cell-specific model of a dynamic-clamp experiments revealed that myocyte-fibroblast coupling results in significant changes in the underlying currents especially for I_{Ks} (see Figure 2.5 *E*). These results are similar to those found previously [27, 41].

2.6 Conclusions

The time- and V_j-dependent gating of gap junction channels results in inactivation of junctional conductance in response to large V_j steps. Despite each Cx type having unique features in their time- and V_j-dependent profiles, the kinetics of inactivation are very slow. During myocyte-fibroblast coupling the transjunctional voltage reaches a minimum at ~100 mV during the upstroke of the action potential. However, this large transjunctional voltage is short-lived; throughout the remainder of the action potential the transjunctional voltage is $< \pm 30$ mV. In this transjunctional voltage range the gap junction channel conductance is very linear for Cx43, Cx45 and Cx43/Cx45 gap junction channels. The large transjunctional voltage during the early upstroke of the action potential results in a reduction in the early peak of the junctional current compared to a static gap junction model. This reduction suggests that fibroblasts are acting as less of a current sink when myocyte-fibroblast coupling is mediated by a Cx specific model.

2.7 Limitations

The Cx models developed are largely based on a single set of experimental data expressed in transfected HeLa cells. Cx expressed in cardiomyocytes and fibroblasts may have different properties even though relative differences in the gating properties of the gap junction channels may be similar. Moreover, gap junction channels exhibit both electrical and chemical gating properties and allow for metabolic communication between neighboring cells [13]. The dynamic clamp and computational modeling studies focus on the effects of electrical gating properties of gap junction channels on myocyte-fibroblast coupling without taking into account the effects of chemical gating and metabolic communication of the gap junction channels. However, this strategy is also beneficial in that it enables the isolation of the contribution of the effects due to electrical interactions from other forms of myocyte-fibroblast interactions. Finally, since the effects of myocyte-fibroblast coupling on cardiomyocyte properties depends on the fibroblast electrophysiological properties [41] (which was not significantly explored in this study due to the lack of available experimental data), further understanding of the electrophysiological properties of fibroblasts could alter the contributions of gap junction gating during myocyte-fibroblast coupling.

BIBLIOGRAPHY

1. Nag, A. C. Study of Non-Muscle Cells of the Adult Mammalian Heart - a Fine-Structural Analysis and Distribution. *Cytobios* (1980).

2. Banerjee, I, Fuseler, J. W., Price, R. L., Borg, T. K. & Baudino, T. A. Determination of cell types and numbers during cardiac development in the neonatal and adult rat and mouse. *AJP: Heart and Circulatory Physiology* (2007).

3. De Jong, S., van Veen, T. A. B., van Rijen, H. V. M. & de Bakker, J. M. T. Fibrosis and cardiac arrhythmias. *J. Cardiovasc. Pharmacol.* (2011).

4. Baudino, T. A. *et al.* Cell Patterning: Interaction of Cardiac Myocytes and Fibroblasts in Three-Dimensional Culture. *MAM* (2008).

5. Vasquez, C *et al.* Enhanced Fibroblast-Myocyte Interactions in Response to Cardiac Injury. *Circ. Res.* (2010).

6. Camelliti, P., Green, C. R., LeGrice, I. & Kohl, P. Fibroblast network in rabbit sinoatrial node: structural and functional identification of homogeneous and heterogeneous cell coupling. *Circ. Res.* (2004).

7. Baum, J. R., Long, B, Cabo, C & Duffy, H. S. Myofibroblasts cause heterogeneous Cx43 reduction and are unlikely to be coupled to myocytes in the healing canine infarct. *AJP: Heart and Circulatory Physiology* (2012).

8. Kohl, P. & Gourdie, R. G. Fibroblast-myocyte electrotonic coupling: does it occur in native cardiac tissue? *Journal of Molecular and Cellular Cardiology* (2014).

9. Quinn, T. A., Camelliti, P., Siedlecka, U & Poggioli, T. Cell-specific expression of voltage-sensitive protein confirms cardiac myocyte to non-myocyte electrotonic coupling in healed murine infarct border tissue. *Circulation* (2014).

10. Nguyen, T. P., Xie, Y, Garfinkel, A, Qu, Z & Weiss, J. N. Arrhythmogenic consequences of myofibroblast-myocyte coupling. *Cardiovasc. Res.* (2012).

11. Miragoli, M., Gaudesius, G. & Rohr, S. Electrotonic modulation of cardiac impulse conduction by myofibroblasts. *Circ. Res.* (2006).

12. Miragoli, M., Salvarani, N. & Rohr, S. Myofibroblasts induce ectopic activity in cardiac tissue. *Circ. Res.* (2007).

13. Harris, A. & Locke, D. *Connexins* (Humana Pr Inc, 2009).

14. Giovannone, S, Remo, B. F. & Fishman, G. I. Channeling diversity: Gap junction expression in the heart. *HRTHM* (2012).

15. Zipes, D. P. & Jalife, J. *Cardiac Electrophysiology: From Cell to Bedside* (Zipes, 2009).

16. Desplantez, T., Dupont, E., Severs, N. J. & Weingart, R. Gap Junction Channels and Cardiac Impulse Propagation. *J Membrane Biol* (2007).

17. Dupont, E. Altered Connexin Expression in Human Congestive Heart Failure. *Journal of Molecular and Cellular Cardiology* (2001).

18. Yamada, K. A., Rogers, J. G., Sundset, R., Steinberg, T. H. & Saffitz, J. E. Up-regulation of connexin45 in heart failure. *J. Cardiovasc. Electrophysiol.* (2003).

19. Zhang, Y. *et al.* Connexin43 Expression Levels Influence Intercellular Coupling and Cell Proliferation of Native Murine Cardiac Fibroblasts. *Cell Commun Adhes* (2008).

20. Camelliti, P., Devlin, G. P., Matthews, K. G., Kohl, P. & Green, C. R. Spatially and temporally distinct expression of fibroblast connexins after sheep ventricular infarction. *Cardiovasc. Res.* (2004).

21. Rook, M. B., Jongsma, H. J. & de Jonge, B. Single channel currents of homo- and heterologous gap junctions between cardiac fibroblasts and myocytes. *Pflugers Arch.* (1989).

22. McSpadden, L. C., Kirkton, R. D. & Bursac, N. Electrotonic loading of anisotropic cardiac monolayers by unexcitable cells depends on connexin type and expression level. *AJP: Cell Physiology* (2009).

23. Desplantez, T. *et al.* Relating specific connexin co-expression ratio to connexon composition and gap junction function. *Journal of Molecular and Cellular Cardiology* (2015).

24. Brown, T., Krogh-Madsen, T. & Christini, D. J. Computational Approaches to Understanding the Role of Fibroblast-Myocyte Interactions in Cardiac Arrhythmogenesis. *BioMed Research International* (2015).

25. Wilders, R. Dynamic clamp: a powerful tool in cardiac electrophysiology. *The Journal of Physiology* (2006).

26. Bryant, S. M., Shipsey, S. J. & Hart, G. Regional differences in electrical and mechanical properties of myocytes from guinea-pig hearts with mild left ventricular hypertrophy. *Cardiovasc. Res.* (1997).

27. MacCannell, K. A. *et al.* A Mathematical Model of Electrotonic Interactions between Ventricular Myocytes and Fibroblasts. *Biophysical Journal* (2007).

28. Ahrens-Nicklas, R. C. & Christini, D. J. Anthropomorphizing the mouse cardiac action potential via a novel dynamic clamp method. *Biophysical Journal* (2009).

29. Bot, C. T., Kherlopian, A. R., Ortega, F. A., Christini, D. J. & Krogh-Madsen, T. Rapid genetic algorithm optimization of a mouse computational model: benefits for anthropomorphization of neonatal mouse cardiomyocytes. *Front Physiol* (2012).

30. Livshitz, L. & Rudy, Y. Uniqueness and Stability of Action Potential Models during Rest, Pacing, and Conduction Using Problem-Solving Environment. *Biophysical Journal* (2009).

31. Groenendaal, W. *et al.* Cell-specific cardiac electrophysiology models. *PLoS Comput Biol* (2015).

32. Vogel, R. & Weingart, R. Mathematical model of vertebrate gap junctions derived from electrical measurements on homotypic and heterotypic channels. *The Journal of Physiology* (1998).

33. Desplantez, T., Halliday, D., Dupont, E. & Weingart, R. Cardiac connexins Cx43 and Cx45: formation of diverse gap junction channels with diverse electrical properties. *Pflugers Arch.* (2004).

34. Vogel, R. & Weingart, R. The electrophysiology of gap junctions and gap junction channels and their mathematical modelling. *Biol. Cell* (2002).

35. Henriquez, A. *et al.* Influence of dynamic gap junction resistance on impulse propagation in ventricular myocardium: a computer simulation study. *Biophysical Journal* (2001).

36. Elenes, S., Martinez, A. D., Delmar, M., Beyer, E. C. & Moreno, A. P. Heterotypic Docking of Cx43 and Cx45 Connexons Blocks Fast Voltage Gating of Cx43. *BPJ* (2001).

37. Bukauskas, F. F., Angele, A. B., Verselis, V. K. & Bennett, M. V. L. Coupling asymmetry of heterotypic connexin 45/ connexin 43-EGFP gap junctions: properties of fast and slow gating mechanisms. *Proc. Natl. Acad. Sci. U.S.A.* (2002).

38. Valiunas, V. Biophysical properties of connexin-45 gap junction hemichannels studied in vertebrate cells. *J. Gen. Physiol.* (2002).

39. González, D., Gómez-Hernández, J. M. & Barrio, L. C. Molecular basis of voltage dependence of connexin channels: an integrative appraisal. *Progress in Biophysics and Molecular Biology* (2007).

40. Livshitz, L. M. & Rudy, Y. Regulation of Ca2+ and electrical alternans in cardiac myocytes: role of CAMKII and repolarizing currents. *Am. J. Physiol. Heart Circ. Physiol.* (2007).

41. Nayak, A. R., Shajahan, T. K., Panfilov, A. V. & Pandit, R. Spiral-Wave Dynamics in a Mathematical Model of Human Ventricular Tissue with Myocytes and Fibroblasts. *PLoS ONE* (2013).

42. Xie, Y. *et al.* Effects of fibroblast-myocyte coupling on cardiac conduction and vulnerability to reentry: A computational study. *Heart Rhythm* (2009).

CHAPTER 3

INVESTIGATING THE INFLUENCE OF GAP JUNCTION CHANNEL GATING ON IMPULSE PROPAGATION AND CONDUCTION VELOCITY DURING CARDIAC FIBROSIS*

3.1 Abstract

Gap junctional channel gating is predicted to play a role during pathological conditions such as ischemia or myocardial infarction, especially at heterocellular boundaries in the heart [2, 3]. Cardiac fibrosis plays an important role in these forms of cardiac injury and despite the increasing number of experimental and modeling studies investigating myocyte-fibroblast interactions as discussed in (Section 1.7), an investigation of the effects of gap junctional channel gating on propagation during cardiac fibrosis has not yet been explored. To illuminate these effects, two-dimensional (2D) tissue sheet simulations of cardiac fibrosis and incorporated voltage-dependent gap junction channels in a cell-type specific manner were performed. Two relevant models representing potential structural architectures where myofibroblasts (i.e., activated fibroblasts) are present were explored. First, a myofibroblast insertion model architecture was developed that represents patchy fibrosis in which myofibroblasts disrupt longitudinal and transverse coupling between cardiomyocytes as would occur during replacement fibrosis after myocardial infarction. Then, a two-layer myofibroblast attachment model architecture was developed which represents a layer of myofibroblasts plated over a monolayer of cardiomyocytes as would be found in co-culture experiments. It was determined that in both structural models, incorporating gap junction channel gating only slightly reduces the macroscopic conduction velocity relative to a static representation of gap junction

*Section 3.3, Section 3.4, Figure 3.1, and Figure 3.2 were reproduced from Brown TR, Krogh-Madsen T, and D.J. Christini. Illuminating myocyte-fibroblast homotypic and heterotypic gap junction dynamics using the dynamic-clamp technique. Biophysical Journal. in press. Section 3.2 has been published in full in [1].

coupling. These results provide insight into the implications of the complex interactions between cardiomyocytes and cardiac fibroblasts during cardiac fibrosis and during myocyte-fibroblast coupling in cell culture conditions.

3.2 Introduction

Previous work investigating the effects of gap junction channel gating on cardiac conduction have focused primarily on myocyte-myocyte gap junction channels. Henriquez *et al.* [2] used the Vogel model of dynamic gap junction channels, which represents the voltage- and time-dependent conductance of the gap junction channels, to couple 300 cells in a linear strand using the Lou-Rudy 1 model of ventricular cells [4]. The dynamic gap junction model was compared to a static gap junction model with a constant value conductance. The results showed that when cells were tightly coupled (6700 gap junction channels, equivalent to 491.11 nS) little change was observed in the gap junctional conductance during propagation. However, for poor coupling (85 gap junction channels, equivalent to 6.23 nS), the gap junction conductance inactivates during propagation. This transient change in conductance resulted in increased transjunctional conduction delays, slowing of action potential upstroke, and conduction block.

Lin *et al.* [5] simulated ventricular action potential propagation using a 100 cell cable model using the Faber and Rudy model of a ventricular action potential [6] and dynamic gap junction coupling was modeled using their dynamic model for ventricular junctional conductance [7]. During normal conduction of 64 cm/s and G_j of 2500 nS there is very little change in conduction velocity by the introduction of the V_j-dependent gating. However, the model predicted changes to be seen only when conduction velocity was below 10 cm/s when the V_j is equivalent to the amplitude of and action potential. In this scenario, differences in conduction velocity between the static and the dynamic model were observed. For example, compared with the static model, the dynamic gap

junction model reduces conduction velocity by approximately a third (i.e., from 1.0 cm/s to <0.8 cm/s) at 6 nS of G_j. Furthermore, modeling the effects of 100 nM dose of rotagaptide, a gap junctional conductance enhancer, resulted in a 60% prevention of the conduction slowing, and thus preventing the formation of unidirectional block.

Casaleggio *et al.* [8] incorporated the rectification behavior often seen in heterotypic gap junction channels by modeling a small 2D tissue sheet using the Beeler-Reuter model [9]. They investigated the hypothesis that ischemia alters the properties of gap junctions inside the ischemic area by reducing the average gap junctional conductance, incorporating random fluctuations with time, and by modifying the gap junction rectifying properties along the edges of the ischemic area. These alterations alone resulted in the development of the main types of non-fatal arrhythmia behavior observed in experimental electrocardiogram recordings: single premature ventricular beats, trigeminy complexes, bigeminy complexes, couplets, triplets, and short runs of tachyarrhythmias. In the case of single premature ventricular beats, the main mechanism of arrhythmia formation is that in the presence of a lesion the signal propagation around the scar generates a secondary wave inside the ischemic region, once this wave reaches the normal region it causes a premature beat which then propagates backwards. These results suggest that random fluctuations in the gap conductance inside an ischemic area can promote and modulate the development of specific types of arrhythmic behavior. These studies suggest that while gap junction channel gating may have little effect during normal heart conditions, they may alter cell-to-cell interactions in the heart and modify cardiac arrhythmogenesis under pathological conditions. This chapter expands on this earlier work to investigate whether gap junction channel gating alters myocyte-fibroblast coupling during cardiac fibrosis. The gap junction channel models developed in (Section 2.4) were incorporated in cell-type-specific combinations into 2D tissue sheet models of cardiac fibrosis and the effects of myocyte-fibroblast coupling mediated by Cx43,

Cx45, and Cx43/Cx45 on fibroblast-mediated changes in conduction velocity was investigated.

3.3 Methods

Tissue Model Structure

Cardiac fibrosis was simulated using two different approaches: 1) a randomly generated myofibroblast insertion architecture and 2) a two layer fibroblast attachment architecture, both with increased myofibroblast:myocyte ratio representing increased degrees of cardiac fibrosis. The myocyte electrophysiology was simulated using the Grandi *et al.* human ventricular myocyte model modified by the addition of I_{NaL} [10, 11] and the myofibroblast electrophysiology was simulated using the MacCannell fibroblast model [12], with an increased cell capacitance to represent the myofibroblast phenotype. Gap junction channel models developed in (Section 2.4) were assigned in a cell-type-specific manner: Cx43 for myocyte-myocyte coupling, Cx45 for fibroblast-fibroblast coupling, and Cx43, Cx45 or Cx43/Cx45 for myocyte-fibroblast coupling as indicated. Due to the high computational cost of implementing a large tissue sheet model with discrete gap junction channels, a 10 x 2 mm two-dimensional (2D) tissue sheet model was simulated. The tissue structure was discretized into a 400 x 80 grid of spatial nodes measuring 25 μm x 25 μm. A myocyte was represented by a row of 5 grid points and a capacitance of 125 pF and a myofibroblast was represented by a single grid point and a capacitance of 25 pF. The degree of tissue fibrosis was generated by assigning a target fibroblast to myocyte ratio as described previously [13]. A staggered brick-like structure with 25 μm overlap was chosen to be a simplified but representative model of the histologically structure of cardiac tissue. The tissue simulation was implemented using

a discrete isopotential cell model representation as described in [14] using Equation 3.1.

$$\frac{\mathrm{d}V_\mathrm{i}}{\mathrm{d}t} = -\frac{1}{C_\mathrm{m}}\left[I_\mathrm{total} + I_\mathrm{stim} + \sum_{\mathrm{k}=1}^{\mathrm{N}} G_\mathrm{i,k} \cdot (V_\mathrm{k} - V_\mathrm{i})\right] \tag{3.1}$$

where i and k represent the index of cell i and its neighbor cell k. N is the number of neighboring cells coupled to cell i. V_i is the membrane voltage of the cell and C_m is the membrane capacitance. I_total is the total ionic current flowing through the ion channels, pumps, and exchangers. I_stim is the stimulus current if the cell is located at the stimulus site. $G_\mathrm{i,k}$ represents the junctional conductance between cell i and cell k, which is dependent on the gap junction model used ("static" or "dynamic"). Thus, each myocyte cell is connected to neighboring myocytes or fibroblasts cells via discrete gap junction models positioned at the shared borders between neighboring cells. For myocyte-myocyte coupling, the maximal longitudinal junctional conductance was set to 200 nS and the maximal transverse junctional conductance was set to 100 nS which is similar to previous modeling studies [15, 16] and within the range of values determined by dual-whole cell patch clamp experiments [17]. Less is known about the junctional conductance of fibroblast-fibroblast and myocyte-fibroblast gap junctions. Thus, these junctional conductances was set to 3 nS, which is within the range of 0.3 to 8 nS reported by Rook *et al.* [18].

Conduction velocity, activation time, action potential duration

The tissue sheet is stimulated along the left vertical edge across 10 spatial grid points. Activation time was calculated as the time of the maximum upstroke velocity ($\mathrm{dV_m}/\mathrm{dt}_{max}$) of the cardiomyocyte action potential. The longitudinal and transverse conduction velocity was computed as the linear regression of the earliest activation time vs. the respective x or y coordinate between 25%-75% of the tissue sheet as described previously [19]. In brief, activation time was defined as the occurrence of $\mathrm{dV/dt}_{max}$ during each cardiomyocyte action potential. Since the wavefront can be irregular shape, the

progression of activation along the tissue sheet as a function of distance x was monitored by identifying the earliest activation time at every coordinate x. The longitudinal conduction velocity was then computed by linear regression of the earliest activation time vs. x graph over an observation window spanning 25-75% of tissue sheet width and length to exclude boundary effects. This procedure was then repeated to determine the transverse conduction velocity, and the progression of activation along the tissue sheet as a function of distance y was monitored by identifying the earliest activation time at every coordinate y. Action potential duration was measured using a threshold that was 10% above the resting membrane potential of the cardiomyocyte.

Implementation

All simulations were conducted in C++ and analyzed in MATLAB. Differential equations were solved using the forward Euler method and no flux boundary conditions with a time step of 0.005 ms. The code was parallelized using OpenMP and run on multi-core machines (Dell PowerEdge R410s/R900, 16–24 cores, 12–128 GB memory).

3.4 Results

Effects of myocyte-fibroblast Cx type on impulse propagation during cardiac fibrosis in the myofibroblast insertion model architecture

An investigation into whether myocyte-fibroblast coupling mediated by Cx43, Cx45, or Cx43/Cx45 gap junction channels would have an effect on impulse propagation and conduction velocity during cardiac fibrosis was conducted. First, a myofibroblast insertion architecture model that represents patchy fibrosis in which myofibroblasts disrupt longitudinal and transverse coupling between cardiomyocytes as would occur during replacement fibrosis after myocardial infarction was implement.

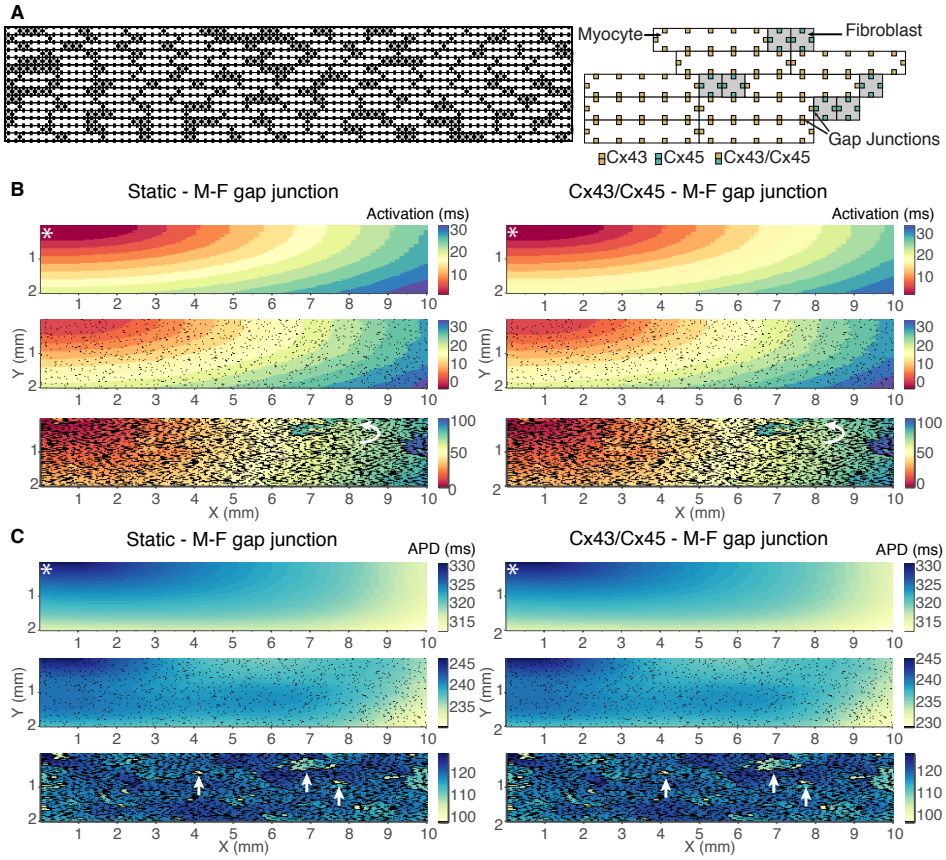

Figure 3.1 | *Myofibroblast insertion model architecture, activation time, and repolarization time.*

(*A*) Schematic representation of the myofibroblast insertion model architecture. Myocytes are represented by white brick-like structures and fibroblasts by grey squares 1/5 the size of cardiomyocytes. On the right panel, Gap junctions are represented by small squares at the border between cells. Myocyte cells are coupled via Cx43 (orange-orange squares), fibroblast cells are coupled via Cx45 (teal-teal squares), and myocyte-fibroblast coupling is via Cx43/Cx45 (orange-teal squares). (*B*) Comparison of activation map between static myocyte-fibroblast coupling and Cx43/Cx45 myocyte-fibroblast coupling. The top panel shows the control simulation during no fibrosis. The middle panel shows simulations during a 0.2:1 fibroblast to myocyte ratio. The bottom panel shows simulations during a 2.8:1 fibroblast to myocyte ratio. Arrows indicate regions of local conduction block and retrograde conduction. (*C*) Comparison of action potential duration map between static myocyte-fibroblast coupling and Cx43/Cx45 myocyte-fibroblast coupling. The top panel shows the control simulation during no fibrosis where action potential duration prolongation is seen around the pacing site. The middle panel shows a 0.2:1 fibroblast to myocyte ratio and illustrates the overall reduction in action potential duration due to fibroblast insertion. The bottom panel shows a 2.8:1 fibroblast to myocyte ratio and markedly increased heterogeneity in action potential duration. Arrows indicate clusters of cardiomyocytes with reduced action potential duration. The stimulus site is indicated by the white asterisk.

The structure of this tissue sheet model is illustrated in Figure 3.1. Figure 3.1 *A-left* shows a segment of the tissue sheet structure with the staggered brick-like arrangement of the cardiomyocytes depicted by white rectangles interspersed with cardiac fibroblasts depicted by grey squares. The arrangement of the gap junction channels is illustrated in Figure 3.1 *A-right* by the smaller squares at the shared borders between neighboring cells. In Figure 3.1 *B* a comparison of the activation time during myocyte-fibroblast coupling mediated by static gap junction models vs. Cx43/Cx45 gap junction models is shown. The top panels demonstrate the control simulation during no fibrosis. The stimulus site was at the top left corner of the tissue sheet. The activation map is smooth despite the staggered structure of the tissue sheet. The middle panel represents 0.2:1 fibroblast to myocyte ratio, where the fibroblasts are relatively dispersed in the tissue sheet. There is relatively little disruption in the smoothness of the activation map. The bottom panel shows a 2.8:1 fibroblast to myocyte ratio, which is equivalent to a patchy fibrosis morphology, where the cardiac fibroblast clusters result in decoupling of cardiomyocytes in the longitudinal and transverse directions [20]. The activation map is very heterogeneous, with areas of local conduction block and retrograde conduction shown by the curved arrow. The results show that the Cx43/Cx45 and other Cx phenotypes (not shown) have similar conduction properties to that of the static myocyte-fibroblast gap junction model, suggesting that the time- and V_j-dependent gating properties do not play a significant role in modifying activation time. In Figure 3.1 *C* a comparison between the cardiomyocyte action potential duration during myocyte-fibroblast coupling mediated by static gap junction models vs. Cx43/Cx45 gap junction models is shown. In the top panel, the action potential duration is prolonged around the pacing site as expected [21] and ranges from 315–330 ms when no fibrosis is present. The middle panel illustrates the overall reduction in action potential duration to a range of 235–245 ms due to the insertion of fibroblasts into the tissue sheet.

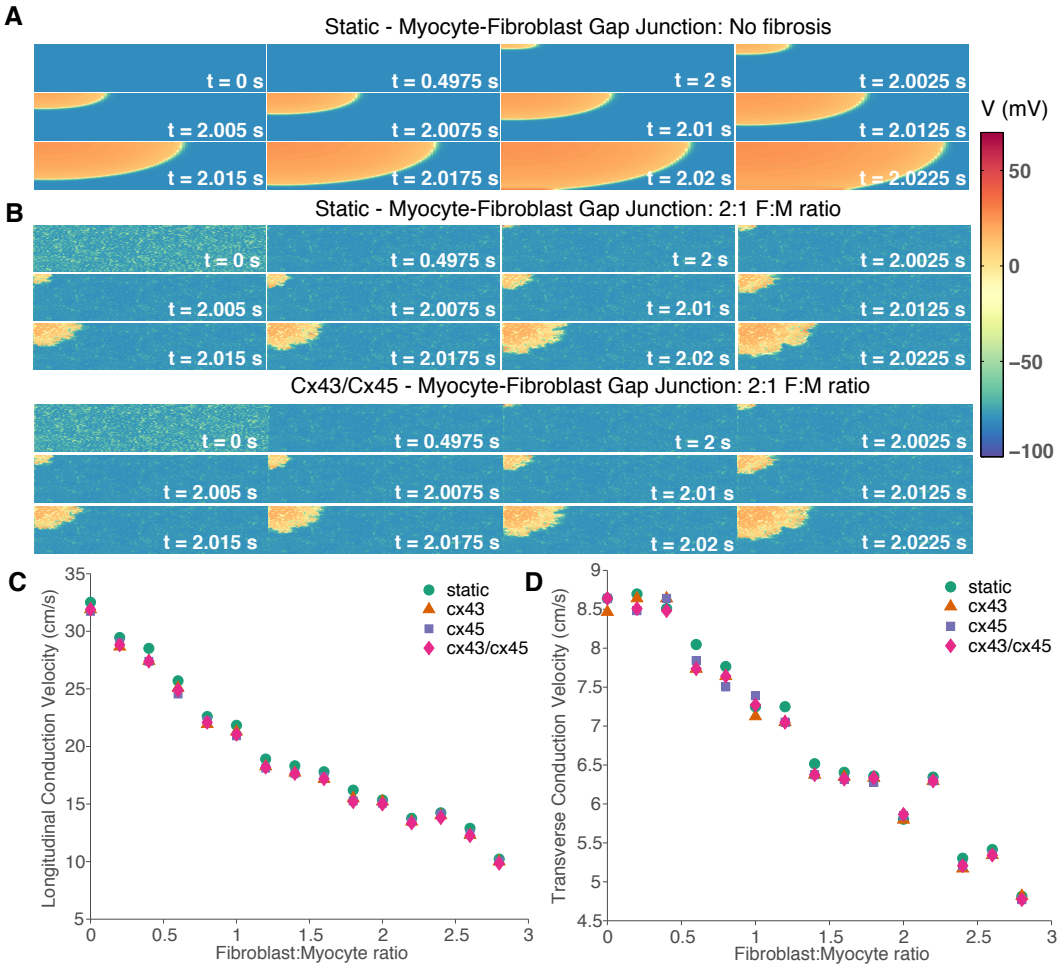

Figure 3.2 | *Effects of myocyte-fibroblast Cx phenotype on conduction velocity – myofibroblast insertion model architecture.*
The tissue sheet is stimulated along the top left corner of the tissue sheet. Each panel shows snapshots of the membrane voltage at the indicated time points. (*A*) Homogenous membrane potential of the cardiomyocytes and smooth impulse propagation. (*B*) Comparison of membrane voltage between static myocyte-fibroblast coupling (*top*) and Cx43/Cx45 myocyte-fibroblast coupling (*bottom*) with a 2:1 fibroblast to myocyte ratio of medium fibrosis. At t = 0 s, before the start of the simulation the fibroblasts are relatively depolarized compared to the cardiomyocytes. At t ≈ 0.5 s, the coupled myocytes and fibroblasts reach a new equilibrium potential where the myocytes are depolarized and the fibroblasts are hyperpolarized compared to t = 0 s. The wavefront is very heterogeneous and longitudinal conduction velocity is reduced by 50%. (*C* and *D*) Comparison of longitudinal and transverse conduction velocity as a function of fibroblast to myocyte ratio, for differing myocyte-fibroblast gap junction channel models. There is a small reduction in the conduction velocity across all degrees of fibrosis, but there is very little difference between myocyte-fibroblast coupling mediated by the three different Cx types.

The bottom panel shows the markedly increased heterogeneity in action potential duration due to enhanced fibrosis; the increased occurrence of clusters of cardiomyocytes with reduced action potential duration as indicated by the arrows.

Figure 3.2 illustrates the effects of increased cardiac fibrosis on conduction velocity. In the absence of fibroblasts (Figure 3.2 *A*), the wavefront is relatively smooth. Increasing the degree of fibrosis to 2:1 fibroblast to myocyte ratio (Figure 3.2 *B*) resulted in a heterogeneous wavefront of propagation as well as slowed conduction across the tissue sheet. The propagation of the Cx43/Cx45 myocyte-fibroblast coupling and other Cx types (not shown) were similar to the static gap junction model representation, suggesting that time- and V_j-dependent gating of the gap junction channels does not play a significant role in conduction velocity. Figure 3.2 *C* and *D* shows the conduction velocity measured between $25\% - 75\%$ of the tissue sheet length in both the transverse and longitudinal direction. It showed a 50% reduction in the longitudinal conduction velocity and a 30% reduction in transverse conduction velocity when comparing no fibrosis to 2:1 fibroblast to myocyte ratio. In Figure 3.2 *D* at low fibroblast to myocyte ratio ($0.5 - 1$) there are small differences in the transverse conduction for the Cx45 phenotypes. However, the conduction velocity is essentially independent of the type of myocyte-fibroblast gap junction channel model.

Effects of myocyte-fibroblast Cx type on impulse propagation in a two layer myofibroblast attachment model architecture

The myofibroblast insertion model architecture showed a high degree of discontinuous conduction for >40% fibrosis (fibroblast to myocyte ratio >2:1), this is due to the myofibroblast insertion resulting in both the disruption of myocyte-myocyte coupling as well as acting as an electrotonic load on the cardiomyocytes.

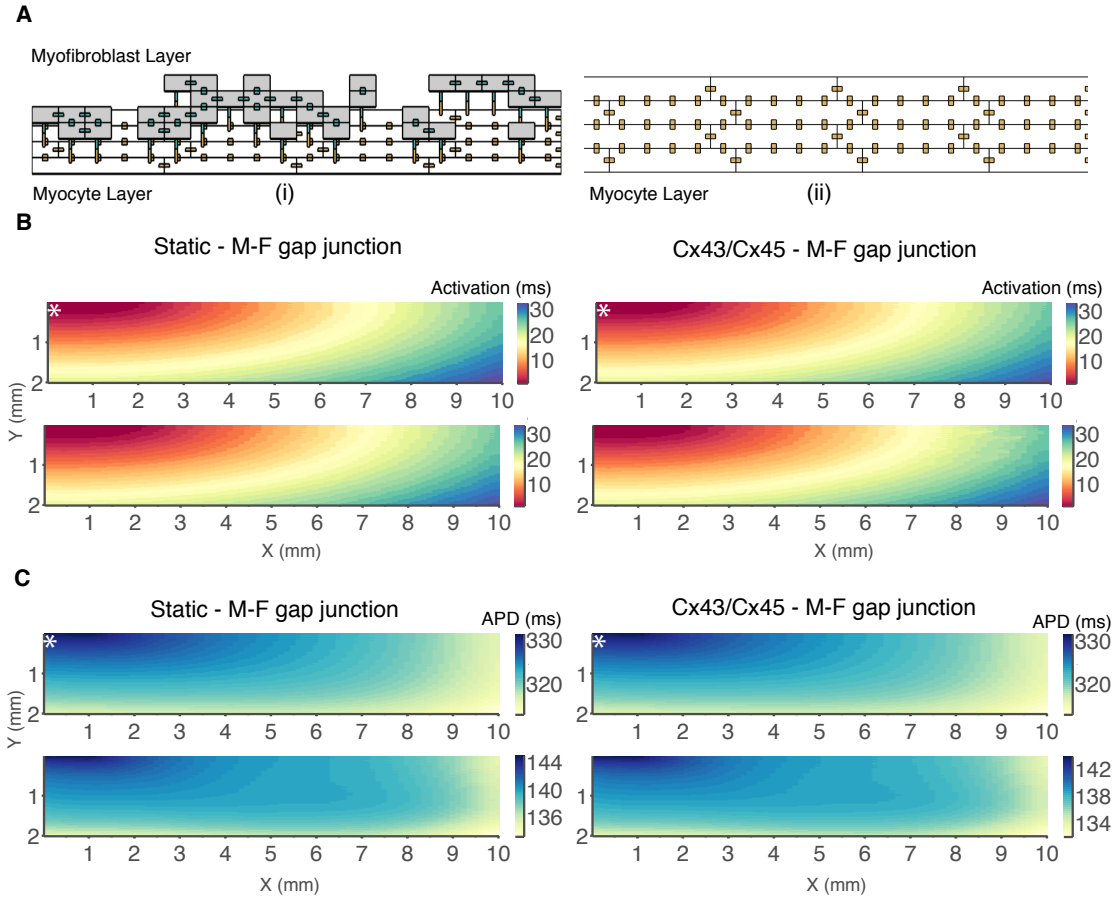

Figure 3.3 | *Two layer myofibroblast attachment model architecture, activation time, and repolarization time*

(*A*) Schematic representation of the two layer myofibroblast attachment model architecture of cardiac fibrosis. (i) Myocytes are represented by the white brick-like structures in the bottom layer and myofibroblasts are represented by grey squares in the top layer and are 1/5 the size of cardiomyocytes. Gap junction channels are represented by the smaller squares located at the border between neighboring cells. Myofibroblast cells are coupled to each other via Cx45 gap junction channels (*teal-teal squares*) and myocyte-myofibroblast coupling between the two layers is via Cx45 gap junction channels (*blue squares*). (ii) View from below shows the bottom layer containing cardiomyocytes only coupled to each other via Cx43 gap junctions (*orange-orange squares*). (*B*) Comparison of activation map between static myocyte-fibroblast coupling and Cx43/Cx45 myocyte-fibroblast coupling. (top panel) No fibrosis, (bottom panel) 2.5:1 fibroblast to myocyte ratio. (*C*) Comparison of action potential duration map between static myocyte-myofibroblast coupling and Cx43/Cx45 myocyte-myofibroblast coupling. (top panel) No fibrosis, (bottom panel) 2.5:1 fibroblast to myocyte ratio. The results illustrate the overall reduction in action potential duration due to fibroblasts coupling to the myocyte layer and resulting in early repolarization of the cardiomyocyte. The stimulus site is indicated by the white asterisk.

In order to gain insight into the relative contribution of the myocyte-myocyte uncoupling vs. the electrotonic effects of the myofibroblasts, a two-layer myofibroblast attachment model architecture was implemented in which myofibroblasts act only as an electrotonic load on the cardiomyocytes. In this model a layer of fibroblasts is simulated on top of a layer of cardiomyocytes as illustrated in (Figure 3.3 *A*) and myocyte-fibroblast coupling occurs across the two layers. This architecture is structurally similar to fibroblasts plated over a monolayer of cardiomyocytes as found in many co-culture experiments. In Figure 3.3 *B* activation time during myocyte-fibroblast coupling mediated by static gap junction models was compared with activation time mediated by Cx43/Cx45 gap junction models. The top panels demonstrate the control simulation during no fibrosis and the bottom panel shows a 2.5:1 fibroblast to myocyte ratio. In contrast to the myofibroblast insertion model, the two layer model activation map remains smooth despite a large increase in the number of myofibroblasts (compare Figure 3.3 *B bottom panel* to Figure 3.1 *B bottom panel*). The results show that the Cx43/Cx45 and other Cx phenotypes (not shown) have similar conduction properties to that of the static myocyte-fibroblast gap junction model, suggesting that the time- and V_j-dependent gating properties of the gap junctions do not play a significant role in modifying activation time.

Figure 3.3 *C* compares the cardiomyocyte action potential duration during myocyte-fibroblast coupling mediated by static gap junction models vs. Cx43/Cx45 gap junction models. While the action potential duration is reduced to a similar extent as the myofibroblast insertion model, there are no clusters of cardiomyocytes with reduced action potential duration (compare Figure 3.3 *C bottom panel* to Figure 3.1 *C bottom panel*). These results demonstrate that the heterogenous conduction behavior of the insertion model is largely as a result of the disruption of myocyte-myocyte coupling by the insertion of myofibroblasts. As shown in Figure 3.4, the effects on conduction velocity is

smaller for the attachment model compared to the insertion model, because of the lack of myocyte-myocyte uncoupling in this tissue architecture. The conduction velocity vs. fibroblast to myocyte ratio results in a biphasic relationship in which there is an initial increase in conduction velocity followed by a decrease in conduction velocity which is not seen in the myofibroblast insertion model. The mechanism is that elevation of the membrane potential first increases conduction velocity by bringing the myocyte closer to the threshold of I_{Na} but then decreases conduction velocity as I_{Na} is progressively inactivated as previously demonstrated by [13].

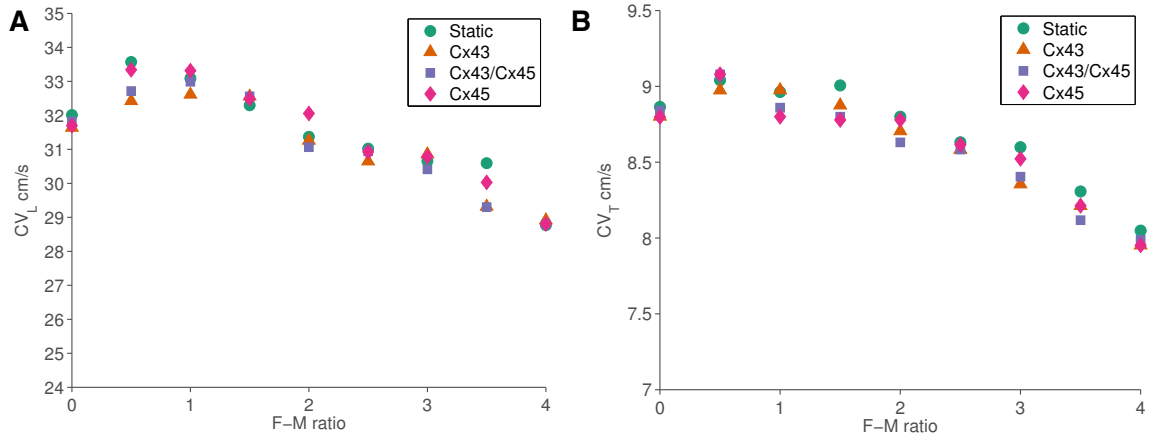

Figure 3.4 | *Effects of myocyte-fibroblast Cx phenotype on conduction velocity – myofibroblast attachment model architecture.*
(*A* and *B*) Comparison of longitudinal and transverse conduction velocity as a function of fibroblast to myocyte ratio, for static, Cx43, Cx45, and Cx43/Cx45 myocyte-fibroblast gap junction channel models. There is a biphasic effect on conduction velocity as the fibroblast to myocyte ratio is increased.

3.5 Discussion

It was hypothesized that the dynamic properties of gap junction channels may modulate cardiac conduction during diseased states. In particular, for the case of heterotypic Cx43/Cx45 gap junction channels with asymmetric conductance-voltage relationships,

it was predicted that such channels may impede current flow in one direction and facilitate it in the opposite direction [3]. Thus, this study explored whether varying the myocyte-fibroblast gap junction channel's phenotype (i.e., between homotypic Cx43, homotypic Cx45, and heterotypic Cx43/Cx45) would play a role in modifying impulse propagation during cardiac fibrosis. In the tissue-level simulations, gap junction channel gating does not significantly alter activation time (see Figure 3.1 *B* and Figure 3.3 *B*), repolarization time (see Figure 3.1 *C* and Figure 3.3 *C*), and conduction velocity (see Figure 3.2 and Figure 3.4) in the 2D tissue sheet models of cardiac fibrosis explored. This is due to the relatively slow dynamics of gap junction channel gating and the small transjunctional voltages observed between the cardiomyocytes and fibroblasts during the course of the action potential. Recent work by Casaleggio *et al.* [8] incorporated the rectification behavior of heterotypic Cx43/Cx45 gap junction channels and showed that varying the average and variance of the gap junctional conductance promoted and modulated the development of specific types of arrhythmic behavior. However, their gap junction models were assumed to instantaneous reach steady-state levels of inactivation. This likely overestimates the degree of inactivation of the gap junction channels during the time course of an action potential. Furthermore, prior work by Henriquez *et al.* demonstrated in a cardiomyocyte fiber model that during poor coupling the time- and transjunctional voltage-dependent gating of gap junction channels resulted in increases in junctional resistance that resulted in increased conduction delays compared to a static gap junction model [2]. This difference is likely due to the existence of alternative strongly coupled myocyte-myocyte conduction pathways in the 2D tissue structure that help maintain the conduction velocity, which is not present in the 1D fiber model.

3.6 Conclusions

This study determined that although gap junction channel gating reduces junctional current during the upstroke of the action potential, the macroscopic conduction velocity was only slightly modified for Cx43, Cx45, and Cx43/Cx45 gating relative to a static representation of gap junction coupling. Thus, it was determined that gap junction channel gating does not significantly alter impulse propagation and conduction velocity under the conditions studied. These results can provide insight into the role of gap junctions phenotypes during cardiac fibrosis and myocyte-fibroblast coupling in cell culture conditions. Future investigations can explore the compound effects of heart failure remodeling of cardiomyocytes during cardiac fibrosis and further modifications of gap junction properties thought to occur under such conditions such as the effects of intracellular acidification and changes in phosphorylation states [22].

BIBLIOGRAPHY

1. Brown, T., Krogh-Madsen, T. & Christini, D. J. Computational Approaches to Understanding the Role of Fibroblast-Myocyte Interactions in Cardiac Arrhythmogenesis. *BioMed Research International* (2015).

2. Henriquez, A. *et al.* Influence of dynamic gap junction resistance on impulse propagation in ventricular myocardium: a computer simulation study. *Biophysical Journal* (2001).

3. Desplantez, T., Dupont, E., Severs, N. J. & Weingart, R. Gap Junction Channels and Cardiac Impulse Propagation. *J Membrane Biol* (2007).

4. Luo, C. H. & Rudy, Y. A model of the ventricular cardiac action potential. Depolarization, repolarization, and their interaction. *Circ. Res.* (1991).

5. Lin, X., Zemlin, C., Hennan, J. K. & Petersen, J. S. Enhancement of ventricular gap-junction coupling by rotigaptide. *Cardiovasc. Res.* (2008).

6. Faber, G. M. & Rudy, Y. Action Potential and Contractility Changes in [Na+]i Overloaded Cardiac Myocytes: A Simulation Study. *Biophysical Journal* (2000).

7. Lin, X., Gemel, J., Beyer, E. C. & Veenstra, R. D. Dynamic model for ventricular junctional conductance during the cardiac action potential. *Am. J. Physiol. Heart Circ. Physiol.* (2005).

8. Casaleggio, A, Hines, M. L. & Migliore, M. Computational model of erratic arrhythmias in a cardiac cell network: the role of gap junctions. *PLoS ONE* (2014).

9. Beeler, G. W. & Reuter, H. Reconstruction of the action potential of ventricular myocardial fibres. *The Journal of Physiology* (1977).

10. Trenor, B. *et al.* Simulation and Mechanistic Investigation of the Arrhythmogenic Role of the Late Sodium Current in Human Heart Failure. *PLoS ONE* (2012).

11. Grandi, E., Pasqualini, F. S. & Bers, D. M. A novel computational model of the human ventricular action potential and Ca transient. *Journal of Molecular and Cellular Cardiology* (2010).

12. MacCannell, K. A. *et al.* A Mathematical Model of Electrotonic Interactions between Ventricular Myocytes and Fibroblasts. *Biophysical Journal* (2007).

13. Xie, Y. *et al.* Effects of fibroblast-myocyte coupling on cardiac conduction and vulnerability to reentry: A computational study. *Heart Rhythm* (2009).

14. Keener, J. P. The effects of gap junctions on propagation in myocardium: a modified cable theory. *Annals of the New York Academy of Sciences* (1990).

15. Hubbard, M. L., Ying, W & Henriquez, C. Effect of gap junction distribution on impulse propagation in a monolayer of myocytes: a model study. *Europace* (2007).

16. Xie, Y, Garfinkel, A, Weiss, J. N. & Qu, Z. Cardiac alternans induced by fibroblast-myocyte coupling: mechanistic insights from computational models. *AJP: Heart and Circulatory Physiology* (2009).

17. Yao, J.-A. *et al.* Remodeling of gap junctional channel function in epicardial border zone of healing canine infarcts. *Circ. Res.* (2003).

18. Rook, M. B. *et al.* Differences in Gap Junction Channels Between Cardiac Myocytes, Fibroblasts, and Heterologous Pairs. *Am. J. Physiol.* (1992).

19. Prudat, Y. & Kucera, J. P. Nonlinear behaviour of conduction and block in cardiac tissue with heterogeneous expression of connexin 43. *Journal of Molecular and Cellular Cardiology* (2014).

20. De Jong, S., van Veen, T. A. B., van Rijen, H. V. M. & de Bakker, J. M. T. Fibrosis and cardiac arrhythmias. *J. Cardiovasc. Pharmacol.* (2011).

21. Krogh-Madsen, T. & Christini, D. J. Action Potential Duration Dispersion and Alternans in Simulated Heterogeneous Cardiac Tissue with a Structural Barrier. *Biophysical Journal* (2007).

22. Wit, A. L. & Peters, N. S. The role of gap junctions in the arrhythmias of ischemia and infarction. *HRTHM* (2012).

CHAPTER 4

A NEW APPROACH TO INVESTIGATING MYOCYTE-FIBROBLAST INTERACTIONS IN CARDIAC TISSUE SLICES

4.1 Abstract

Due to the intermingled structure of cardiomyocytes and fibroblasts in the heart, it has been challenging to study their interactions using whole heart models. Therefore, many experimental studies investigating myocyte-fibroblast interactions have been predominantly conducted using *in vitro* cell culture models. Although the co-culture of cardiomyocytes and fibroblasts allow for valuable insight into the implications of myocyte-fibroblast interactions, they may be limited in their capacity to reproduce *in vivo* behavior. Thus, an intermediate experimental model, such as cardiac tissue slices, may provide valuable insight into the implications and extent of myocyte-fibroblast interactions in tissue. In this chapter, a new approach to investigate cell-to-cell interactions using a dye transfer method in acute cardiac tissue slices is proposed. As a proof-of-principle, the cardiac tissue slice model is used to investigate myocyte-myocyte and myocyte-fibroblast functional coupling. Gap junction permeable and impermeable fluorescent tracers were iontophoretically injected into targeted myocyte and fibroblast-like cells and dye transfer was visualized both in the live recording setup and after fixation and immunostaining. These results demonstrate that cardiac tissue slices have preserved architecture which is optically accessible using standard patch-clamp equipment and allow for the targeting of individual cells. Furthermore, the results show that combining dye transfer studies to determine functional coupling of cells with immunohistochemical identification of the targeted cell types is technically challenging but feasible. Thus, this is a promising technique to investigate the complex cell-to-cell interactions in cardiac tissue.

4.2 Introduction

Cardiac tissue slice as a cardiac electrophysiology model

In 1990, Burnashev et al. [1] demonstrated using thin slices from the neonatal rat ventricle, that cardiac tissue slices are a viable experimental model for performing patch-clamp recordings. Although the resting potential of the *in situ* cardiomyocytes during these earlier attempts were relatively depolarized (-35 to -65mV), the average sodium currents and inward rectifying currents measured using the cell-attached patch-clamp method were similar to recordings from isolated rat ventricular cells. In 2003, Pillekamp et al. [2] reestablished the model in the embryonic mouse heart and later in the adult mouse heart opening the opportunity to generate cardiac tissue slices from wild-type and genetically engineering mouse models for physiological and pharmacological studies. Furthermore, cardiac tissue slice protocols were established for the adult guinea pig heart model in 2009 [3] and for human ventricular tissue in 2011 [4]. These studies presented significant methodological improvements in slice preparation and the preservation of the live samples. Since, the reemergence of the cardiac tissue slice model it has been used to investigate the electrophysiological integration of cardiomyocytes after transplantation [5], to investigate the utility of cardiac tissue slices in pharmacological drug testing [6], and to investigate its utility as a tissue-engineered graft model [7].

There are several advantages to using cardiac tissue slices for studying cell-to-cell interactions in the heart. Acute cardiac tissue slices have more preserved microstructural properties compared to the enzymatically isolated cardiomyocyte model and to primary cell culture monolayers [8]. Moreover, field potential and action potential recordings in response to pharmacological manipulation in tissue slices from the rabbit and guinea pig heart have shown a significant correlation with results from well established electrophysiology models [9]. Furthermore, cardiac tissue slices are more suitable for optical

imaging [10] compared to other organotypic models such as the ventricular wedge and papillary muscle preparation. This is due to the ability to generate relatively thin precision cut slices which transmit light with less scattering. These two properties make this model suitable for investigating intercellular communication in a preserved multicellular environment which offers access to structural and morphological information via light and epi-fluorescent microscopy and functional measures using electrophysiological techniques.

Due to the need to individually evaluate intercellular coupling between two distinct cell types (i.e., cardiomyocytes and fibroblasts) in the cardiac tissue slice, the microinjection method of assaying gap junctional coupling as described in Figure 1.7*A* was used. The dual tracer technique, which involves the microinjection of the target cell with two membrane-impermeable dyes, one that is gap junction impermeable and another that is gap junction permeable was implemented as indicated. The gap junction impermeable dye provides an internal control that the target cell is intact, while the gap junction permeable dye will diffuse into coupled neighboring cells, as illustrated in Figure 4.1.

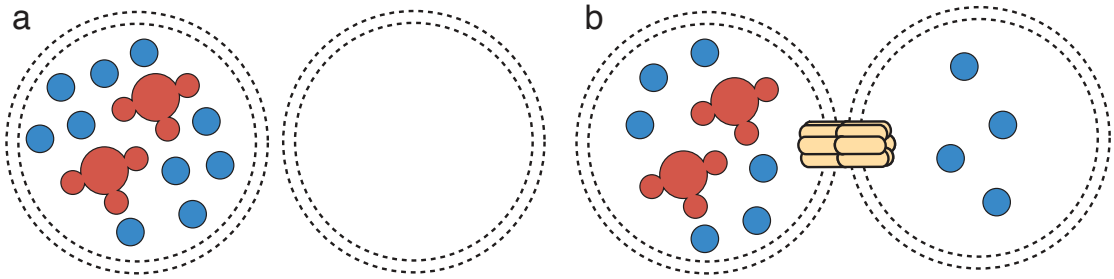

Figure 4.1 | *Dual tracer technique*
Cells are injected with a mixture of a small polar tracer (blue) and a relatively large dextran conjugated tracer (red). [Left] Uncoupled cells: both the low molecular weight tracer and the much larger dextran conjugate remains in the initially injected cell. [Right] Coupled cells: the low molecular weight tracer will transfer to its neighbors, whereas the much larger dextran conjugate tracer remains in the initial target cell.

Previously, the dual tracer technique has been applied to cell culture preparations [11], but the morphology of the tissue is often disrupted in cell culture prepara-

tions. Likewise, the dual tracer technique has also been applied to scrape loading experiments, but due to the method of loading multiple cells simultaneously with dye it is difficult to track dye transfer [12]. Applying the dual tracer technique to microinjection experiments in cardiac tissue slices overcomes these methodological limitations.

4.3 Materials and Methods

Cardiac slice preparation

Ventricular heart slices were prepared from adult female/male guinea pigs, body weight 450 g, obtained from (Charles River, Sulzfeld, Germany). All procedures were performed in accordance with the Weill Cornell IACUC protocol 0701-571A. Acute tissue slices from the guinea pig heart are prepared as described previously [3, 6]. In brief, guinea pigs were weighed and an intraperitoneal injection of 500U Heparin was performed. After 10 mins the guinea pig was euthanized using i.p. injection of 120 mg/kg sodium pentobarbital. The heart was quickly removed and placed in oxygenated (5% Carbon dioxide; 95% Oxygen) ice-cold Tyrode's (in mM):126.7 NaCl, 5.4 KCl, 1.05 $MgCl_2$, 1.8 $CaCl_2$, 0.42 NaH_2PO_4, 22 $NaHCO_3$, 5 Glucose, supplemented with Heparin. The heart was then prepared for Langendorf perfusion by removing fat tissue and the pericardial sac. The heart is then cannulated on a Langendorff apparatus, it is first perfused with oxygenated Tyrode's to facilitate the removal of blood, followed by perfusion with high K^+ Tyrode's (in mM):106.7 NaCl, 20 KCl, 1.05 $MgCl_2$, 1.8 $CaCl_2$, 0.42 NaH_2PO_4, 22 $NaHCO_3$, 5 Glucose, supplemented with 2,3-butanedione monoxide (HK-BDM) to inhibit myocyte contractions.

A tissue chunk measuring approximately 10 x 4 mm and spanning the thickness was dissected from the left ventricle and glued used histoacryl tissue adhesive (ProgressiveMed) to a magnetic specimen disc with the epicardium facing up. The magnetic disc

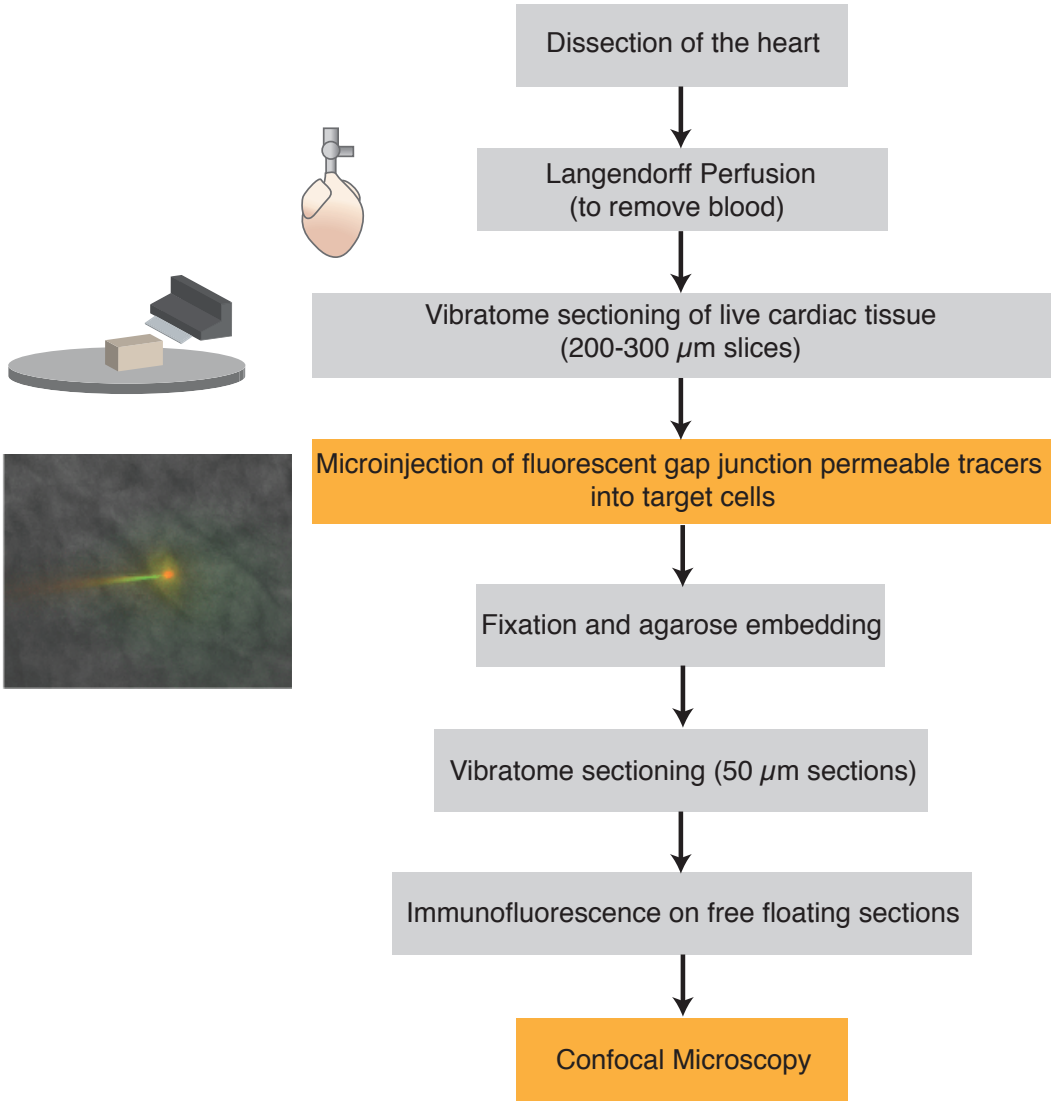

Figure 4.2 | *Overview of protocol steps*
The heart is dissected and Langendorff perfusion is used to remove blood, followed by vibratome sectioning of live cardiac tissue into 200−300 microns slices. The generated acute cardiac tissue slices are placed in a recording chamber with oxygenated Common Tyrode's solution. Microinjections targeting individual cardiomyocytes and fibroblasts were performed under IR/DIC optics, iontophoretic dye injections lasted for 5 mins and used either the gap junction permeable tracers. Samples were fixed in 4% parafomaldehyde then thin sectioned using a vibratome or cryostat. Immunohistochemistry was performed to identify target cell types. Images were captured using confocal microscopy.

was placed in the base of the buffer tray of the vibratome (VT1000S, Leica Microsystems). The sample was positioned as flat as possible and the long axis of the tissue chunk was oriented perpendicular to the vibratome blade. The buffer tray was filled with ice-cold HK-BDM and the outer area of the vibratome chamber was filled with ice. Using a vibratome blade speed of 0.025–0.050 mm/s, an amplitude of 1 mm, and a frequency of 85 Hz. On average, 6–10 slices at 250–300 μm in thickness were generated. The slice thickness was determined empirically based on a compromise between two factors: thinner slices tend to be more damaged, whereas thicker slices result in reduced nutrient supply to the center of the tissue and reduced optical transparency. Using a fine-tip paintbrush, the slices were transferred to a pre-incubation chamber containing oxygenated Tyrode's supplemented with BDM at 25°C. Slices were kept in the preincubation chamber for at least 1 hour of recovery before the start of the microinjection experiments.

Field potential Recordings

A multi-electrode array (MEA)-System with a MEA1060-Up amplifier, a TC01 temperature controller, and a 60 electrodes MEA (8 x8 grid with 200 μm inter electrode spacing and 30 μm electrode diameter) was used to measure field potential recordings from tissue slices in response to bipolar electrode stimulation. MC_Stimulus software was setup with a threshold protocol and the MC_Rack software was used to define the recording protocol. A stimulus site located at the edge of the tissue was found and the stimulus threshold test was performed using MC_stimulus. The threshold test consisted of bipolar pulses between 1–5 V, 1000 μs duration, at 1 Hz frequency. Once a threshold pulse was determined, field potentials were recorded for 20–60s every 1–2 hour(s) for up to 7 hrs for the time-lapse MEA recording to access the stability of the tissue slices over time using the MC_Rack software. The data was then exported using the MC_DataTool software and analyze using custom MATLAB scripts.

Iontophoretic microinjection

Microinjection pipettes from borosilicate glass capillaries (World Precision Instruments, #1B100F-4) were pulled with a micropipette puller (P-1000 Micropipette Puller, Sutter Instruments). A good microinjection pipette had a fine tip and a longer taper and a resistance >30 MΩ. Pipettes were designed with a fine enough tip to allow for minimal cell damage during microinjection, but large enough to allow for adequate dye diffusion. Micropipette tips were filled with microinjection solution via capillary action and then backfilled with intracellular solution (in mM):113 KCL,11 KOH,10 NaCl,0.5 $MgCl_2$,10 HEPES,5.5 Dextrose, 5 K_2ATP, 7.1 pH adjusted with KOH. Before the start of the experiment the filled pipettes were visually accessed for excess dye leakage and control of iontophoretic dye outflow using epi-fluorescence and a square 0.1 nA current pulse of 900 ms duration and 0.5 Hz frequency using (Patch Clamp Amplifier Model 2400& Model 2100 Isolated Pulse Stimulator, A-M Systems).

Slices were then loaded into the recording chamber (RC-27LD, Warner Instruments, #64-0241) on a fixed stage microscope (Olympus BX51WI with IR/DIC optics) equipped with a light source (SOLA light engine, Lumencor) and stabilized with a custom made slice hold down. Slices were superfused at a rate of 1–2 ml/min with oxygenated Tyrode's solution at 37°C. A target cell was then found in the tissue slice away from the cut surface of the tissue slice that were damage by the vibratome sectioning. To improve visualization of target cells, it is important to achieve Kohler illumination in which the light is focused on the same plane as the target cell (see [13]). In brief, Kohler illumination was obtained by focusing on the target cell by closing down the microscope field diaphragm, adjusting the height of the condenser so that it is in focus and centered and then reopen the field diaphragm so it is just outside the field of view. DIC optics are adjusted to enhance contrast by rotating the polarizer.

The pipette was lowered into the bath and positioned at the center of the field of

Table 4.1 | Fluorescent Tracers

Fluorophore	Molecular weight	Charge
Alexa 350 Hydrazide	349.29	-1
Lucifer yellow CH	457.25	-2
Alexa 488 Hydrazide	570.48	-1
Alexa 594 Hydrazide	758.79	-1
Alexa 568-Dextran	10,000	-1

view under 4x magnification and visualized using live imaging software (HCImage live, Hamamatsu Photonics). The objective was switched to 40x magnification and the pipette tip was located. The pipette tip was positioned above the target cell and moved towards the cell by adjusting focus and lowering the pipette with the micromanipulator in a stepwise fashion. Once the pipette was positioned directly over the cell, the fluorescence filter was switched on and the cell was microinjected iontophoretically for 5 mins. The spread of the dye during microinjection and post microinjection was captured with a CMOS camera (ORCA-Flash2.8 CMOS camera, Hamamatsu Photonics).

Immunostaining

Following microinjection of a tissue slice, the slice was removed from the recording chamber and place in a well of a 12-well plate containing oxygenated Common Tyrode's solution. Using a separate fine-tip paintbrush, each sample was transferred to a well containing 500 μl of 4% (wt/vol) paraformaldehyde in Phosphate Buffered Saline (PBS). The tissue sample was fixed for 30 min at room temperature (RT) before incubating the sample at 4°C overnight on a shaker in the dark. After overnight fixation at 4°C in PFA (Electron microscopy sciences, #157-4), the slices were washed 3x for 15 mins each in 0.1 M PBS. A paintbrush was used to transfer the slices between wells or solution was removed from wells using a pipette. After the last wash, slices were sometimes stored at 4°C for up to 2–3 days in 0.1 M PBS with 0.05% NaN_3. The tissue slices were then resection to obtain 25–50 μm vibratome sections. This was completed by embedding

samples in 3% and 6% low-melting-point agarose (Sigma, #A9414). A drop of 3% agarose was placed on a heated microscope slide with spacers matching the thickness of the tissue slice and the slice was placed into the drop using a small paintbrush. A coverslip was placed on top to slightly flatten the sample and cooled to solidify. The thin block of agarose containing slice was trimmed and then placed in the bottom of a cryostat mold being careful not to trap air bubbles. The remainder of the mold was filled with 6% agarose and placed on ice to solidify. The solidified agarose block containing the slice was trimmed, leaving a small amount of excess agarose around sample. The agarose block was oriented on the vibratome platform such that the cut surfaces of the slice are parallel to the cutting blade of the vibratome. 25–50 μm thick sections were then cut with the vibratome. A fine-tip paintbrush was used to transfer the floating vibratome sections into a 24-well plate containing 1x PBS (one slice per well).

The thin sections were washed with PBS 3x for 15 min each, then blocked for 1 hr at RT in Blocking Buffer: 0.3% Triton-PBS (Sigma, #93443), 3% donkey serum, 2% BSA. They were then incubated in blocking buffer containin primary antibody overnight at 4°C (or 3–8 h at room temperature) on a shaker. The sections were then transferred to a new multiwell dish using a separate paintbrush for each primary antibody (or antibody combination) and then washed in PBS 3x for 15 mins each and then blocked for 30 mins at RT in Blocking Buffer. The sections were then incubated in diluted secondary antibodies (1:1000) for 2 hr at RT. After incubation, they were then wash in PBS 3x for 15 mins and then incubated with DAPI (4',6-diamidino-2-phenylindole; Molecular Probes) for 1 h at room temperature and then washed with PBS 3x for 5 mins. The sections were then mounted using secure seal spacers (Electron Microscopy Sciences, #70327-9S) and Prolong Gold anti-fade reagent and coversliped. Finally, the samples were imaged using confocal microscopy.

Confocal Imaging

Confocal acquisitions were performed on an LSM510 Zeiss microscope equipped with an argon laser (488 nm excitation), two helium-neon lasers (543 nm and 633 nm excitation) and a 63x/1.4 Plan-Apochromat objective.

4.4 Results

Morphology of acute cardiac tissue slices

In order to generate viable acute cardiac tissue slices, certain preparation, storage, and handling conditions must be considered. First, the dimension of cardiac slices relative to the dimensions of an individual cardiomyocyte is important for tissue viability. Adult guinea pig cardiomyocytes are $\approx$142 μm in length and $\approx$32 μm in width and $\approx$13 μm in depth [14]. Thus, a 250 μm tissue slice with cells oriented parallel to the epicardial surface would approximately contain 20 layers of cells. Cardiac tissue slices were generated at 250$-$300 μm in thickness in the plane of the epicardial surface (i.e. tangential slices). These dimensions were determined empirically to: 1) allow for oxygen diffusion through cardiac slices, 2) to obtain more parallel cardiomyocyte fibers, and 3) to allow for enough surface area to visualize dye transfer. Moreover, tangential orientation of slices also allow for the better visualization of dye diffusion. Figure 4.3 *A*, shows a comparison between regions of a tissue slice in which cardiomyocytes are predominantly oriented in cross-section, versus when the muscle fibers are oriented parallel to the plane of the slice. Second, it is important to use sharp blades positioned at an angle to reduce damage to the tissue slice.

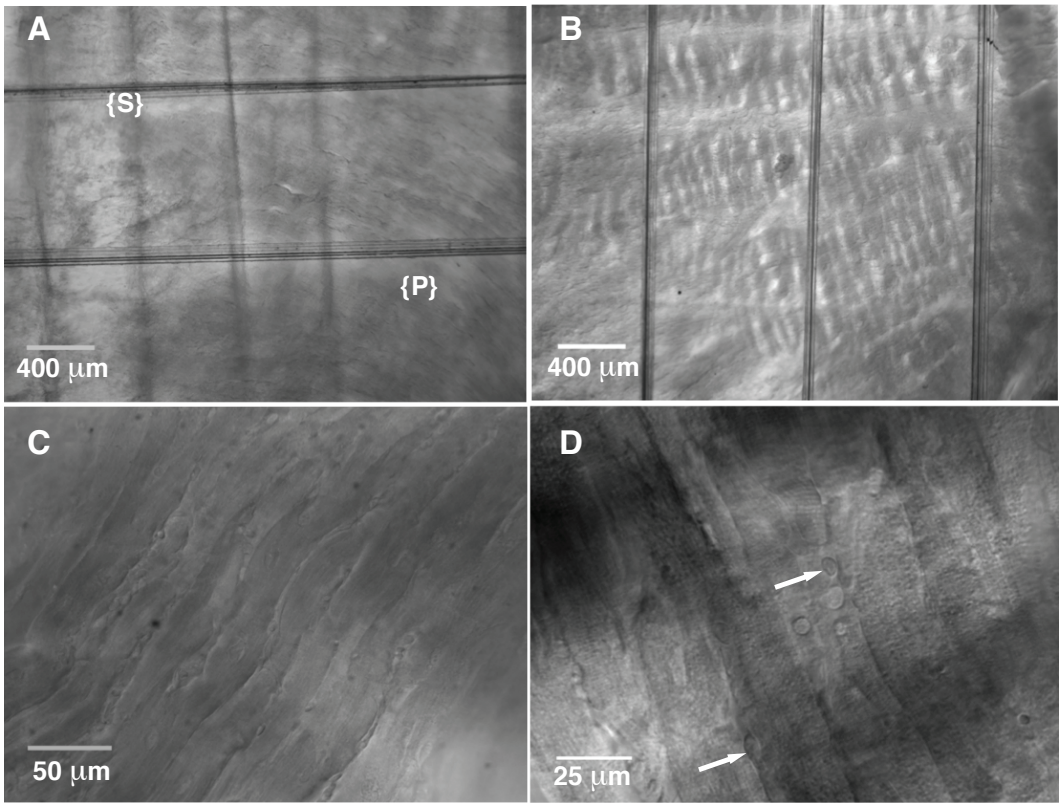

Figure 4.3 | *Cardiac tissue slice morphology*
Acute cardiac slices can be generated from the adult guinea pig heart and can be used to visualize myocyte and non-myocyte cells in a multicellular environment. Slices were generated from the left ventricle, parallel to the epicardial surface. (*A*) Shows areas of a slice in which cardiomyocytes are oriented in cross section {S} and parallel {P} to the plane of the slice. This is due to the rotation of muscle fibers around the axis of the heart. (*B*) The surface of the tissue slice is shown, demonstrating damage due to the vibratome sectioning as indicated by the waves/ripples of hypercontracted and distorted tissue. (*C*) Infrared/Differential interference contrast (IR-DIC) allow for improved contrast to distinguish cell borders and morphology. (*D*) A 2x magnifier can be used for visualizing small cell bodies of non-myocyte cells (indicated by the arrows). Note: Thick parallel nylon wires in (*A*) and (*B*) are the tissue hold downs to keep slices in the recording chamber during perfusion.

Figure 4.3 *B*, shows an example of a slice in which the objective is focused on the top layer of the tissue, which is damaged due to the vibratome sectioning as indicated by the ripples in the tissue surface. Third, in order to visualize the borders of cells and to target cells below the cut surface of the tissue slice, specialized optics are required. Figure 4.3 *C*, shows the enhanced contrast that can be obtained using Infrared/Differential

Interference Contrast (IR/DIC) optics. The IR allows for better visualization below the surface of the tissue and the DIC allows for enhanced contrast. Finally, due to the small size of non-myocyte cell bodies in the cardiac tissue slice, an additional 2x magnifier can provide additional magnification as shown in Figure 4.3 *D*, where arrows indicate non-myocyte cells.

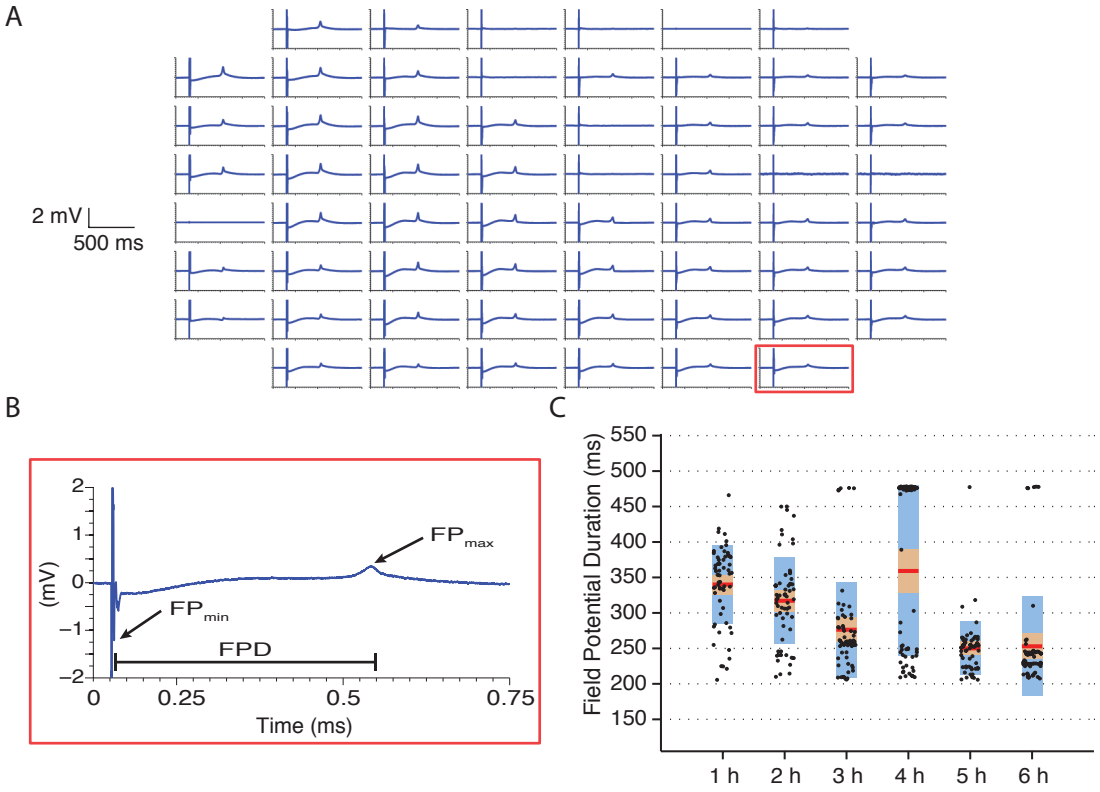

Figure 4.4 | *Field potential recordings from cardiac tissue slices*
(*A*) Field potentials simultaneously recorded from 60 MEA electrodes. (*B*) A magnified view of the recordings from the MEA electrode in (*A−red box*). The field potential duration corresponds to the action potential duration, it is measured from minimum of the I_{Na} peak (FP_{min}) to the maximum of the I_{Kr} current peak (FP_{max}). (*C*) Representative time-lapse recording of FPD (ms) measures at each MEA electrode, was recorded every hour after a 1 h slice pre-incubation period. Red lines represents the mean, orange region the 95% confidence interval for the mean, and the blue region is 1 standard deviation. Note: outlier values are due to spontaneous FPD which distort the analysis

To obtain electrophysiological parameters of the tissue slice a MEA system was used to measure extracellular field potentials. The field potential duration which corresponds to the action potential duration, was measured from the minimum of the initial I_{Na} peak

to the maximum of the I_{Kr} current peak as illustrated in Figure 4.4*B*. The field potential duration is stable for the first two hours after pre-incubation period, but then declines. These results indicate that it is best to perform dye transfer experiments within the first few hours after the preincubation period to ensure slice viability, as suggested by previous studies [3, 10].

Targeting cardiomyocytes for microinjection

Functionally coupled cells can by identified by applying the dual tracer method and taking advantage of the variety of fluorescent tracers that are gap junction channel permeable and their dextran conjugates (Table 4.1). Dextran conjugates cannot pass through gap junctions due to size exclusion and act as a control for identifying the initially injected cell, while the smaller dye is able to pass through gap junction channels indicating functional coupling [15]. Ventricular cardiomyocytes are known to be strongly coupled to each other by Cx43 gap junction channels [16]. Thus, in Figure 4.5 *A*, a cardiomyocytes was targeted for gap junction channel screening as a positive control. Using a small current pulse the two tracers Alexa Fluor 350 (AF350) and dextran conjugated Alexa Fluor 568 (Dex-AF568) are injected simultaneously for 5 mins (Figure 4.5 *B*). The pipette is removed and images are captured post iontophoretic injection (Figure 4.5 *C*). Figure 4.5 *D* shows a merged image of the blue, red, and DIC filter channel, the gap junction channel impermeable dye Dex-AF568 (*red*) remains in the initially injected cell and the gap junction permeable dye AF350 (*cyan-blue*) diffused to the neighboring cells.

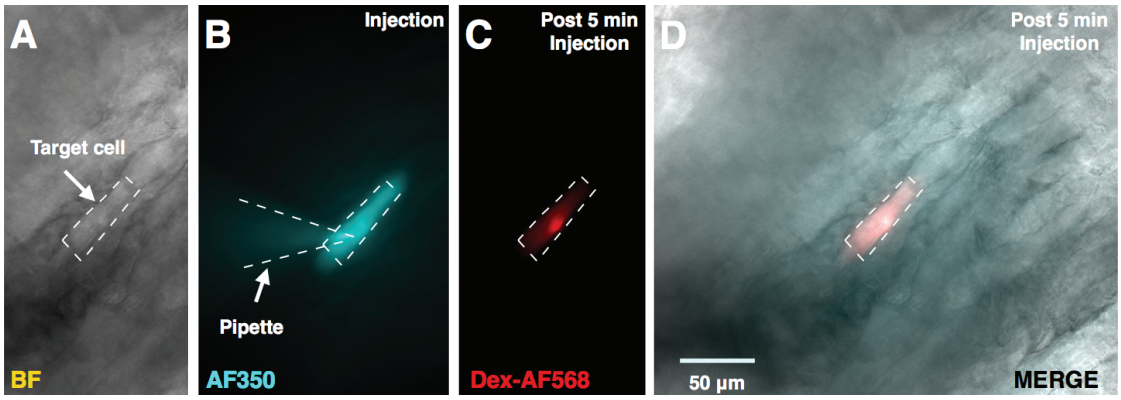

Figure 4.5 | *Cardiomyocyte microinjection under visual control*
(*A*) A single cardiomyocyte is targeted for screening of functional gap junction coupling using IR/DIC optics on a fixed stage upright microscope. (*B*) Using a small current pulse (1-2 nA) the two tracers (in this case AF350 and Dex-AF568) are injected simultaneously for 5 mins as shown. (*C*) The pipette is removed and images are captured post ionophoretic injection using the red filter channel. (*D*) Merged red, blue, and DIC filter channels show the gap junction channel impermeable dye remaining in the injected cell and the gap junction permeable dye transferring to neighboring cells. Images are of the live sample captured in the experimental recording chamber.

Targeting cardiac fibroblasts-like cells for microinjection

Targeting fibroblasts cells is significantly more challenging, due to their small cell size. In Figure 4.6 *A*, a non-myocyte cell is targeted for gap junction channel screening. Two tracers in this case Alexa Fluor 594 (AF594) and dextran conjugated Cascade Blue (Dex-Blue) were injected simultaneously for 5 mins the pipette is removed and images are captured post–iontophoretic injection using both filters in Figure 4.6 *B* and *C*. Figure 4.6 *B* shows the gap junction channel impermeable dye (blue) remaining in the injected cell and Figure 4.6 *C* shows the gap junction permeable dye (red) transferring to neighboring cells. In Figure 4.6 *D* the red, blue, and DIC channels are merged to show the underlying tissue structure, the spread of AF594 (red) to neighboring cells is easier to visualize.

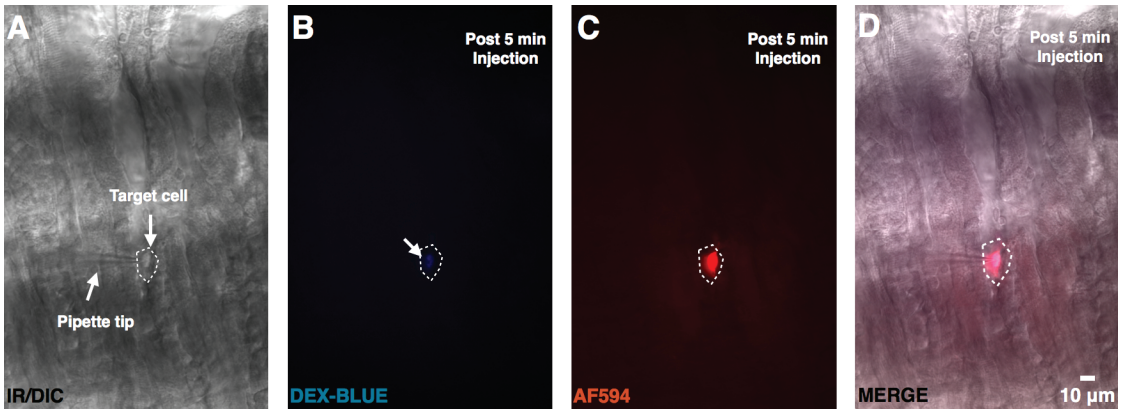

Figure 4.6 | *Non-myocyte microinjection under visual control*
(*A*) A non-myocyte cell is targeted for gap junction channel screening. Two tracers, Alexa Fluor 594 and Dex-Cascade Blue, were loaded into a microelectrode and injected iontophoretically for 5 mins. (*B* and *C*) The pipette is then removed and images are captured post iontophoretic injection using both red (*B*) and blue (*C*) filter channels. (*D*) To show the gap junction channel impermeable dye remaining in the initially injected cell (dotted outline) and the gap junction permeable dye transferring to neighboring cells. Images are of the live sample captured in the experimental recording chamber.

Combining dye transfer studies with immunohistochemistry

Figure 4.7 shows results of microinjection in live samples followed by fixation and immunostaining with vimentin, a commonly used fibroblast marker. In these experiments, a single gap junction permeable tracer was used (i.e., as opposed to the previous dual-tracer method), future experiments will incorporate the dual-tracer technique with immunostaining. Again, cardiomyocytes which are known to be electrically coupled by gap junctions were used as a positive control. A single cardiomyocyte was microinjected iontophoretically with AF594 under visual control. The sample was then fixed and immunostained for vimentin, these results are shown in Figure 4.7. Next, a single non-myocyte cell was iontophoretically injected with Lucifer yellow under visual control. The cardiac tissue slice was then fixed, resectioned, and immunostained for vimentin.

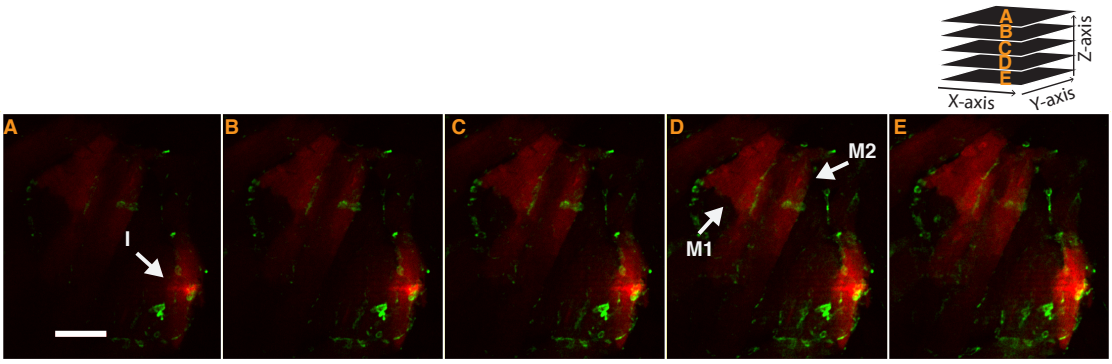

Figure 4.7 | *Investigating myocyte-to-myocyte coupling*
A cardiomyocyte cell with visible striations was targeted for microinjection (*arrow, I*) in the recording chamber and was filled with Alexa Fluor 594 (*red*), a gap junction permeable tracer. The tissue slice was resectioned (20 μm sections) and immunostained for vimentin (*green*). Confocal z-stacks from the microinjected region was captured. Images were collected at 0.5 micron intervals, serial stacks are labelled from A-E. The localization of the dye in neighboring myocyte cells (*arrows, M1, M2*) can be visualized. Scale bar represents 50 μm.

As shown in Figure 4.8, the initially injected cell is shown to have a small round cell body indicated by an arrow, the dye transfers to the neighboring cardiomyocytes as indicated by arrows in Figure 4.8 *F* and Figure 4.8 *G*. In Figure 4.8 *A*, there is vimentin staining just around the borders of the injected cell. However, colocalization of Lucifer yellow and vimentin could not be verified in this image.

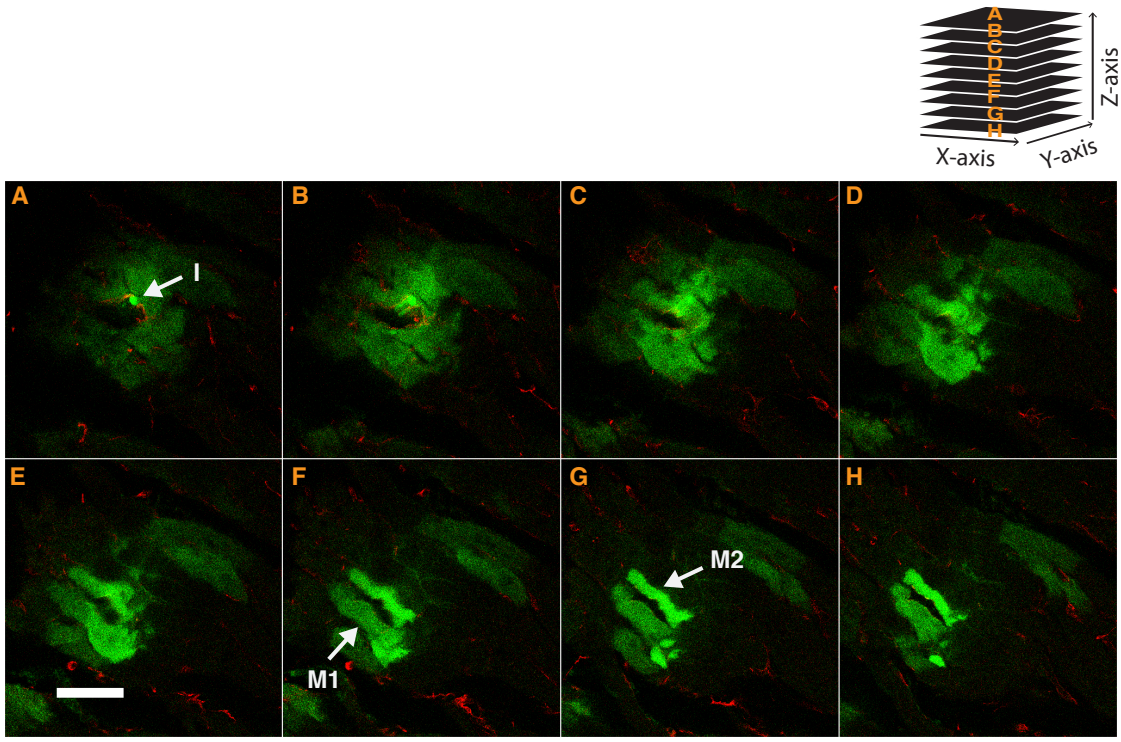

Figure 4.8 | *Investigating non-myocyte-to-myocyte coupling*
A non-myocyte cell with a small cell body was targeted for microinjection (*arrow, I*) in the recording chamber and was filled with Lucifer Yellow (*green*). The tissue slice was resectioned (50 μm sections) and immunostained for vimentin (*red*). Confocal z-stacks from the microinjected region was captured. Images were collected at 1.5 micron intervals, serial stacks are labelled from A-H. Confocal images capture the localization of the dye to neighboring cardiomyocytes filled with Lucifer Yellow (*arrows, M1, M2*). Scale bar represents 50 μm.

4.5 Discussion

Due to the heterogenous structure of cardiac tissue slices, it may be difficult to definitively identify cell types within the sample at the time of iontophoretic injection. This can be easily accomplished if the target cell type has a distinct morphology that is easily identified with optical microscopy. Since fibroblast cell bodies are similar to other non-myocyte cells (pericytes, immune cells). Alternatively, the cardiac tissue slice can be generated from animal models with GFP tagged cell types. Since transgenic guinea pigs

are not readily available, the method can be implemented using genetically engineering mouse models (see Section 5.2.1: Future directions for a description of a strategy for generating slices from transgenic mice). In the event that no coupling is observed, one confounding factor is that experimental conditions may transiently alter the state of the gap junctional channels. This can be overcome by the application of a gap junction opener such as tedisamil [17] to verify the absence of functional coupling. It is important to note that the current method uses nonbiological dyes for an all-or-none detection of junctional communication. However due to the versatility of the experimental setup, the method can be adapted to investigate the transfer of endogenous small molecules provided the appropriate controls are implemented [16].

4.6 Conclusions

Acute cardiac tissue slices can be generated from the adult guinea pig heart and can be used to visualize myocyte and non-myocyte cells in a more native multicellular environment compared to cell culture. Single cells can be targeted for microinjection with fluorescent tracers under visual control using IR/DIC optics to investigate functional gap junction coupling. Immunohistochemistry can be combined with dye transfer studies to identify subpopulations such as cardiac fibroblasts by fixing cardiac slices, thin sectioning, and then free-float immunostaining samples with cell type specific markers. The results showed dye transfer from an initially injected cardiomyocytes and or non-myocyte cell (likely to be fibroblasts) to neighboring myocyte cells, which suggests that these combination of steps are a good strategy for investigating functional coupling in cardiac tissue. The methods described were applied to the investigation of myocyte-to-myocyte coupling and to non-myocyte-to-myocyte coupling, but the method can be expanded to investigate coupling between other cell populations resident in cardiac tissue slices.

BIBLIOGRAPHY

1. Burnashev, N. A., Edwards, F. A. & Verkhratsky, A. N. Patch-clamp recordings on rat cardiac muscle slices. *Pflugers Arch.* (1990).

2. Pillekamp, F. *et al.* Establishment and characterization of a mouse embryonic heart slice preparation. *Cell. Physiol. Biochem.* (2005).

3. Bussek, A. *et al.* Tissue slices from adult mammalian hearts as a model for pharmacological drug testing. *Cell. Physiol. Biochem.* (2009).

4. Camelliti, P. *et al.* Adult human heart slices are a multicellular system suitable for electrophysiological and pharmacological studies. *Journal of Molecular and Cellular Cardiology* (2011).

5. Halbach, M. *et al.* Electrophysiological Maturation and Integration of Murine Fetal Cardiomyocytes After Transplantation. *Circ. Res.* (2007).

6. Bussek, A. *et al.* Cardiac tissue slices with prolonged survival for in vitro drug safety screening. *Journal of Pharmacological and Toxicological Methods* (2012).

7. Riegler, J, Gillich, A, Shen, Q, Gold, J. D. & Wu, J. C. Cardiac tissue slice transplantation as a model to assess tissue-engineered graft thickness, survival, and function. *Circulation* (2014).

8. Sigg, D. C. *Cardiac Electrophysiology Methods and Models* (Springer Verlag, 2010).

9. Himmel, H. M. *et al.* Field and action potential recordings in heart slices: correlation with established in vitro and in vivo models. *British Journal of Pharmacology* (2012).

10. Wang, K. *et al.* Cardiac Tissue Slices: Preparation, Handling, and Successful Optical Mapping. *Am. J. Physiol. Heart Circ. Physiol.* (2015).

11. Baudino, T. A. *et al.* Cell Patterning: Interaction of Cardiac Myocytes and Fibroblasts in Three-Dimensional Culture. *MAM* (2008).

12. Camelliti, P., Green, C. R., LeGrice, I. & Kohl, P. Fibroblast network in rabbit sinoatrial node: structural and functional identification of homogeneous and heterogeneous cell coupling. *Circ. Res.* (2004).

13. Davie, J. T. *et al.* Dendritic patch-clamp recording. *Nat Protoc* (2006).

14. Satoh, H, Delbridge, L. M., Blatter, L. A. & Bers, D. M. Surface:volume relationship in cardiac myocytes studied with confocal microscopy and membrane capac-

itance measurements: species-dependence and developmental effects. *Biophysical Journal* (1996).

15. Mobbs, P., Becker, D., Williamson, R., Bate, M. & Warner, A. Techniques for dye injection and cell labeling (1994).

16. Harris, A. & Locke, D. *Connexins* (Humana Pr Inc, 2009).

17. Dhein, S. Pharmacology of gap junctions in the cardiovascular system. *Cardiovasc. Res.* (2004).

CHAPTER 5

CONCLUSIONS AND FUTURE DIRECTIONS

5.1 Summary of research

In conclusion, this thesis investigated the role of gap junction channel gating on the electrotonic interactions between cardiomyocytes and fibroblasts using a multiscale computational modeling and experimental electrophysiology approach. Mathematical models of dynamic gap junctional channels that reproduce the key features of the time- and voltage-dependent properties of Cx43, Cx45 and Cx43/Cx45 gap junctional channels were developed. These models were then used to investigate the role of gap junction channel gating during myocyte-fibroblast electrical coupling using a combination of computational modeling and the dynamic clamp technique. The results showed that the early component of the gap junctional current was reduced during dynamic fibroblast-myocyte coupling compared to a constant value conductance representation of the gap junction coupling. This was due to the large transjunctional voltage during the early upstroke of the action potential resulting in the inactivation of the gap junction channel. Moreover, the magnitude of this reduction depends on the phenotype of the gap junctional channel, the magnitude of the gap junctional conductance, and the fibroblast-myocyte ratio. These gap junctional models were also incorporated in a tissue sheet model of cardiac fibrosis with tissue structures representing patchy fibrosis after myocardial infarction and myocyte-fibroblast coupling in cell culture conditions. The results of these simulations showed that gap junction gating did not significantly modify conduction velocity compared to a static representation of gap junction coupling. Finally, a strategy using acute cardiac tissue slices generated from the adult guinea pig heart was proposed to investigate myocyte-fibroblast interactions in a multicellular environment. The results show that combining dye transfer studies to investigate functional coupling

along with immunostaining to identify cell types in cardiac tissue slices is a promising strategy for investigating cell-to-cell coupling in cardiac tissue.

5.2 Future directions

One of the challenges of evaluating myocyte-fibroblast interactions in cardiac tissue slices is the targeting of fibroblast cells in live tissue slice samples. In the studies presented in Chapter 4, microinjection was completed on fibroblast-like cells based on their morphology in the live recording setup. Afterwards, verification of the identity of the injected cell was completed by immunohistochemistry. This method can be tedious as it requires fixation of cardiac slices, thin sectioning and free float staining in order to verify the phenotype of the injected cell. An alternative strategy that can circumvent the post-injection verification of the injected cell phenotype and allow for a higher success rate in targeting a specific subpopulation of cells (i.e., cardiac fibroblasts) within the slice is to generate cardiac tissue slices from transgenic mice with GFP tagged cardiac fibroblast.

5.2.1 Cardiac tissue slices generated from transgenic mice

Materials and Methods

Mouse model Thy1 has been described to be expressed in cardiac fibroblasts [1, 2]. The Tg(Thy1-EGFP)MJrs/J mouse strain stably expresses Thy1-EGFP and thus may fluorescently label cardiac fibroblasts in the heart. These Thy1-EGFP mice can be used to locate cardiac fibroblasts in cardiac tissue slices in order to investigate their functional coupling with neighboring cardiomyocytes using the dye transfer technique.

Generating tissue slice from adult mouse heart Isolation of the mouse heart can be performed as described previously [3]. All procedures should be done in accordance

with Weill Cornell IACUC guidelines. Briefly, mice are anesthetized via inhalation of isoflurane, and their hearts removed and placed into ice-cold Modified Tyrode's solution containing (in mM):118.5 NaCl, 4.7 KCl, 1.2 $MgSO_4$, 1.2 KH_2PO_4, 0.9 $CaCl_2$, 25 $NaHCO_3$, 11 Glucose and supplemented with 0.2 ml Heparin to make a Dissection buffer. The heart is removed and placed in ice-cold Dissection buffer. Using a dissecting microscope, the base of the aorta is located under the thymus tissue. Then using curved forceps the aorta is loaded on a cannula attached to a 3 ml syringe containing Dissection buffer. The Dissection buffer is perfused through the heart to test for leakage at the cannulation site. The aorta is then fixed to the cannula using a surgical suture. The cannulated heart is then loaded on a Langendorff apparatus and perfused with warmed (37 °C) oxygenated (5% Carbon dioxide; 95% Oxygen) Modified Tyrode's solution to remove blood. Next, warmed and oxygenated Modified Tyrode's supplemented with 30 mM BDM is perfused to inhibit contractions. The heart is then removed from the cannula and placed in a petri dish containing ice-cold Modified Tyrode's supplemented with 30 mM BDM. The right ventricle is dissected away using fine scissors, the left ventricle is filled with 4% low melt agarose to stabilize the tissue for vibratome sectioning. The ventricle is then embed into a cryomold containing 4% low melt agarose. The agarose block is then trimmed to remove excess agarose and attached to the vibratome platform with cyanoacrylate glue. Slices are then generated using methods described in Section 4.3.

5.2.2 Internal pipette perfusion to modify gap junction properties

To go beyond the all-or-nothing evaluation of dye transfer between myocyte and non-myocyte cells, strategies to manipulate gap junctions by modifying the internal composition of the iontophoretic pipette have been developed. Velumian *et al.* [4], describes a simple and inexpensive strategy to apply the internal perfusion technique to studies in acute slices from the brain, which can potentially be modified for the application in

cardiac tissue slices. In brief, a pipette holder with a perfusion port is used to position a fine infusion tube inside the iontophoretic pipette, the infusion tube is connected to a solution reservoir, solutions are exchanged by applying pressure to the back of the pipette. Thus, internal pipette perfusion can be used to acutely modify gap junction function through modifying intracellular solution [5].

5.2.3 Detailed electrophysiological modeling of cardiac tissue slices

Detailed microstructural information of cardiac tissue slices can be acquired using immunohistochemistry and confocal microscopy. Recent studies have introduced methodologies involving the quantitative analysis of cardiac tissue based on fluorescent labeling, three-dimensional confocal microscopy, and image processing and reconstruction [6, 7]. Applying this methodology to cardiac tissue slices can provide unique opportunities to correlate microstructural information with electrophysiological data from multielectrode arrays [8–10] and microelectrode action potential recordings [11] in order to generate micostructurally detailed electrophysiological models of cardiac tissue slices.

5.3 Concluding thoughts

In conclusion, multi-scale computational modeling studies in combination with *in vitro* experiments have demonstrated that cardiac fibroblasts may modify action potential duration, induce spontaneous activity, modify conduction velocity, and increase susceptibility to early afterdepolarizations and cardiac alternans. The extent of these fibroblast-mediated changes depends on the density of fibrosis, the magnitude of the gap junctional conductance, the underlying electrophysiology of cardiac fibroblasts.

Myocyte-fibroblast coupling has been well documented in cell culture conditions and a major challenge of the field has been to determine to what extent this mechanism

of cardiomyocyte electrophysiology modification occurs *in vivo*. To date, functional coupling between myocytes and fibroblast have been shown *in situ* in the rabbit sinoatrial node, a region of the heart thought to natively contain many fibroblasts. Whether functional myocyte-fibroblast coupling occurs and plays a significant role in other regions of the heart is to be determined. In the diseased heart non-myocytes (likely predominantly composed of fibroblasts) are thought to play a role in bridging electrical activity across ventricular scars [12].

The goal of this thesis was to expand on the current understanding of gap junction function between myocyte and fibroblasts. In particular, since different connexins phenotypes have been found in myocytes and fibroblasts in both *in vitro* and *in situ* studies, this thesis explored whether the dynamic properties (i.e., time– and transjunctional voltage–dependence) of connexins played a role in the contribution of fibroblasts to cardiomyocyte electrophysiology. Furthermore, a novel strategy to investigate functional coupling between myocytes and fibroblasts in the heart was developed. This strategy focused on using the recently improved cardiac tissue slice model in hopes that the advantage of having an intact multicellular environment and optically accessible cells would allow for targeted investigation of cell-to-cell coupling.

However, significant challenges remain in investigating myocyte to non-myocyte coupling in live cardiac tissue samples. Future strategies that aim towards improving the method of targeting non-myocyte cell types in the live tissue slices using transgenic mouse models which express GFP in the target cell types can significantly improve the efficiency of such experiments. This will allow for more reliable identification of non-myocyte cells and faster screening of myocyte to non-myocyte coupling in a given slice. Furthermore, to go beyond the determination of the existence or absence of coupling, internal pipette perfusion can be used to acutely modify the functional state of local gap junctions in a particular cell, allowing for an investigation of chemical modifiers

of myocyte to non-myocyte coupling. Finally, detailed microstructural imaging can be obtained from confocal microscopy and image processing of tissue slices and then combined with electrophysiology recordings to develop detailed microstructural and electrophysiology models of cardiac tissue.

BIBLIOGRAPHY

1. Rochais, F *et al.* FGF10 promotes regional foetal cardiomyocyte proliferation and adult cardiomyocyte cell-cycle re-entry. *Cardiovasc. Res.* (2014).

2. Ieda, M. *et al.* Cardiac Fibroblasts Regulate Myocardial Proliferation through b1 Integrin Signaling. *Developmental Cell* (2009).

3. Li, D., Wu, J., Bai, Y., Zhao, X. & Liu, L. Isolation and culture of adult mouse cardiomyocytes for cell signaling and in vitro cardiac hypertrophy. *JoVE* (2014).

4. Velumian, A. A., Zhang, L & Carlen, P. L. A simple method for internal perfusion of mammalian central nervous system neurones in brain slices with multiple solution changes. *Journal of Neuroscience Methods* (1993).

5. Verrecchia, F *et al.* ATP counteracts the rundown of gap junctional channels of rat ventricular myocytes by promoting protein phosphorylation. *The Journal of Physiology* (1999).

6. Schwab, B. C. *et al.* Quantitative Analysis of Cardiac Tissue Including Fibroblasts Using Three-Dimensional Confocal Microscopy and Image Reconstruction: Towards a Basis for Electrophysiological Modeling. *IEEE Trans Med Imaging* (2013).

7. Bauer, S, Edelmann, J. C., Seemann, G, Sachse, F. B. & Dössel, O. Estimating Intracellular Conductivity Tensors from Confocal Microscopy of Rabbit Ventricular Tissue. *Biomed Tech (Berl)* (2013).

8. Sun, J. *et al.* Microelectrode array measurement of potassium ion channel remodeling on the field action potential duration in rapid atrial pacing rabbits model. *Int J Clin Exp Med* (2015).

9. Bussek, A. *et al.* Tissue slices from adult mammalian hearts as a model for pharmacological drug testing. *Cell. Physiol. Biochem.* (2009).

10. Camelliti, P. *et al.* Adult human heart slices are a multicellular system suitable for electrophysiological and pharmacological studies. *Journal of Molecular and Cellular Cardiology* (2011).

11. Bussek, A. *et al.* Cardiac tissue slices with prolonged survival for in vitro drug safety screening. *Journal of Pharmacological and Toxicological Methods* (2012).

12. Walker, N. L., Burton, F. L., Kettlewell, S., Smith, G. L. & Cobbe, S. M. Mapping of epicardial activation in a rabbit model of chronic myocardial infarction:. *J. Cardiovasc. Electrophysiol.* (2007).

APPENDIX A

A.1 Equations for the gap junction model

Equations for the gap junction model from [1].

$$I_{\mathrm{j}} = G_{\mathrm{j}} \cdot V_{\mathrm{j}} \tag{A.1}$$

$$G_{\mathrm{j}} = N_{\mathrm{chans}}(G_{\mathrm{HH}} \cdot N_{\mathrm{HH}} + G_{\mathrm{LH}} \cdot N_{\mathrm{LH}} \cdot G_{\mathrm{HL}} \cdot N_{\mathrm{HL}} + G_{\mathrm{LL}} \cdot N_{\mathrm{LL}}) \tag{A.2}$$

$$\begin{aligned}
\frac{\mathrm{d}N_{\mathrm{HH}}}{\mathrm{d}t} &= -(\beta_1 + \beta_2) \cdot N_{\mathrm{HH}} + \alpha_1 \cdot N_{\mathrm{LH}} + \alpha_2 \cdot N_{\mathrm{HL}} \\
\frac{\mathrm{d}N_{\mathrm{LH}}}{\mathrm{d}t} &= \beta_1 \cdot N_{\mathrm{HH}} - (\alpha_1 + \beta_4) \cdot N_{\mathrm{LH}} + \alpha_4 \cdot N_{\mathrm{LL}} \\
\frac{\mathrm{d}N_{\mathrm{HL}}}{\mathrm{d}t} &= \beta_2 \cdot N_{\mathrm{HH}} - (\alpha_2 + \beta_3) \cdot N_{\mathrm{HL}} + \alpha_3 \cdot N_{\mathrm{LL}} \\
\frac{\mathrm{d}N_{\mathrm{LL}}}{\mathrm{d}t} &= \beta_4 \cdot N_{\mathrm{LH}} + \beta_3 \cdot N_{\mathrm{HL}} + (\alpha_3 + \alpha_4) \cdot N_{\mathrm{LL}}
\end{aligned} \tag{A.3}$$

$$\begin{aligned}
\alpha_1 &= \frac{2 \cdot \alpha_{\mathrm{coef1}}}{1 + exp(-V_{\mathrm{LH1}}/V_{\alpha 1})} \quad \alpha_2 = \frac{2 \cdot \alpha_{\mathrm{coef2}}}{1 + exp(-V_{\mathrm{HL2}}/V_{\alpha 2})} \\
\alpha_3 &= \frac{2 \cdot \alpha_{\mathrm{coef1}}}{1 + exp(-V_{\mathrm{LL1}}/V_{\alpha 1})} \quad \alpha_4 = \frac{2 \cdot \alpha_{\mathrm{coef2}}}{1 + exp(-V_{\mathrm{LL2}}/V_{\alpha 2})}
\end{aligned} \tag{A.4}$$

$$\begin{aligned}
\beta_1 &= \beta_{\mathrm{coef1}} \cdot exp(-V_{\mathrm{HH1}}/V_{\beta 1}) \quad \beta_2 = \beta_{\mathrm{coef2}} \cdot exp(-V_{\mathrm{HH2}}/V_{\beta 2}) \\
\beta_3 &= \beta_{\mathrm{coef1}} \cdot exp(-V_{\mathrm{HL1}}/V_{\beta 1}) \quad \beta_4 = \beta_{\mathrm{coef2}} \cdot exp(-V_{\mathrm{LH2}}/V_{\beta 2})
\end{aligned} \tag{A.5}$$

$$g_{\mathrm{xy}} = \frac{g_{\mathrm{x}} \cdot g_{\mathrm{y}}}{(g_{\mathrm{x}} + g_{\mathrm{y}})} \quad g_{\mathrm{x}} = \gamma_x \cdot exp(-V_{jx}/V_{\mathrm{x}}) \tag{A.6}$$

$$V_{\mathrm{jx}} = -V_j \left(\frac{g_{\mathrm{x}} \cdot g_{\mathrm{y}}}{(g_{\mathrm{x}} + g_{\mathrm{y}})} \right) \quad V_{\mathrm{jy}} = V_j \left(\frac{g_{\mathrm{x}} \cdot g_{\mathrm{y}}}{(g_{\mathrm{x}} + g_{\mathrm{y}})} \right) \tag{A.7}$$

A.2 Parameters of gap junction model

Table A.1 | Connexin model parameters

Parameters	Units	Cx43	Cx45	Cx43/Cx45
V_{H_1}	mV	156.2	125.38	99.95
V_{L_1}	mV	218.7	299.23	351.3
γ_{H_1}	pS	158.5	71.518	140
γ_{L_1}	pS	14	4.7646	11.42
α_1	s$^-$1	167.4	144.1	264.3
β_1	s$^-$1	0.02338	0.02064	0.000951
V_{α_1}	mV	9.926	6.989	11.57
V_{β_1}	mV	6.152	5.235	7.314
V_{H_2}	mV	156.2	125.38	844.9
V_{L_2}	mV	218.7	299.23	603.5
γ_{H_2}	pS	158.5	71.518	95.38
γ_{L_2}	pS	14	4.7646	2.09
α_2	s$^-$1	167.4	144.1	77.3
β_2	s$^-$1	0.02338	0.02064	0.02637
V_{α_2}	mV	9.926	6.989	2.235
V_{β_2}	mV	6.152	5.235	7.674
N_{Chans}	-	13	28	19
N_{HH_0}	-	0.99	0.99	0.91
N_{HL_0}	-	6.56E-07	0.00043905	0.0606
N_{LH_0}	-	4.44E-14	0.00040637	7.063E-06
N_{LL_0}	-	4.44E-14	7.63E-05	0.02437